ABSTRACT

Title of Thesis: DESIGN AND TESTING OF A GALFENOL TACTILE SENSOR ARRAY

Kathleen L. Hale, Master of Science, 2006

Thesis directed by: Professor Alison Flatau
Department of Aerospace Engineering

The smart material Galfenol, $Fe_{100-x}Ga_x$, where $15<x<28$, offers a unique combination of mechanical and magnetostrictive properties that are expected to lead to its use in new sensor and actuator concepts. This thesis seeks to determine if Galfenol can be used to develop a 2-dimensional array of force sensors as part of a 3-D magnetic circuit that, if properly scaled, could mimic the tactile force sensing capabilities needed for use in robotic grippers, prosthetic devices, and robotic surgery. This concept takes advantage of the fact that Galfenol is not brittle and its permeability has high sensitivity to mechanical loads. The hypothesis is that applying stress or force to one or more of the Galfenol rods will produce changes in Galfenol's permeability which will produce changes in the flux density distribution in the magnetic circuit that can be used to determine information about both the load's magnitude and location. The studies performed demonstrated that the decrease in permeability of a loaded rod results in complex changes in magnetic flux. Results from this thesis include recommendations for modifications to better match the rod flux density to the applied load levels and prevent rod top separation.

DESIGN AND TESTING OF A GALFENOL TACTILE SENSOR ARRAY

by

Kathleen L. Hale

Thesis submitted to the Faculty of the Graduate School of the
University of Maryland, College Park, in partial fulfillment
of the requirements for the degree of
Master of Science
2006

Advisory Committee:

Professor Alison B. Flatau, Chair
Professor Sung Lee
Professor Inderjit Chopra

Acknowledgements

First I would like to thank my parents and for their unending support and encouragement. I would also like to thank Ryan Boller of NASA Goddard for stirring the creative juices of robotic tactile feedback research and for his initial collaborations and brainstorming on this project. Next, I would like to thank Dan Clingeman for encouraging me to perform this work and for introducing me to Dr. Flatau. Carlos Lugo at NASA Goddard deserves all the thanks possible for his electrical support and encouragement through his wonderfully positive attitude. I would also like to thank Steve Wood at NASA Goddard and Luke Twarek and Mike Perna at the University of Maryland, College Park for their help in the machine shops. Thank you to Professor Alison Flatau for giving me the opportunity to work on this project and for her advice and guidance. My accomplishments would not be possible without the advice and knowledge shared by my fellow grad students: Pat Downey, Jayasimha Atulasimha, Chaitanya Mudivarthi, Ron DiSabatino, Supratik Datta, and Dr. Jin Yoo. And with immense gratitude, thank you Michael for your insightfulness, wisdom, and endless support.

This work was supported partially as an Internal Research and Development (IRAD) project at the NASA in collaboration with the University of Maryland.

Table of Contents

1 INTRODUCTION

Tactile force feedback sensors are an essential part of the sensory equipment required for robotic end effectors to properly grasp an object of unknown size and shape (Biagiotti et al., 2003). Currently, force feedback sensors consist of strain gages, force sensing resistors, torque sensors, and others. These set-ups typically do not provide the force range or resolution required and may be cumbersome or expensive. They also provide neither the force resolution nor the spatial resolution of the human fingertip, which has been shown to have a spatial resolution of on the order of 40 microns (Maheshwari and Saraf, 2006).

Increasing the dexterity of robotic and prosthetic grippers using a sensor array capable of providing resolution at least equal to that of human fingertips (and ideally of even greater spatial resolution) would greatly increase the usefulness for these devices. The smart material Galfenol, $Fe_{100-x}Ga_x$, where $15<x<28$, offers a unique combination of mechanical and magnetostrictive properties that lend it to these types of applications. Nanowires made of Galfenol have recently been successfully grown at the nano-scale (McGary et al., 2005). As shown in Figure 1, these nanowires can be grown with diameters of about ∅20 to ∅500 nm. Using the proposed 2-D grid array and magnetic circuit concepts, a sensor array of Galfenol nanowires could be placed on the end effectors of robots, prosthetics, and even robotic surgical devices to provide a high-resolution tactile force feedback capability. Such a system would enable both remote users of such systems to know exactly how much force they are applying when grasping

objects and would enable the operator to determine the size, shape, and surface characteristics of an object.

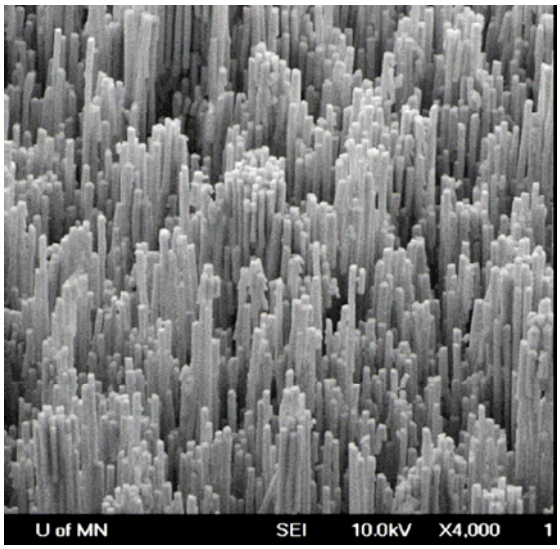

Figure 1: Top View of Nanowires (McGary et al, 2006) Wires can be grown with diameters ranging from ∅20 to ∅500 nm.

With the ability to manufacture Galfenol at such a small scale and the plan to place many of the nanowires together in an array that covers the size of the human fingertip, the Galfenol arrays could enable a feedback system with low mass and high resolution that is able to withstand the rigors of everyday human use and even the environment of outer space. It is this project's objective to investigate the behavior of such an array at the macro scale and to determine concept feasibility before attempting implementation at the nano-scale.

1.1 Current and Future Use of Tactile Sensors

Currently, force feedback sensors from smart materials are appealing for use in the robotic space industry realm. Smart materials are ideal as they are small, lightweight, require low levels of power, and can survive in vacuum and the extreme temperatures of

space. One particular device that can benefit from this technology is the humanoid robot developed at NASA's Johnson Space Center called Robonaut. Currently, a commercial technology of Force Sensing Resistors (FSR) made by Interlink Electronics® are used to detect force levels on the robot's hand. However, the force's location can only be detected along one axis, and the resolution of that location is not stated. (http://robonaut.jsc.nasa.gov/mit_hand) Additionally, the hand gets general force feedback from load cells inserted into the leadscrew assemblies and wrist ball joint links (Bluethmann et al., 2003). If Robonaut had the same fingertip force feedback resolution as a human, the dexterity of the robot would be greatly enhanced and Robonaut would be able to perform more intricate tasks.

Prosthetics would benefit from smart material sensors as well, due to their low mass and high resolution capabilities. In Zecca et al., the prosthetic hand designed uses a force sensing resistor to obtain pressure feedback on the thumb tip. The sensor is 5-mm in diameter and 0.3-mm thick, which at best would allow a resolution between force locations of 5-mm. If an array of Galfenol nanowires were used instead, the resolution of sensitivity would be much greater due to the ability to grow the wires from ∅20- to ∅500-nm in diameter. By greatly increasing the hand's sensitivity, it would have the ability to grasp smaller and more delicate objects.

Another area that could benefit from force feedback sensors is the realm of robotic surgery. Laparoscopic surgery is one type that uses equipment to perform tasks with minimal invasion to the body. The technique has several advantages including smaller

incisions, less risk for infection, and shorter recovery time. Although laparoscopic surgery has progressed dramatically over past techniques, it still has several areas that need improvement. Due to the equipment constraints there is a decrease in hand-eye coordination, dexterity, and haptic feedback (Lanfranco et al., 2004) when compared to what can be done at a larger scale. Integration of a tactile feedback array, such as the one proposed here, built at the nanoscale could be attached to the end-effector of the surgical equipment. Possible end-effectors are a grasper, resectoscope, or scalpel (Lee et al., 1999). Adding a force feedback array to such an end-effector would increase the surgeon's sensitivity to his or her own movements within the body and therefore provide the ability to perform delicate and difficult procedures.

1.2 Background on Magnetics

An overview of the magnetic units and relations used in this paper are briefly described in this section. Flux density, B, can be equated to a relationship of the permeability of a material, μ, and the field, H, as shown in Equation 1.

$$B = \mu H \tag{1}$$

The SI units used to describe magnetic field and magnetic flux density (also known as magnetic induction) are Amperes per meter (A/m) and Tesla (T) respectively (cgs units are Oersteds and Gauss respectively) (Fitzgerald et al., 2003). 10,000 Gauss is equal to 1 Tesla. Magnetic flux density is a scalar quantity that is a measure of magnetism by taking account of the strength and extent of a magnetic field.

Initial flux density levels are measured for many of the experiments listed in this paper. The measurements are taken with a gaussmeter. The meter detects the flux density with a probe that is placed as close as possible to the top of the steel components that make up circuit area of interest. Although close to the circuit surface, the probe measures the flux density in air at this location and not the flux density level in the circuit. Since the permeability of air is $\mu = 1$, the flux density in Gauss is equal in magnitude to the magnetic field in Oersted (Equation 2).

$$B_{Gauss} = \mu H_{Oersted} = H_{Oersted} \tag{2}$$

1.3 Background on Magnetostriction and Galfenol

Magnetostriction effects were first discovered by James Prescott Joule in the 1840s when he observed the change in length of an iron sample in relation to the sample's magnetization. The opposite case, in which a change in magnetization results from stress applied to the material, is called the Villari effect. It is this effect that allows the use of magnetostrictive materials as force or motion sensors. (Calkins et al., 1999)

Devices built in the first half of the 20th century, such as telephone receivers, scanning sonar, and hydrophones, were developed using nickel and other magnetostrictive materials that exhibited magnetostriction of less than 100 μL/L (micro length per length). In the 1970s, materials were discovered that provided much higher magnetostriction; on the order of 1000 μL/L or greater. These materials are called "giant" magnetostrictive

alloys. Current devices using these "giant" magnetostrictive materials include high force linear motors, active vibration and noise control, hearing aids, underwater sonar, and many others. (Calkins et al., 1999)

The smart material, Galfenol, is considered to be a "large" magnetostrictive material with strain capability ranging from 300 - 400 parts per million (Clark et al., 2000). Galfenol is an alloy made of Iron and Gallium, $Fe_{100-x}Ga_x$, where $15 \leq x \leq 28$, creates a material with useful mechanical and transduction attributes (Clark et al., 2000, Kellogg, 2002). By combining Gallium with Iron at these percentages, Galfenol has been shown to have magnetostriction equal to about 10 times that of pure Iron (Summers et al., 2004). Galfenol is also available in either a single crystal or polycrystalline form. Single crystal has higher transduction coefficients than polycrystalline, but is more costly. Polycrystalline Galfenol is currently available as either production or research grade. These designations are related to the sample growth rate, with the slower rate being the research grade. The slower growth rate produces samples with properties that more closely resemble single crystal Galfenol properties. The Galfenol used in this thesis was 18.4% Gallium research grade material that was provided by Etrema Products Inc.

The basic relationship between field and stress in Galfenol is depicted in Figure 2. Figure 2a shows a cartoon depicting how the magnetic domains within Galfenol are randomly aligned when at room temperature, unstressed, and under no magnetic fields. Note that in the first state there is no net magnetization in the sample. With a magnetic field applied axially through a rod of Galfenol, the domains will rotate until they become aligned with

the direction of the applied field (Fig. 2b). This domain rotation causes the material to lengthen and the magnetic flux density in the rod to increase. Once fully aligned with the applied field at what is termed the saturation field level, further increases in magnetic field would produce very small increases in the magnetic flux density in the rod and no increase in length. As shown in Figure 3, the saturation level for a rod of research grade, polycrystalline Galfenol ($Fe_{81.6}Ga_{18.4}$), is about 1.6 – 1.7 Tesla at about 50 Oe. Figure 2c shows a compressive load applied to the rod, causing the length to shorten and the magnetic moments to rotate. Rotation of the magnetic moments causes the permeability of the material to increase and the flux density in the rod to decrease. Once the magnetic domains rotate a full 90° additional stress will not cause any substantial change in the magnetic flux density of the rod, Figure 2d and Figure 4. (Atulasimha, Flatau, and Kellogg, 2006)

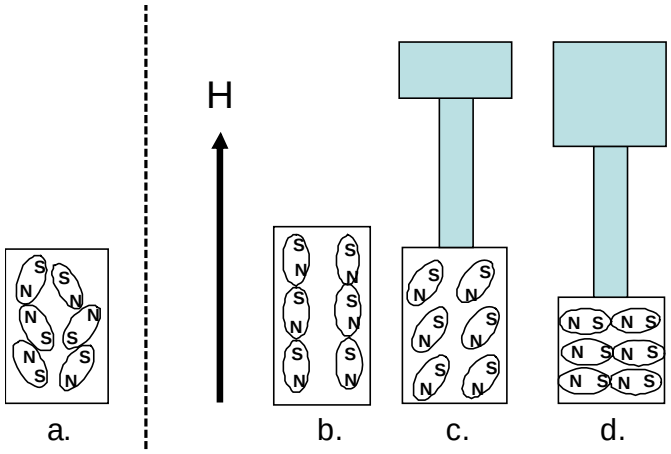

Figure 2: Polycrystalline, research grade, Galfenol rod ($Fe_{81.4}Ga_{18.6}$) a. Under no stress, and no field; b. Under field H (saturated) under no external stress; c. Under field H and intermediate external stress; d. Under field H and high external stress.

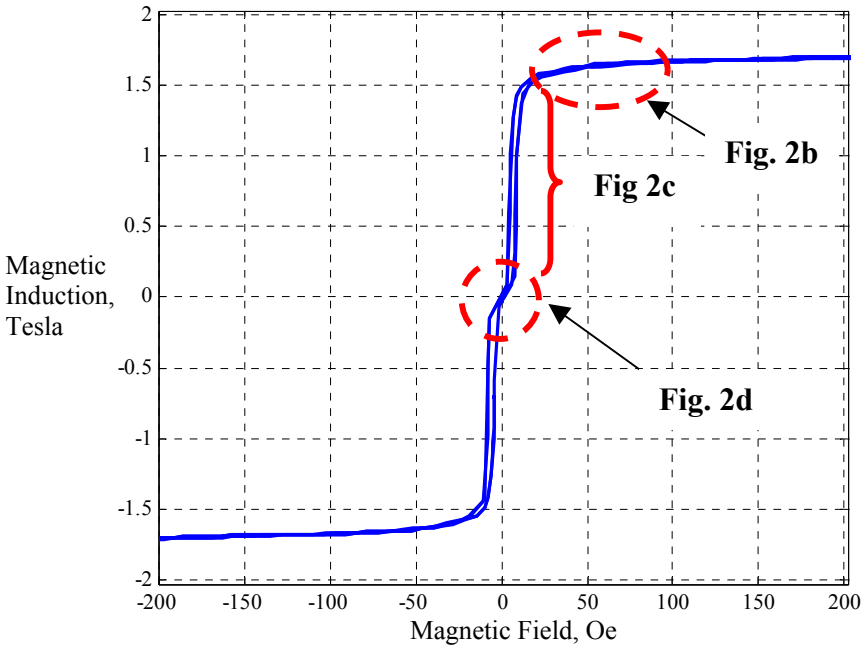

Figure 3. Magnetic induction vs. magnetic field for a research grade polycrystalline rod with zero initial stress (courtesy of Atulasimha, 2006). Labels indicate how this figure corresponds to Figure 2.

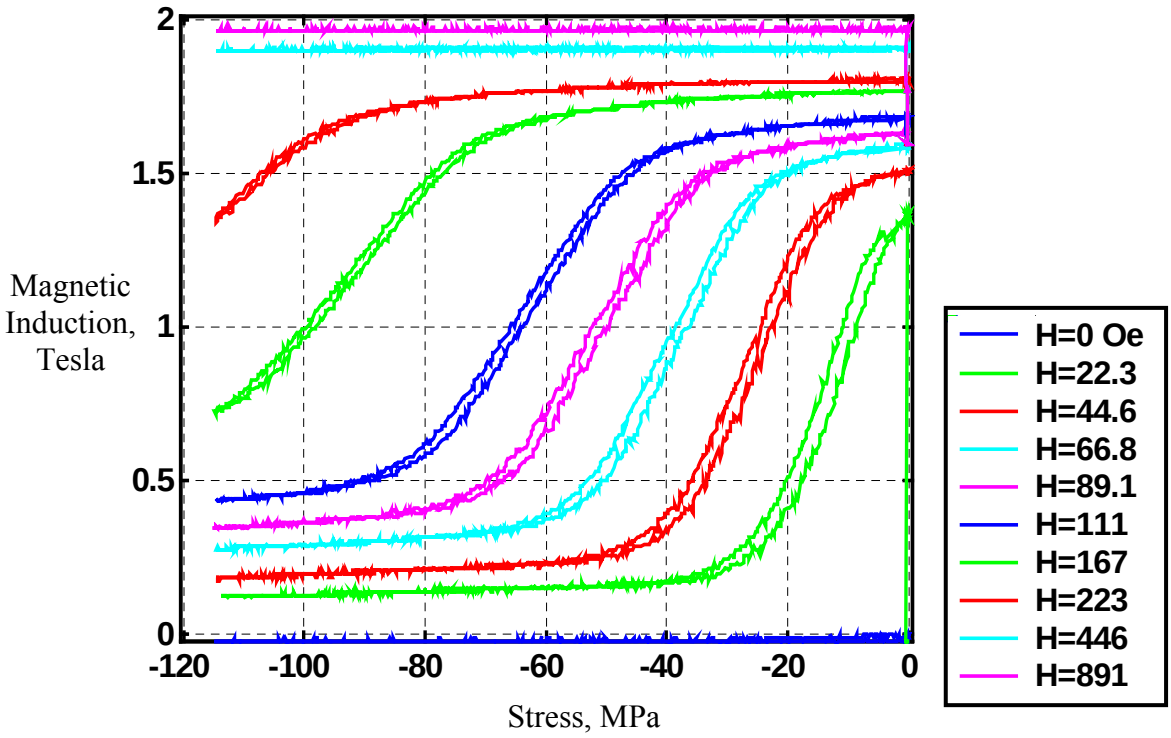

Figure 4: Magnetic induction vs. stress for a production grade polycrystalline rod with zero initial stress (courtesy of Atulasimha, 2006).

1.4 Proposed Sensor Array

The concept for the proposed sensor array stems from the characteristics of Galfenol and magnetic circuits. An array of Galfenol rods placed within an array of magnetic circuits can be biased so that when the rods are stressed the permeability of the rods changes and the flux passing through them will change proportionally. The change in flux density of the rods will alter the flux density of the circuit return paths, and this change can be detected by sensors. Post-processing performed to correlate the largest changes in sensor response to the intersection of magnetic circuit paths should provide an indication of the applied force location and magnitude. Magnetic flux has an affinity for high permeability materials (high relative to air), and this fact allows the design of pathways (using a ferrous material, in this case 1010 steel) to direct the flux flow to the sensors strategically located to measure the flux density change.

Figure 5 shows a possible magnetic 3 x 3, two-dimensional sensor array. At the base of the circuit a permanent magnet creates the field bias. On top of the magnet sits the 3 x 3 Galfenol rod array. Steel pathways complete the six, 3 x 3 circuit pathways from the tops of the rods, along to 2 sides of the array, and then back down to the magnet. The steel pathways are constructed with gaps at the +/- 45° to the grid axes in order to direct the flux flow along the grid axes. Each steel rod top is a separate piece so that when one rod is stressed the rod next to it is minimally affected. (Figure 5, Top View)

The flux density sensors are located at the side return paths on the top and sides of the circuit (see Figure 5). A load can be located on the grid by two sensors (one on the row

side and one on the column side) detecting a larger change in flux density than the other sensors in the row or column. These two sensors correlate to the loaded rod located at the intersection of the row and column flux paths along which they are attached. Figure 6 depicts an example of locating a loaded rod. By determining the loaded rod in this way, for an n x n array of rods only n + n sensors are required versus more conventional detection arrays in which a sensor would be dedicated to tracking permeability changes within each individual rod (= n^2). For example, a 10 x 10 array requires only 20 sensors instead of 100. This simplifies the amount of data acquisition required by the circuit and also helps minimize the mass and hardware complexity. Figure 7 shows a side view of Figure 6's row of rods with load applied to the center rod. The displacement under load causes stress to the rod and the domains begin to rotate. This changes the flux density in the rod and consequently how the flux travels through the circuit to the flux sensors.

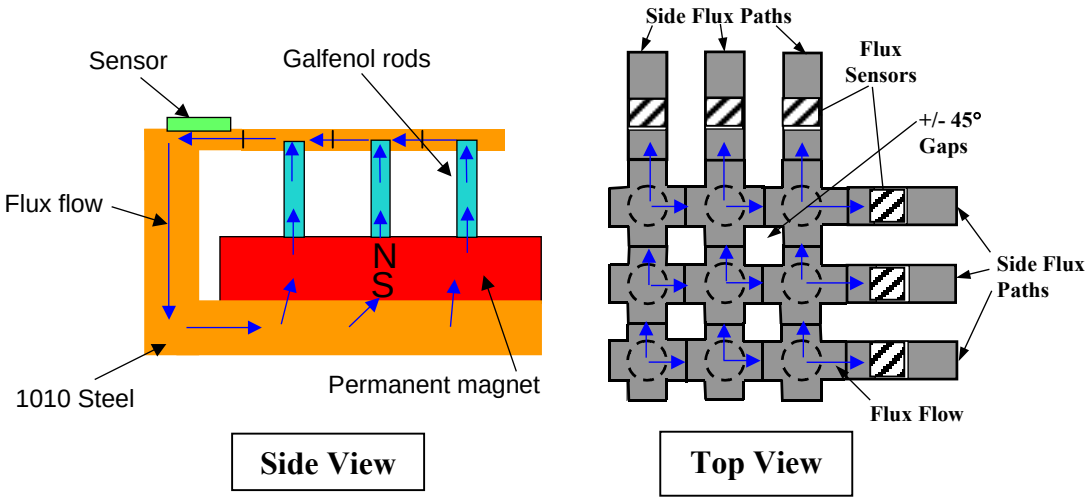

Figure 5. Side and top views of a 3 x 3 rod array magnetic circuit.

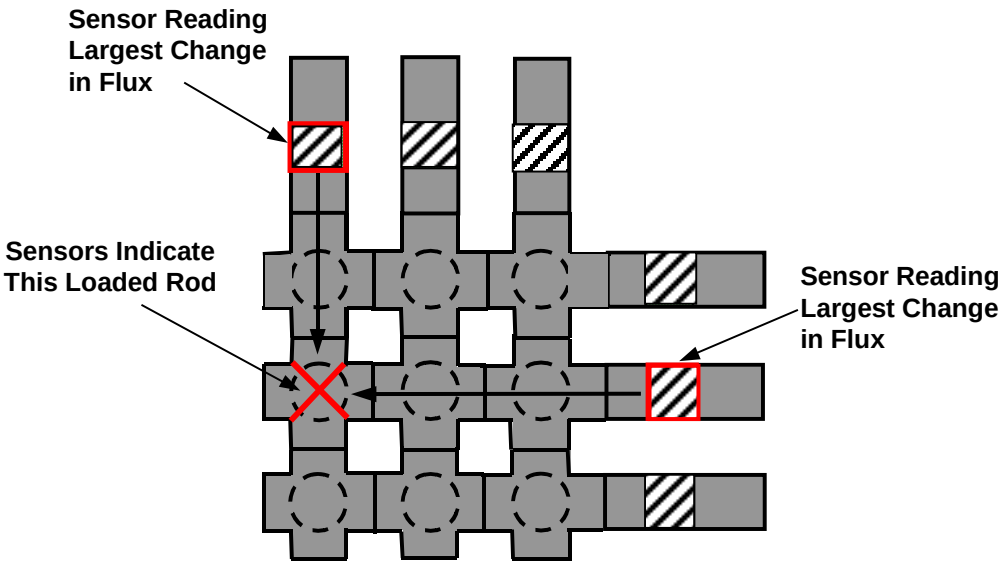

Figure 6. Sensor in row and sensor in column locating the loaded rod along their intersecting paths.

a)

b)

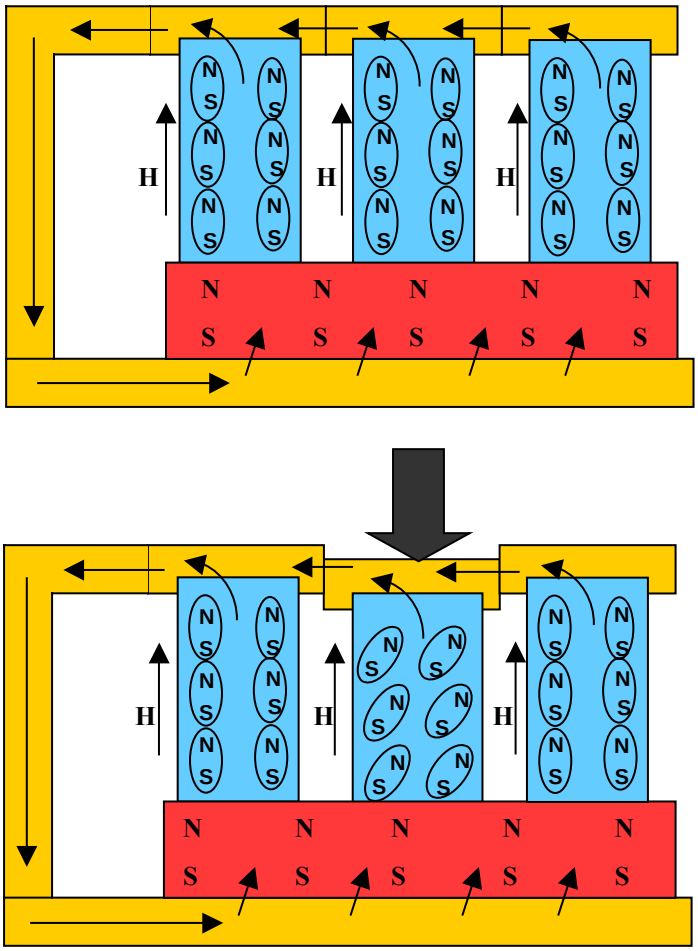

Figure 7. Side view of rods showing exaggerated view of magnetic domains within rods. a) Rods in unstressed condition. b) Center rod under load with domains beginning to rotate.

To detect the change in flux density within the steel flux paths, a type of sensor called a Giant Magneto-Resistive (GMR) sensor is used. The sensor measures the change in magnetic field along its "sensitive" axis and is relatively immune to changes along its other axes (Smith and Robert W. Schneider, 1999). Other means of measuring the change in flux density are Hall effect sensors and sense coils. GMRs were chosen over Hall effect sensors as GMRs have a higher sensitivity. Sense coils could be used, yet they require more data acquisition equipment and the GMRs provide a compact, easy-to-handle sensor package.

1.5 Summary

As can be deduced by this array configuration, the spatial resolution of the sensor is the distance between the centers of the flux pathways. The closer together the array of rods and flux paths can become, the higher the resolution capability. Therefore, by using Galfenol nanowires as mentioned earlier, the flux paths could be made smaller and the resolution of the sensor would greatly increase from that of mm to that of nanometers. Additionally, the Galfenol rods can be "grown" with small pieces of permanent magnet within the rod to provide the magnetic bias for each wire. Figure 8 shows an example of a magnetic multilayered wire.

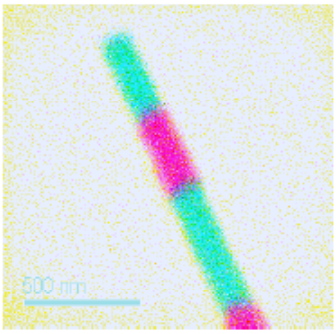

Figure 8. Example of a nanowire with magnetic multilayering (Cobian, 2004)

In all, this sensor array can provide tactile force feedback information by combining the characteristics of a magnetic circuit, the smart material Galfenol, and sensors. To maximize the information received from sensor array, the Galfenol rods should be biased to levels suitable for detection of a specific range of forces. As shown in Figure 4, with too high a bias level there is not much reaction until very high stress levels, and with close to no bias the range of stress the sensor can detect is very small. Based on Figure 4, to get good sensitivity for detecting stress levels ranging from 20 to 75 MPa, initial flux density values should be at levels produced by applied fields of 20 to 100 Oe.

2 PRELIMINARY MODELING AND DESIGN

2.1 Overview

In addition to the B-H and B versus stress data collected by Atulasimha shown in Figures 3 and 4, modeling of the magnetic circuit and sensor array was performed first to ensure a working design. Concepts used in the first prototype circuit design were based on results from these models. The model was used to compare asymmetric with symmetric circuit paths to determine locations of maximum sensitivity for using GMR sensors. GMRs measure the change in magnetic field, which is then used to calculate the magnetic density change. Due to the fact that the GMR sensors measures the field through a small air gap just above the steel magnetic circuit it is attached to and in a direction parallel to flux flow in the flux path, the measured field is equal in magnitude to the magnetic flux density in the steel path (Atulasimha, 2006).

2.2 Preliminary Circuit Optimization

Magnetic modeling is performed to optimize the circuit design for efficiency and for determining the best location for the GMR sensors. Both symmetric and asymmetric configurations were analyzed. Two software programs created by the company Integrated Engineering Software are used; Oersted (2-Dimensional) and Amperes (3-Dimensional). Initial modeling is performed using Oersted, and more accurate analysis is completed using Amperes. Oersted simplifies the circuit by assuming a constant design through a user specified depth.

In order to first get an idea of how flux travels through a magnetic circuit with two steel rods on top of a permanent magnet, a 2-D model (Figure 9a) was created and analyzed. Next, Figure 9b shows a 2-D model of an asymmetric, magnetic circuit with 2 Galfenol rods, under no stress, on top of a grade 1 ceramic magnet. B-H curves for Galfenol under various levels of stress were used to produce the model and were obtained from data collected and distributed in Atulasimha and Flatau, 2006.

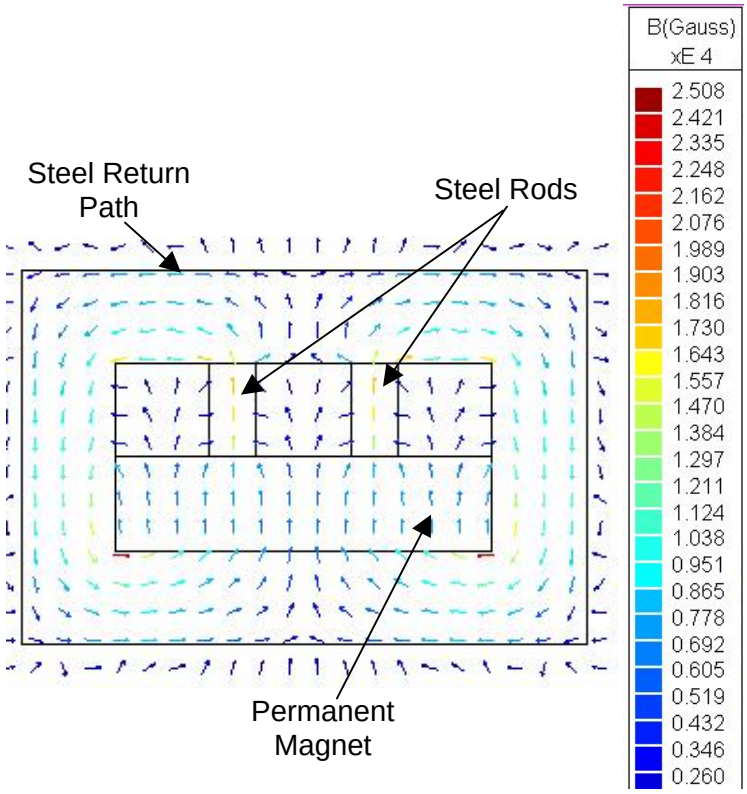

Figure 9a. A 2-D model of a symmetric magnetic circuit design using the modeling program Oersted.

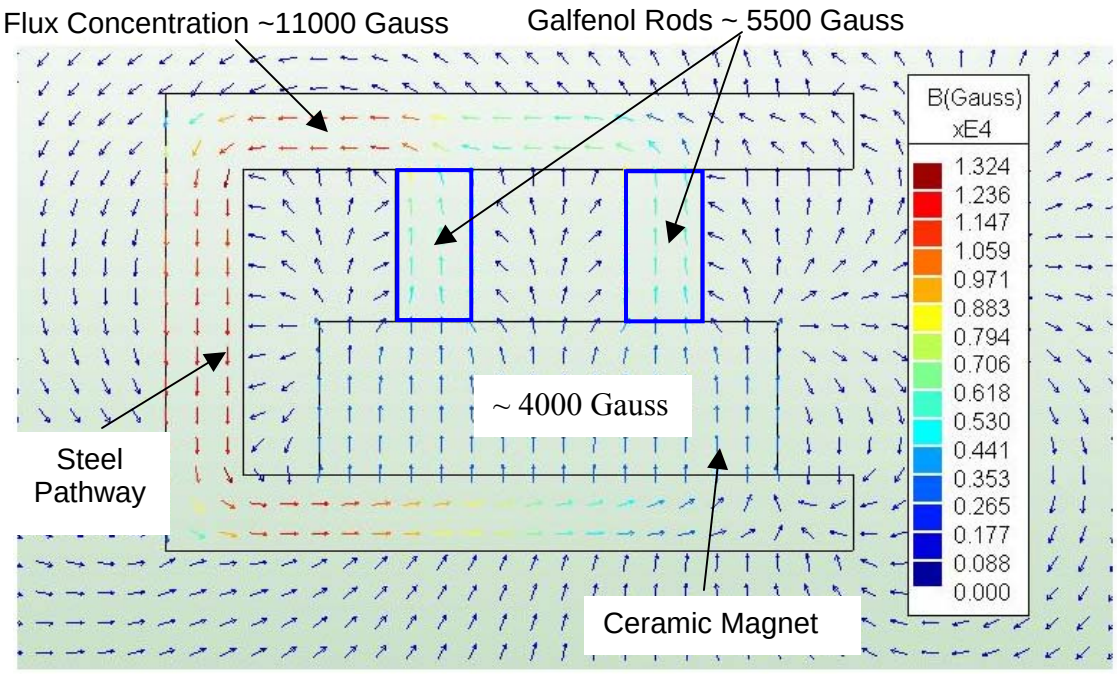

Figure 9b. Asymmetric, 2-D, model of the magnetic circuit design using the modeling program Oersted.

The analysis allows determination of where the maximum change in flux density occurs and therefore where the GMR sensor should be located. Modeling of the circuit also investigated symmetric versus asymmetric configuration of the flux return path using the 2-D program. With a flux return path on both the left and right sides of a row of rods (Figure 9a), the flux traveling up through the rods travels to the left and to the right depending on which side of the circuit the rod is closest to. The asymmetric circuit (Figure 9b), however, shows that the flux will travel in just one direction along the steel pathway that closes the circuit. Therefore, in order to minimize the number of sensors required, and to simplify the circuit, one return path was chosen for the circuit design to cause the flux to travel to one side only where one sensor will be located for an entire row of rods.

Additionally, as shown by the B-H curves for Galfenol in Figure 4, the permanent magnet should be of a strength that produces a bias in the Galfenol rods similar to a bias produced by 10 to 80 Oersteds in order that the domains will rotate and provide a change in magnetic induction when the material is stressed from 0 to 80 MPa. This analysis determined that a magnet of low strength should be used to obtain this bias range in the Galfenol rods. Ceramic magnets work well as they are a hard material and have a lower strength then rare earth magnets. Based on the above model, using a ceramic magnet of grade 1 should provide the initial flux density needed in the rods to allow sufficient changes in permeability for detection using GMR sensors when loading the rods between 20 and 80 MPa.

2.3 Prototype I Circuit Configuration

The circuit designed here was configured with the intent of creating a sensor with high sensitivity for a range of stresses readably achievable in the laboratory. Figure 10 depicts the final sensor array configuration. The sensor is made up of nine Galfenol rods of ∅3.1 mm (∅.125″) diameter by 6.4 mm (0.25″) long that are arranged in a 3x3 grid array. The rods are evenly spaced with a 4.8 mm (0.1875″) distance between rod centers. A permanent magnet produces the field bias.

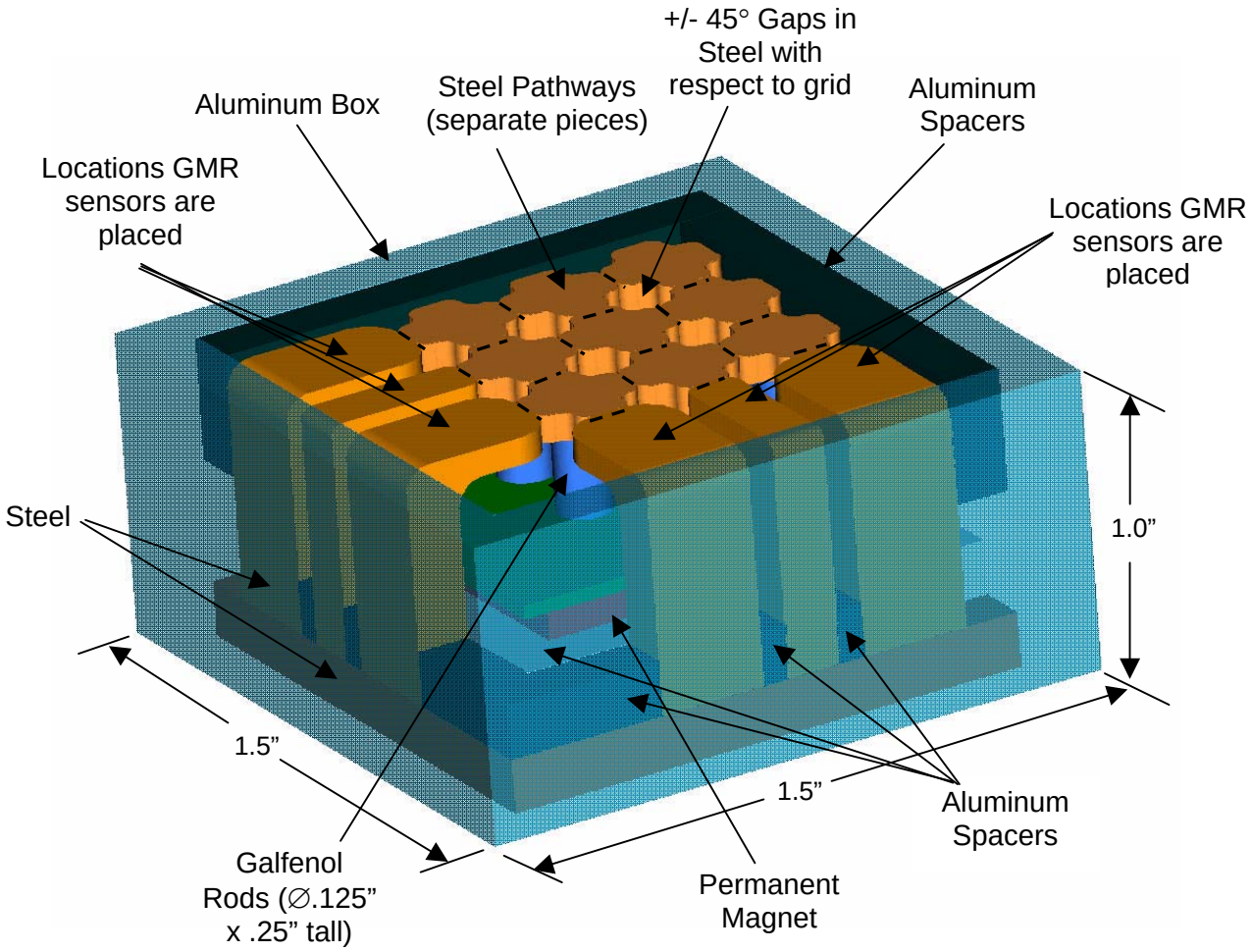

Figure 10. Circuit design

The magnetic circuit is completed with 1010 steel. The layer of steel at the top of the Galfenol rods is a group of steel pieces, placed together to create pathways to the sides. Each flux path is 4.8 mm (0.1875″) wide, which is the same as the distance between rod centers and the spatial resolution. This steel layer is made as separate pieces in order to allow force to be applied to one rod at a time without affecting the others. Also, these steel pieces are machined with small gaps at +/- 45° with respect to the grid, to encourage the flux to travel along the continuous paths in line with the grid axes (See Figures 7 and 10). The flux flow begins at the permanent magnet, which creates a magnetic field. Flux travels up through the rods and into the “rod tops” made of 1010 steel. Then the flux

moves laterally along the pathways created by the "rod tops." In general, flux flows along the shortest path possible to complete a circuit and along the path of greatest permeability and least reluctance. Therefore, in this circuit, flux travels along the flux paths and grid axes as steel has a higher relative permeability (μ_{steel}=1156) than air (μ_{air}=1). After passing through the top pathways, the flux then reaches the side steel paths and travels downwards through them to a bottom layer of 1010 steel. The flux moves through the steel and back to the magnet, which closes the circuit.

When building the first prototype it was necessary to use two magnets placed next to each other due to the way the magnet is manufactured and size constraints for seating the permanent magnet beneath the rods. Figure 11 depicts the magnets' configuration within the circuit. Due to each magnet having a magnetic orientation of North on the top half and South on the bottom half, they had to be pressed together by aluminum spacers in order to remain side by side.

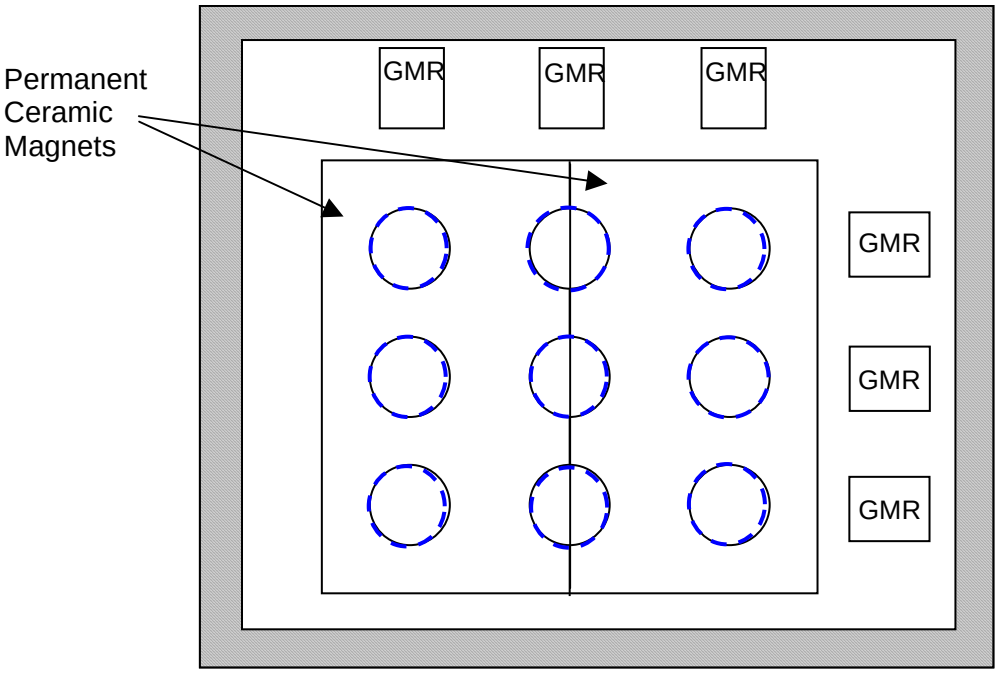

Figure 11: Overhead view of magnetic circuit showing the position of the two permanent ceramic magnets and rods. The locations where Galfenol rods will be placed are depicted by dashed circles.

The prototype I system used side steel paths of different widths due to the surface area thought to be required to mount the GMRs. The outside two side paths on each side wall were slightly wider than the center paths. Figure 10 depicts the side paths at these widths. The second prototype used a different attachment method for the GMRs which allowed the side paths to be fabricated to the size of the original, center side path. This ensured that the data collected by the GMRs was not affected by any difference in side path width.

The finite element model of the magnetic circuit discussed in section 2.1 was used to determine the optimal location for the GMR sensors. As shown in Fig 10, this was determined to be the area close to the side walls on the top of the flux paths.

Aluminum spacers separate the steel pathways on the sides of the circuit. The size of the spacers may be varied for investigation into the effect of separation distance between the steel paths on the flux density within the paths. This investigation was not performed here but is suggested for future research.

3 ANALYSIS OF PROTOTYPE I CIRCUIT DESIGN

3.1 No Load Circuit Analysis

Once the prototype I, asymmetric circuit design was chosen, a more detailed analysis was performed using Amperes. The following figures depict Amperes 3-D analyses results. Information on how the B-H curve of the Galfenol material changes due to applied stress was used in the model to investigate how the flux density changes at different locations when force is applied to one rod in the array. Figure 12 depicts the flux density in one row of Galfenol rods when the array is in the nominal, no stress configuration. The greatest flux density is shown to be along the top level of steel near the left side. This information supported the decision to locate the GMR sensor close to this location. Also, the flux density levels of 0.8 to 1.1 Tesla in the rods correlated to applied field levels of about 10 Oe (Figure 3), which according to Figure 4 should produce a change in flux density when the rods are subjected to stress levels ranging from 0 to 40 MPa. Figure 13 shows the flux density along the top steel pathways with no rods under stress.

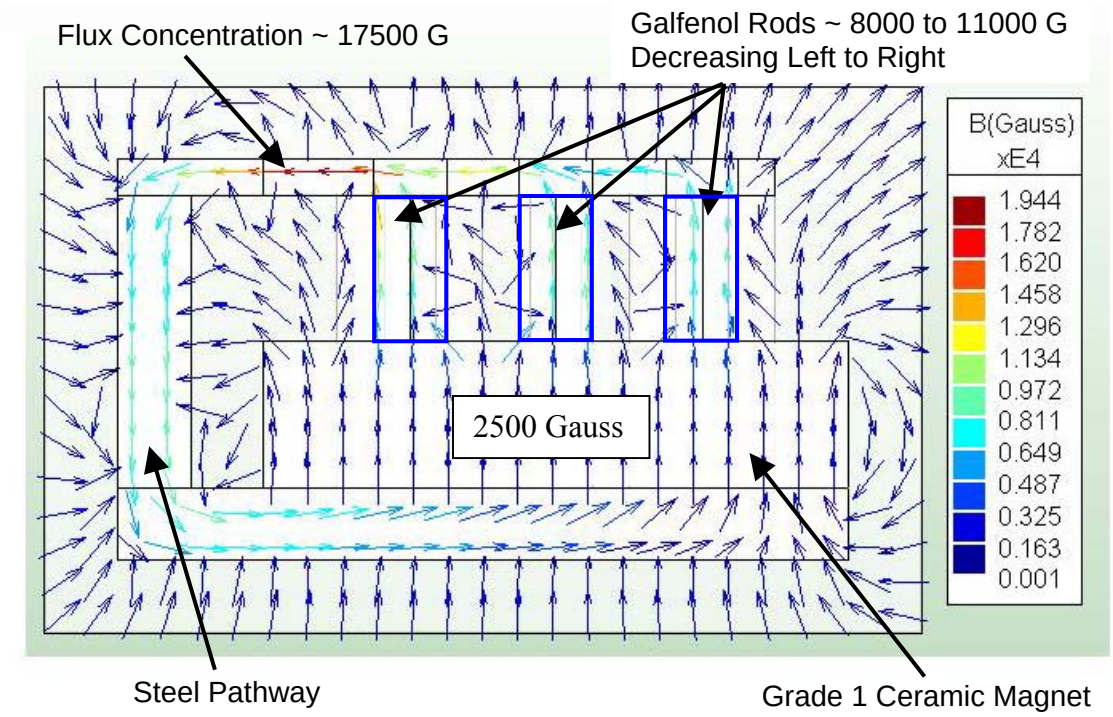

Figure 12. Side view of Galfenol rods under no stress using the modeling program Amperes.

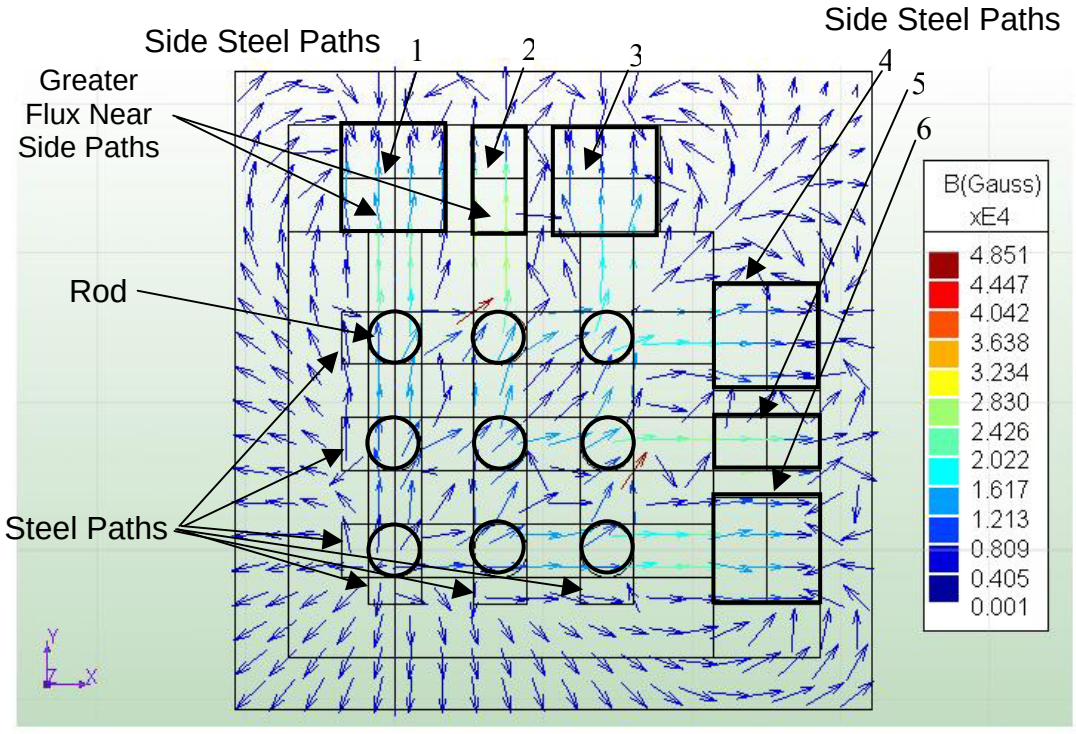

Figure 13. Top view of flux pathway along top of Galfenol rod array using the modeling program Amperes. No rods are under stress.

It should be noted that the flux density just outside the edges of the top, steel pathways was lower than the value of flux density within the rods (see Figure 12). Section 4.2 describes how measurements of the flux density were taken with a gaussmeter in this area before testing was performed in an effort to get an idea of the flux density within the rod.

3.2 Analysis of Circuit Under Load

The modeling shown here was performed using the 3-dimensional program Amperes and was used to simulate responses to the proposed loads numerically. Next, in Figure 14, the central rod was stressed to 15 MPa to determine the flux density change throughout the magnetic circuit (i.e. through the six side flux paths and all nine Galfenol rods).

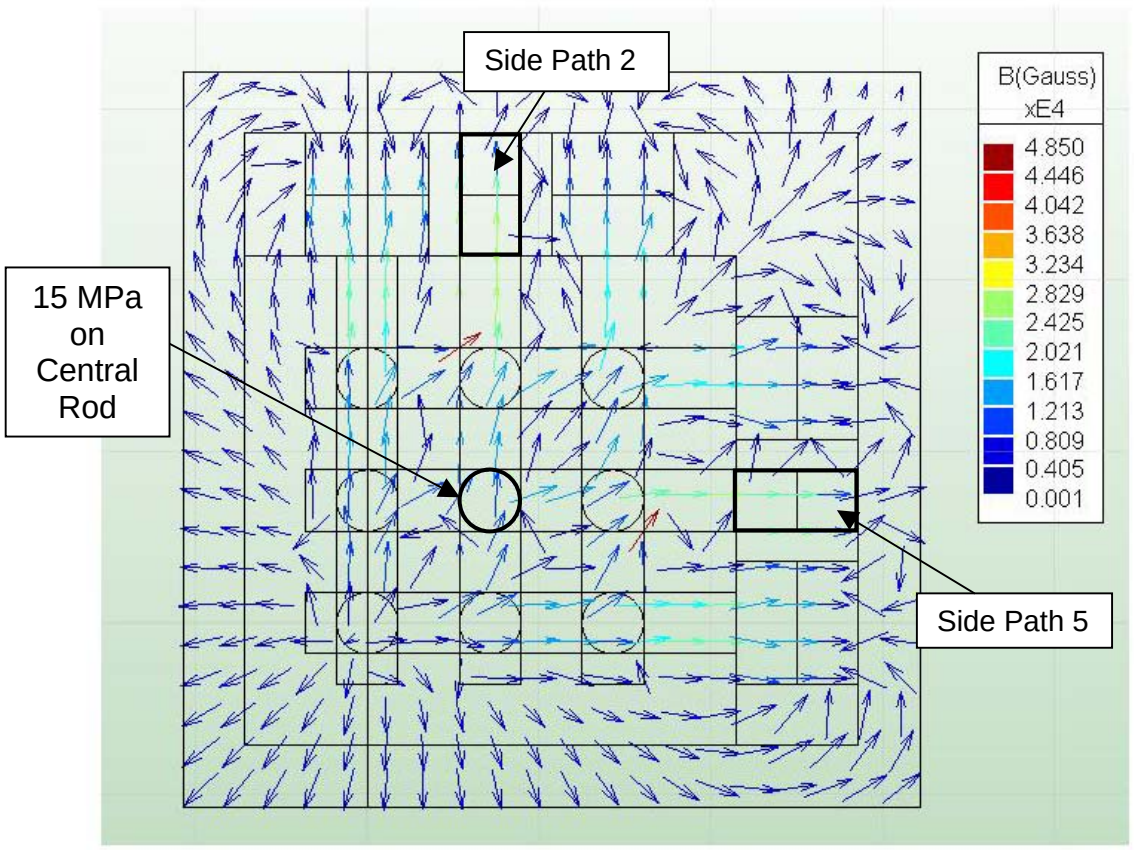

Figure 14. Central rod stressed at 15 MPa. Modeling performed using Amperes.

The figures show that the flux flow was indeed in the direction of the shortest path back to the magnet. Flux density values shown in Table 1 were taken from the modeling results shown in Figures 12, 13, and 14 in the steel pathways just above the central rod or just below at the proposed location for the GMR sensors as indicated. From these values, it is shown that the largest change in flux density was at the two side paths that intersect at the rod that was stressed. In this case, when 15 MPa of stress was applied to the central rod, side paths #2 and #5 changed by 5 Gauss whereas the other side paths changed by no more than 3 Gauss. These changes correctly indicated the central rod as being stressed, although the simultaneous and significant changes in flux through all other paths suggests that the 2 dimensional array appears to be more complicated than the single row of rods analyzed in Figure 9b. The flux density at the measurement location in the steel paths along which no loading occurs sometimes increases and sometimes decreases depending on the location of the loaded rod within the array. Testing of all the Galfenol rods under various loads is required to fully characterize the sensor circuit. In future work, sensitivity of the change in flux density at the GMR sensor locations to both the applied stress magnitude and strength of the initial magnetic bias field should be studied.

Table 1. Flux density values for central rod and side steel paths according to model

Location	Stress (MPa)	x(in)	y (in)	z (in)	Bm (Gauss)	Delta B (Gauss)
Top of Central Rod	0	0.500	0.500	0.625	5651	3362
Side Steel Path #1	0	0.250	1.125	0.688	379	3
Side Steel Path #2	0	0.500	1.125	0.688	**636**	**5**
Side Steel Path #3	0	0.750	1.125	0.688	295	1
Side Steel Path #4	0	1.125	0.75	0.6875	276	-3
Side Steel Path #5	0	1.125	0.500	0.688	**501**	**-5**
Side Steel Path #6	0	1.125	0.25	0.6875	340	-2
Top of central rod	15	0.500	0.500	0.625	9013	
Side Steel Path #1	15	0.250	1.125	0.688	382	
Side Steel Path #2	15	0.500	1.125	0.688	**641**	
Side Steel Path #3	15	0.750	1.125	0.688	296	
Side Steel Path #4	15	1.125	0.75	0.6875	273	
Side Steel Path #5	15	1.125	0.500	0.688	**496**	
Side Steel Path #6	15	1.125	0.25	0.6875	338	

4 PERFORMANCE OF PROTOTYPE I DESIGN

4.1 Set-Up

Six GMR sensors were placed along the outer perimeter of the circuit, one for each row or column of the steel pathways (Figures 15 & 16). The GMR sensors used were model number NVE AA-005-02 and had a linear range of 10 to 70 Oersteds. The sensors were powered using a voltage of 3.33V, and the signal was amplified by setting the gain to 10. Excitation and amplification was provided using the National Instruments SCXI-1121 module, -1321 terminal block and PCI-MIO-16XE data acquisition card. Labview was then used to record and view the change in field during testing. The field was then converted to flux density according to the fact that the measurement was taken in air, which causes the field to be equal to flux density in magnitude. One hundred samples were taken and averaged to produce one flux density value. The samples were filtered with a 4 Hz low pass filter.

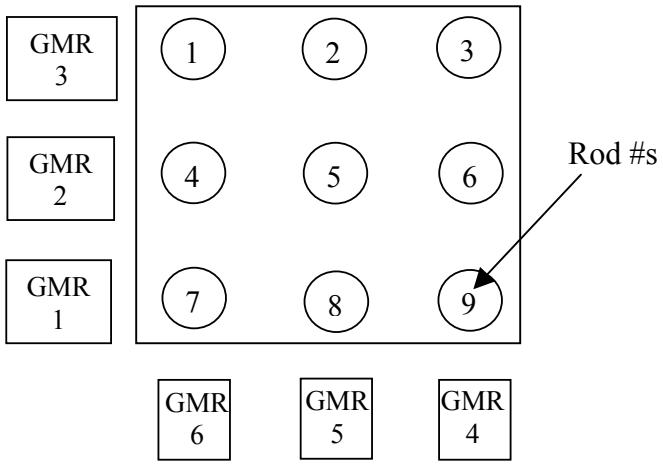

Figure 15. Intended design for rod and GMR sensor configuration in magnetic circuit (note all GMRs were equal distance from rods).

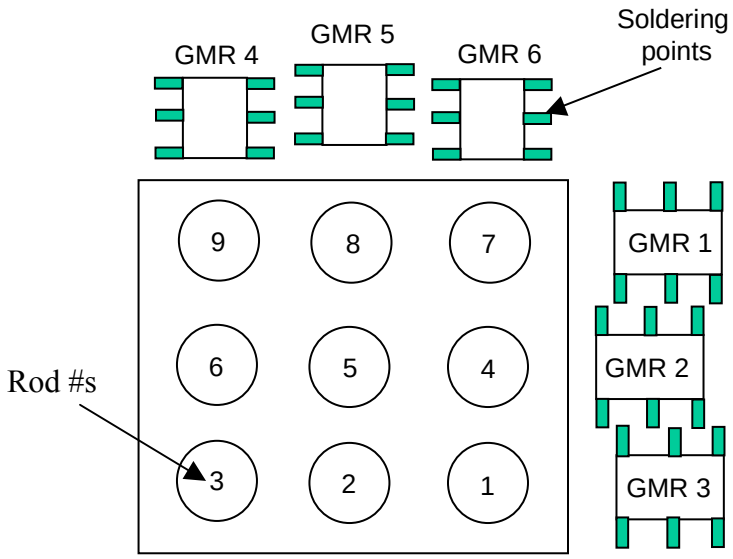

Figure 16. Depiction of GMR soldering points and as-built GMR configuration (staggering of GMRs required).

Figure 15 shows the sensor array with the intended GMR sensor design. However, as shown in Figure 16, the soldering points extrude from the GMRs, and due to the small distance between the rods (0.1875″), the GMRs were staggered to prevent the solder tabs from contacting one another, which would produce erroneous readings. It is important to note that this staggering caused the GMRs to be different distances (~0.1 inch difference) from the rods, which may have been a factor in the measured flux density data values changing differently than expected. Figure 17 shows photographs of the sensor array system.

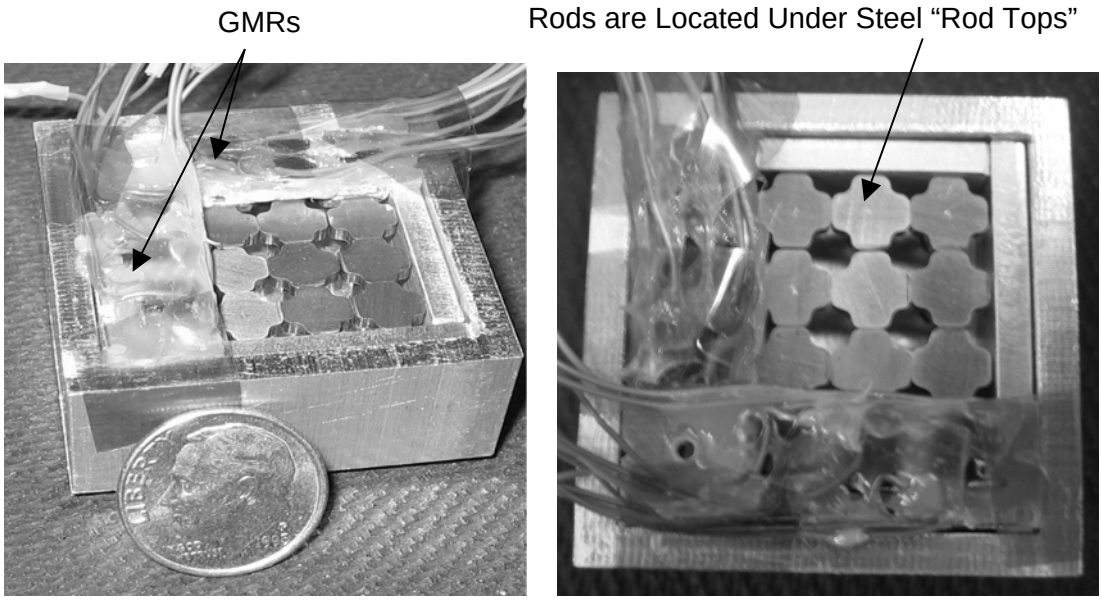

Figure 17. Isometric and top views of sensor array.

Figure 18 displays the flux density levels measured in the air just above each steel rod top while the rods were under the permanent magnet bias.

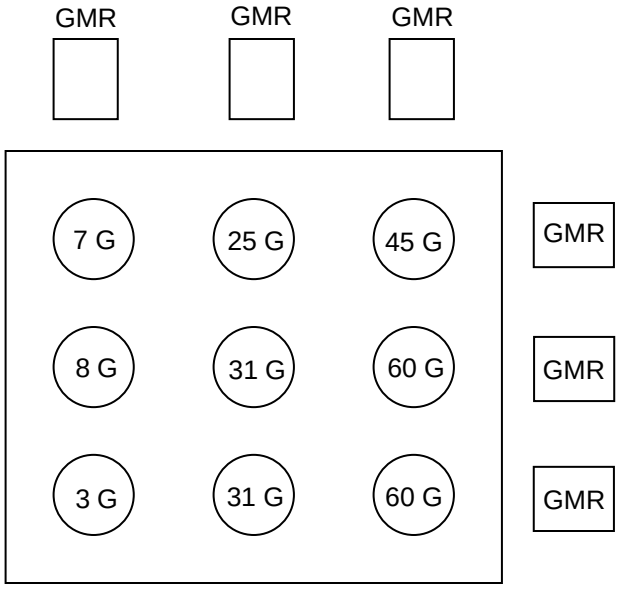

Figure 18. Flux density in air (Gauss) measured with a gaussmeter at the tops of the rods while under no stress.

As mentioned in section 1.2, flux density values were measured just above the flux return paths above the rods using a gaussmeter. The gaussmeter recorded the flux density parallel to the axes of the rods. The probe tip of the gaussmeter was held as close as possible to the flux paths above the rods, but an air gap did exist between the probe tip and the flux paths due to the orientation of the probe tip and the circuit's small hardware. It should be noted that the flux density levels measured in air above the rod tops was much lower than the flux density within the rods since the majority of the flux will remain in the more permeable steel. The measured values are close to the values predicted in air in the calculated models depicted in figures 9b and 12. Therefore, according to the models, the flux density values detected in air above the rod tops indicate that the fields in the rods were within the sensitive range given by Figure 4. According to Figure 4, magnetic fields from about 20 to 100 Oe should produce good sensitivity to stress loads up to 80 MPa and most all the rods shown in Figure 18 fell within this range. The lower initial biases shown in Figure 18 would be verified to be within the sensitive range by testing.

4.2 Initial Experiments

Static and dynamic loads were applied to rods in the 3 x 3 grid array. Static loading was applied to each rod in the 3 x 3 array, and dynamic loading was applied to certain rods in the 3 x 3 grid array and also to rods in a simpler 2 x 2 array. Experiment procedures, analyses, results, and possible errors from both loading types are discussed in the following sections.

4.2.1 Static Loading

The first set of tests was run on the circuit by loading a rod and recording the GMR response. Each rod was first loaded individually to 31.1 N (7 lb_f) and 57.7N (13lb_f) which induced 3.9 MPa and 7.6 MPa of stress respectively. Loads were applied using a small loading apparatus that placed weight on the steel rod top piece located at the top of each individual rod. The stress levels induced rotated the magnetic domains in the loaded Galfenol rods (as depicted in Figures 2 and 4) and therefore should have changed the field that the GMR sensors recorded. The field change was then converted to flux density for analysis. The resulting data was analyzed to determine if the loaded rod was correctly identified.

4.2.2 Static Loading Analysis

Tables 2 and 3 list the change in flux density for each rod when loaded statically to 3.9 MPa and 7.6 MPa, respectively. For data in these tables, GMR sensors 1 through 3 detected changes in the rows while sensors 4 through 6 detected the column changes. By choosing the GMR with the largest change in flux density out of the two sensor sets, it was expected that the intersection of their respective flux paths would locate the loaded rod. Tables 2 and 3 highlight the highest change in flux density values for each sensor set for two loadings of each rod and also state the expected GMR indications and the actual indications. The rightmost column indicates whether or not the loaded rod was correctly identified.

Table 2. Flux density change calculated from field change recorded by GMR sensors when rods were stressed to 3.9 MPa. Here the fields are measured through a small air gap (μ=1), and so the field and flux density magnitudes are equal (see equation 1).

				Delta Flux Density						Expected GMR Indications	Actual GMR Indications	Correct?
	Rod	Force (N)	Stress (MPa)	GMR 1 (Gauss)	GMR 2 (Gauss)	GMR 3 (Gauss)	GMR 4 (Gauss)	GMR 5 (Gauss)	GMR 6 (Gauss)			
Loading 1	1	30.8	3.9	**1.816**	0.079	0.194	**0.448**	-0.200	-0.218	3,6	1,4	n
	2	31.2	4.0	**-1.120**	0.279	0.109	**0.745**	-0.200	-0.200	3,5	1,4	n
	3	31.0	3.9	-0.412	0.279	**1.096**	**1.919**	0.036	0.212	3,4	**3,4**	Y
	4	30.9	3.9	2.961	**8.676**	0.545	**8.180**	-1.514	5.213	2,6	2,4	n
	5	30.9	3.9	-0.333	**1.320**	0.073	**0.872**	-0.557	0.642	2,5	2,4	n
	6	31.1	3.9	**-0.866**	-0.236	-0.327	**4.559**	-0.133	-1.193	2,4	1,4	n
	7	31.4	4.0	0.206	**0.387**	-0.194	2.755	-0.133	**8.737**	1,6	2,6	n
	8	31.4	4.0	**0.890**	0.745	0.478	2.313	0.854	**5.025**	1,5	1,6	n
	9	31.0	3.9	0.472	0.763	**1.235**	0.345	0.581	**1.102**	1,4	3,6	n
Loading 2	1	31.0	3.9	1.241	0.624	**2.737**	**1.865**	0.200	0.406	3,6	3,4	n
	2	31.0	3.9	**3.463**	0.515	0.412	0.327	**0.503**	0.472	3,5	1,4	n
	3	31.0	3.9	**0.636**	0.291	0.394	**1.090**	0.254	0.254	3,4	1,4	n
	4	31.0	3.9	2.712	**7.895**	1.259	**5.715**	-0.551	4.172	2,6	2,4	n
	5	31.1	3.9	**2.949**	2.385	1.162	**2.961**	0.115	1.120	2,5	1,4	n
	6	31.2	3.9	0.727	**1.344**	0.612	**3.736**	0.969	1.623	2,4	**2,4**	Y
	7	31.4	4.0	0.484	**1.187**	0.418	0.006	0.575	**4.795**	1,6	2,6	n
	8	31.4	4.0	-0.527	-0.230	**0.896**	0.351	**5.322**	-5.316	1,5	3,5	n
	9	31.1	3.9	**1.992**	1.744	1.574	-0.472	1.495	**2.712**	1,4	1,6	n

Table 3. Flux density change calculated from field change recorded by GMR sensors when rods were stressed to 7.6 MPa. Here the fields are measured through a small air gap (μ=1), and so the field and flux density magnitudes are equal (see equation 1).

			Delta Flux Density						Expected GMR Indications	Actual GMR Indications	Correct Indication ?
Rod	Force (N)	Stress (MPa)	GMR 1 (Gauss)	GMR 2 (Gauss)	GMR 3 (Gauss)	GMR 4 (Gauss)	GMR 5 (Gauss)	GMR 6 (Gauss)			
1	59.7	7.5	3.736	3.384	3.808	4.559	3.627	3.342	3,6	3,4	n
2	59.8	7.6	2.385	1.659	2.283	4.329	2.428	2.507	3,5	1,4	n
3	59.9	7.6	1.356	1.380	1.253	6.490	2.101	1.368	3,4	2,4	n
4	59.8	7.5	0.163	2.052	1.495	-2.918	1.072	2.531	2,6	2,6	Y
5	59.9	7.6	0.224	-0.963	1.084	4.880	2.373	1.980	2,5	3,4	n
6	60.0	7.6	0.030	-0.884	0.503	6.448	1.193	1.671	2,4	3,4	n
7	60.2	7.6	0.339	0.357	2.101	6.206	4.880	4.377	1,6	3,4	n
8	59.8	7.5	-1.078	0.321	0.285	6.236	2.597	1.962	1,5	2,4	n
9	60.0	7.6	0.720	0.521	0.769	-1.828	0.369	1.132	1,4	3,6	n

As shown by the results in Tables 2 and 3, only two rods at the 3.9 MPa stress level and one rod at the 7.6 MPa stress level were correctly identified. It should also be noted that under loading, some GMR sensor readings increased while others decreased. Also, of the sensors 4 thru 6, during the 3.9 MPa loading GMR 4 or 6 records the most change almost every time. As will be discussed in detail in section 4.3, the low number of correct identifications and lopsided number of maximum flux readings by certain sensors is

believed to be at least partly due to the fact that the steel rod tops were separating during loading. This had a profound effect on the path that the flux traveled and so altered the results from those expected. Exactly how the separating of rod tops affected the flux flow in the sensor array is investigated in section 4.3.

4.2.3 Dynamic Loading

After static loading, dynamic loading was performed on the 2 x 2 array shown in Figure 19. Testing was performed on a 2 x 2 array (rods taken out of 3 x 3 to create 2 x 2 array) in order to simplify the circuit and produce correct rod identifications under load. Loading was performed by hand using a wooden rod (non-magnetic material) and pressing the rod down and releasing about 3 to 5 times. First each rod in the 2 x 2 array was dynamically loaded and then each rod in the 3 x 3 array was loaded. Lastly, pairs of rods in the 2 x 2 array configuration were dynamically loaded at the same time. Results and discussion follow.

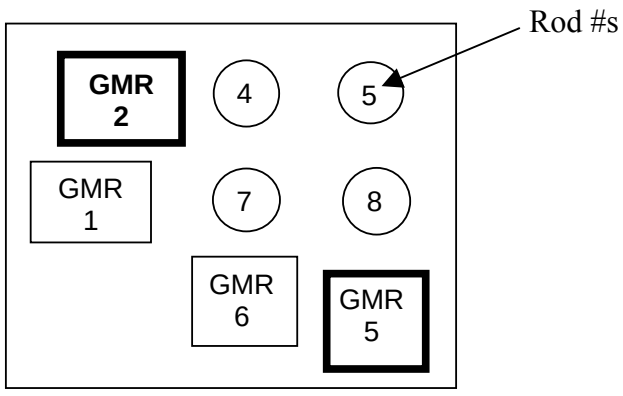

Figure 19. Depiction of 2 x 2 grid array of Galfenol rods to show numbering scheme and staggering of GMRs.

Figures 20 and 21 depict the dynamic loading results for rods 4 and 7, respectively. Figure 20 shows that rod 4 was correctly identified by the GMR sensor data, which showed the greatest frequency and amplitude of change during loading on sensors 2 and 5. The correct sensor information for rod 7, however, was not as obvious, which may be due to the fact that GMR 2 was located closer to the rods than GMR 1 and the rod tops were separating during loading. Another error that became apparent from this testing is the drift most noted in GMR sensor 2 in Figures 20 and 21. This was likely also due to the rod top separation issue.

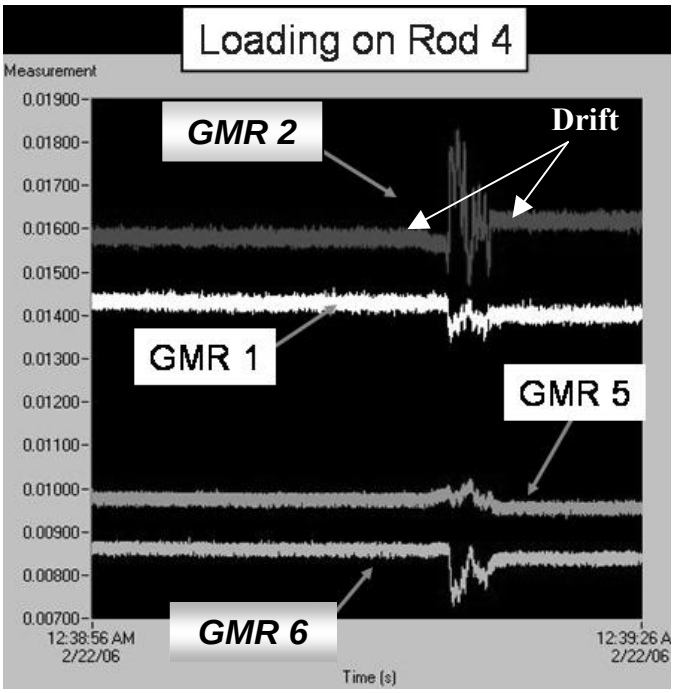

Figure 20. Dynamic loading on rod 4 (correct indication by GMRs 2 and 6).

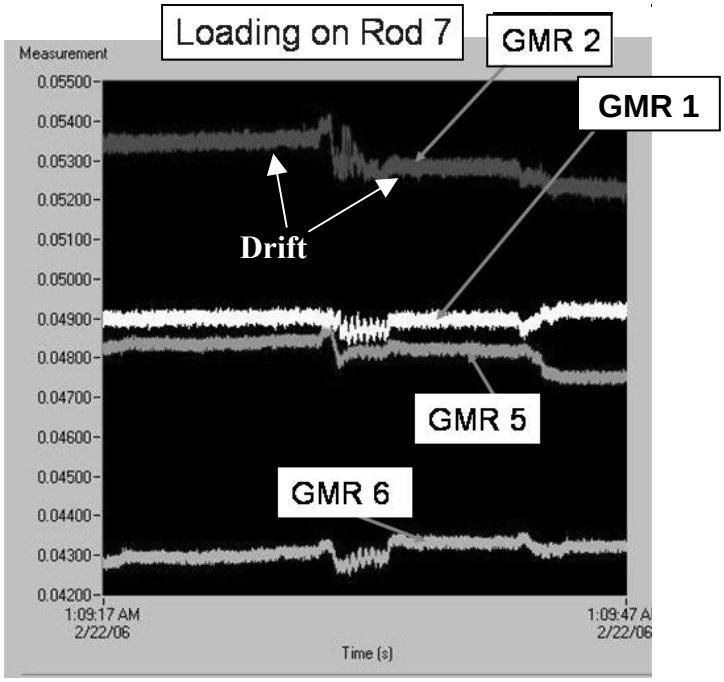

Figure 21. Dynamic loading on rod 7 (should be indicated by GMRs 1 and 6).

Figure 22 shows results for dynamic loading on rod 1 in the 3 x 3 rod array in Figure 16. GMRs 3 and 6 should have given the greatest signal response, however it was not apparent that this was the true from the data collected. As was also the case for rod 7, incorrect rod identification was possibly caused by rod top separation and/or the GMR sensor staggered positions relative to the rods.

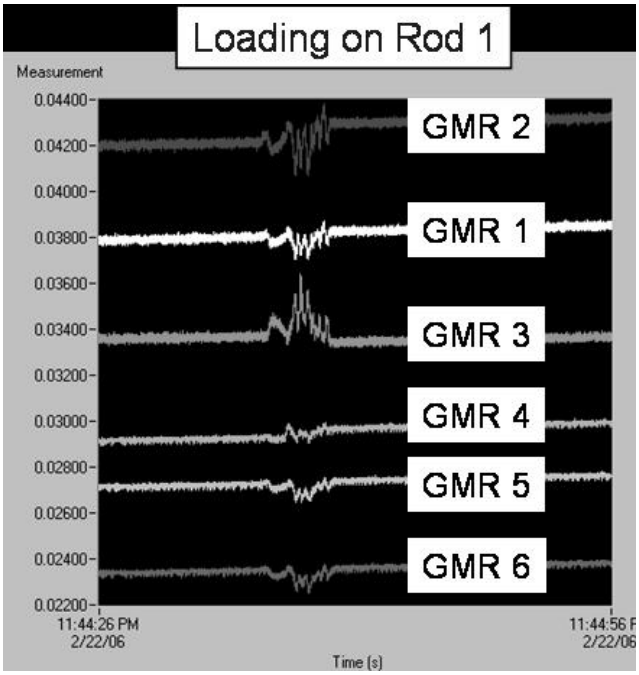

Figure 22. Loading on rod 1 in 3 x 3 grid array

Simultaneous loading on two rods was also performed. This experiment occurred in the 2 x 2 grid array and gave correct indications. One example of a simultaneous loading that occurred was with rods 4 and 5. A strong signal was recorded in GMR 2 and in GMRs 5 and 6 as expected.

The initial set of experiments did not consistently identify the rod placed under load. Rod top separation and the fact that the side paths were different widths likely induced error. Rod top separation was the creation of air gaps between the steel return paths on top of the rods during loading. Additional modeling was performed in order to verify the effect of the rod top separation. The modeling and its results are discussed in section 4.3. Modifications were made to the circuit design in order to minimize these error avenues and will be discussed in Chapter 5.

4.3 Modeling of Rod Top Separation

In order to qualify the effects of the steel rod tops separating, magnetic modeling was performed with one rod top separated from the others along one surface. Rod 2's steel top was modeled as separated from the center rod top by inserting an air gap 0.006″ wide between the two tops. This gap size was used as it created a definite separation between the rod tops and was an estimate from the tolerance build up in fabrication of the rod tops that could have allowed such a gap. In the nominal, unstressed condition, the separation of the steel rod tops causes the flux density distribution to change drastically. Figure 23 shows the rod order with the GMRs and the gap location. Figures 24a and 24b show the difference in flux density distribution between the connected rod top configuration and the separated rod top configuration. Note that due to rod 2's top separation from rod 5's top, the flux from rod 3 does not even pass through rod 2's steel top (even though it is one of the shortest return paths) but instead all flux travels through rod 6's steel top. Also, it can be seen in the model that the amount of flux traveling over rod 5 in the center decreases when rod 2 separates. It is clear from this model that any rod top separation will greatly affect the GMR readings and therefore which rod is indicated as being loaded.

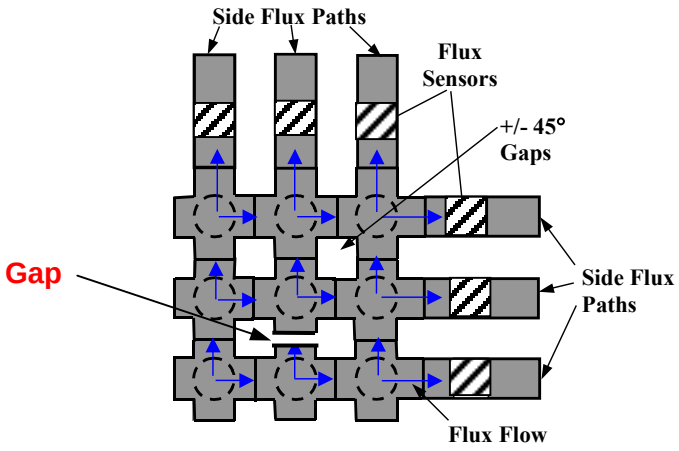

Figure 23. Rod order with GMRs.

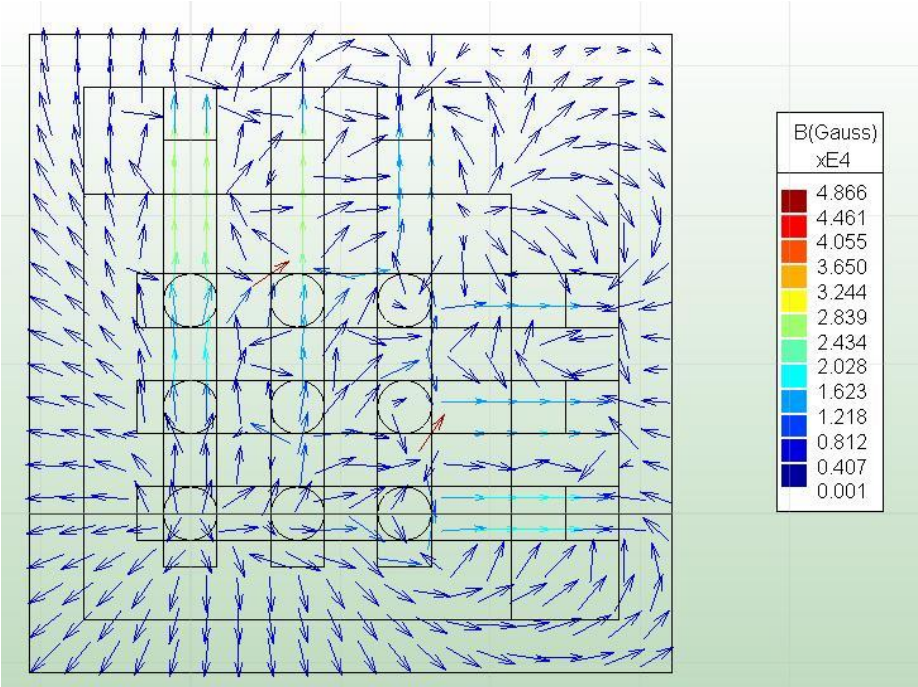

Figure 24a. Nominal flux distribution while rods are under 0 stress using 3-D modeling program Amperes (medium density of arrows shown).

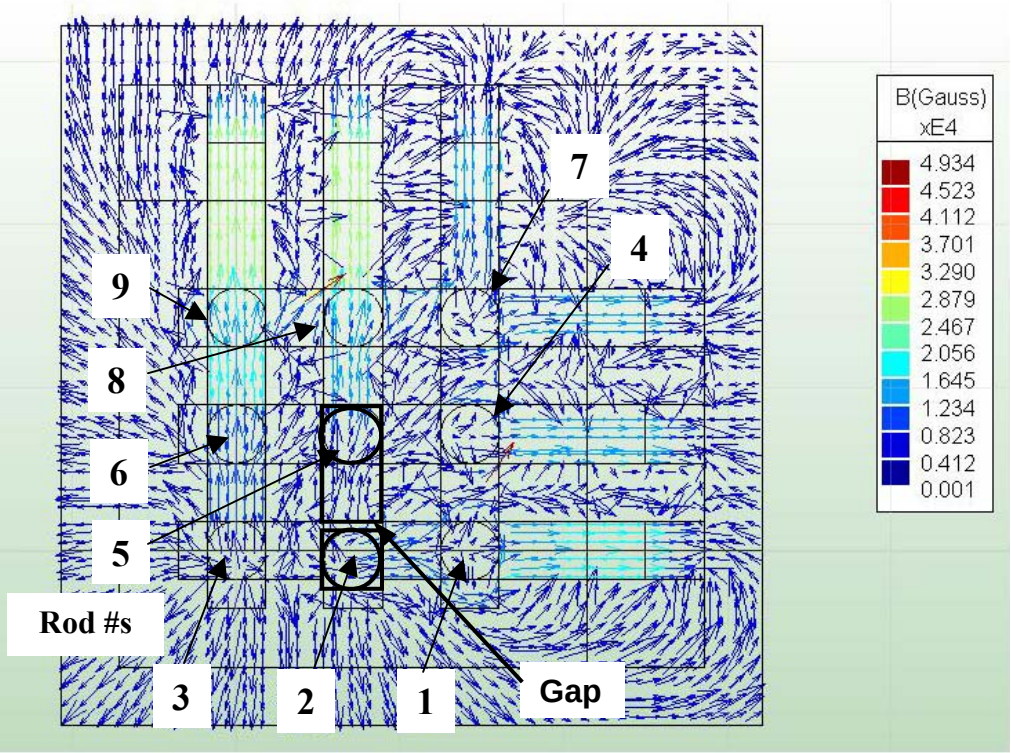

Figure 24b. Rod 2's top separation from rod 5's top using the 3-D modeling program Amperes (fine density of arrows shown for more detail).

5 PERFORMANCE AND ANALYSIS OF PROTOTYPE II

5.1 Set-up

The circuit was redesigned and modified to minimize the possible areas for error. The side paths were machined to the same width (initially the center side path was slightly wider than the others) and the GMR sensors were reattached and positioned so that they all were the same distance from the edge of the side path. The GMRs were attached directly to the top of the side wall piece instead of mounting all three to a particle board first. The direct attachment allowed the space needed to prevent the solder points from touching. Grease with iron filings was inserted at the edges of all the rod tops to prevent gaping during loading. Data was then collected using the new set-up.

Once the circuit was reassembled with the new modifications, a Tinius Olsen loading machine was configured and a rod, made of G10 (a non-magnetic, woven glass, epoxy resin material), was used to apply load to the rods (See Figure 25). Additional data acquisition devices were also mounted in the circuit. Three strain gages were mounted to rods 3, 5, and 7 along one diagonal of the sensor array as shown in Figure 26. Also, a sense coil was placed around rod 3 and another around rod 5 to record their flux density change as they were stressed. Rod 3's coil had forty-six turns and rod 5's coil had fifty turns. Once the circuit was assembled, grease was added to the edges of the rod tops.

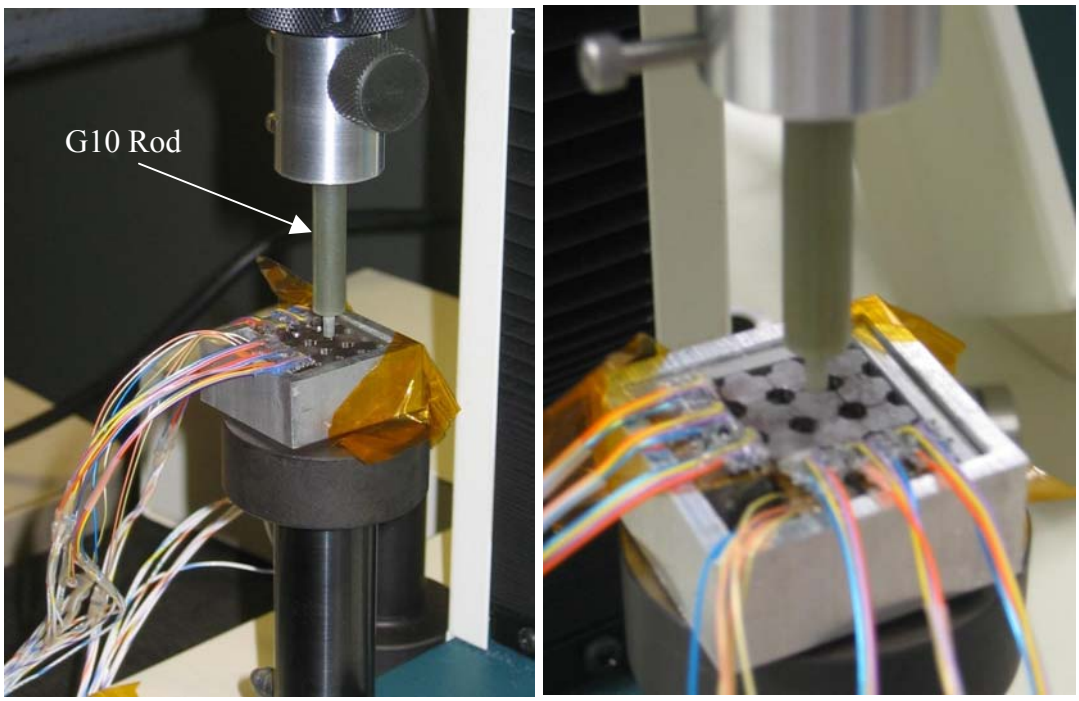

Figure 25: Galfenol Circuit Array on Tinius Olsen Loading Machine.

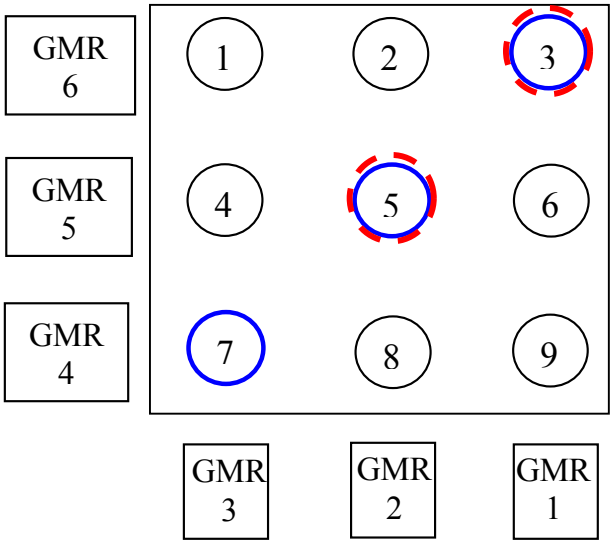

Figure 26: Strain gages on rods 3, 5, and 7, and sense coils on rod 3 and 5.

5.2 Acquisition Results and Discussion

With the sensor array reconfigured and new data acquisition devices attached, a second set of data was collected at four larger loads than used in the previous study: 311, 445, 528, and 578 N (70, 100, 120, and 130 lb_f). These forces translate to stresses of 39.3, 56.2, 66.7, and 73.0 MPa (5.7, 8.1, 9.8, and 10.6 ksi) respectively. The stresses were chosen to fall within the sensitive range (20 to 80 MPa) as shown in Figure 4. Each rod was individually loaded and unloaded at two rates of 0.1 in/min and 0.2 in/min using the Tinius Olsen machine. These loading speeds were chosen as they provided sharp changes in field that were easier to measure with the GMRs, rather than more gradual changes recorded at slower loading speeds. Lastly, individual rods were loaded in circuit arrays only containing a single row or column of rods in an attempt to simplify the circuit and understand the system better. Analyses and results follow.

Figures 27 a, b, and c show the GMR data for all 6 pathways as rods 3, 5, and 7 were unloaded from 66.7 MPa at 0.1 in/min. Figures 28 a, b, and c show the strain data at these loads. Figures 29 a and b depict the sense coil data for rods 3 and 5 loading to and unloading from 73 MPa.

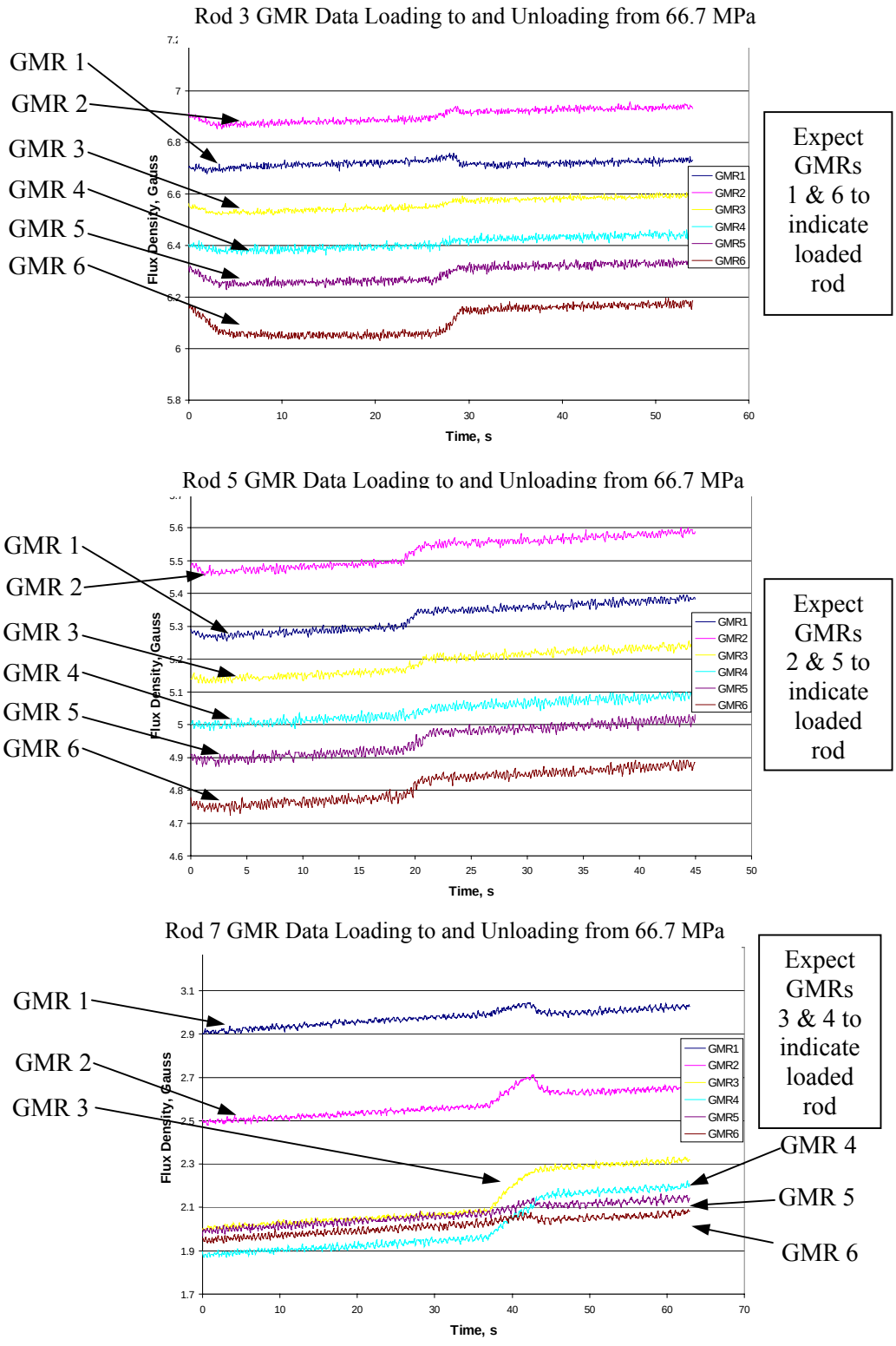

Figure 27 a, b, and c, GMR data when unloading rods 3, 5, and 7 respectively from 66.7 MPa at 0.1 in/min.

Figure 27a shows that when rod 3 was loaded, the GMR response seems to be equal between GMRs 1 and 2, but had a strong (correct) indication from GMR 6. Therefore, the response indicated the loading was applied to either rod 3 or rod 2, or possibly distributed on both rods. When rod 5 was stressed, GMRs 2 and 5 were expected to exhibit the maximum changes, but Figure 27b showed that similar responses were seen in GMRs 1 & 2 and in 5 & 6. Therefore the single rod that was loaded could not be determined. As shown in Figure 27c, stressing rod 7 gave strong correct indications in GMRs 3 and 4 as expected. However, there was also a notable response in GMRs 1 and 2. Again, the correct rod indication was not possible.

Also seen in Figures 27 a, b, and c is the drift from the GMR sensors. This drift is much smoother than the discrete jumps seen in Figures 20 to 22. This indicates that the rod top separation problem was successfully addressed. The drift seen in Figures 27 a, b, and c, is due to the inherent drift in the strain gage and data acquisition system. In order to minimize drift, the data acquisition equipment was run for about 15 minutes before collecting data in order to allow the system to thermally stabilize. The remaining drift was small over the short period of time it took to load and unload and so was ignored in data results.

Strain data was also recorded by the strain gages attached to the rods. As can be seen in Figures 28 a, b, and c, the strain decreases as a rod is unloaded from 66.7 MPa. The amount that the strain changes from the unloading varies between the rods. The strain recorded in rod 3 changes much less than that for rods 5 and 7. This may be due to the

fact that rods 5 and 7 had a greater initial flux densities as suggested by axial fields of about 30 Oe and 45 Oe respectively in air above their rod tops, than did rod 3 with only a 5 Oe field above its rod top. According to Figure 2, a lower magnetic bias in the rod would have caused rod 3 to have a shorter initial length than rods 5 and 7. This may explain why rod 3 compressed less than rods 5 and 7. Also note the strain values did not increase linearly with the increase in initial flux density values.

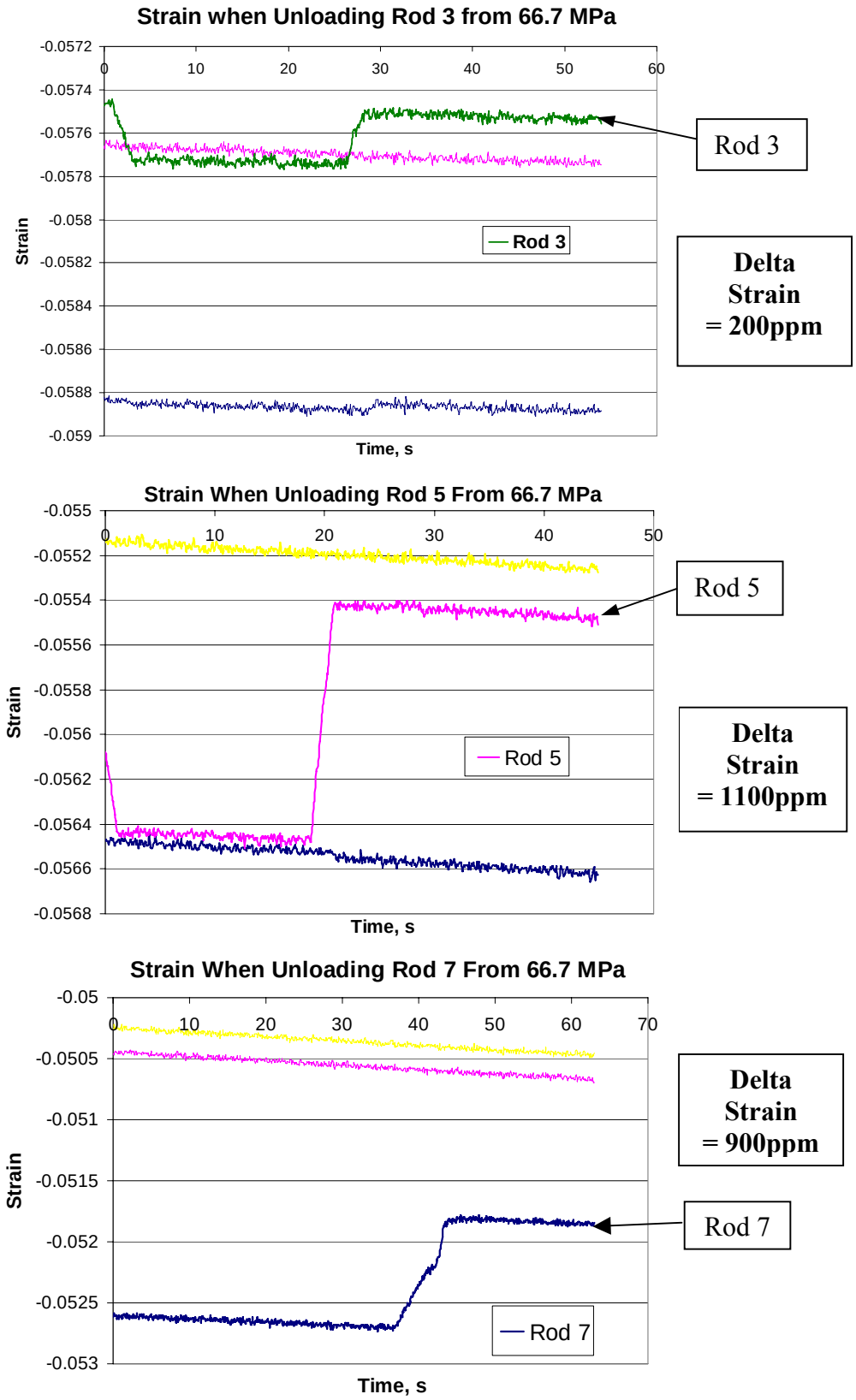

Figure 28 a, b, and c. Strain data for rods 3, 5, and 7 respectively, as each respective rod was unloaded from 66.7 MPa.

The change in flux density in a rod while it underwent a change in load was obtained using sense coils. Results are shown in Figures 29 a and b for flux density change while loading and unloading rods 3 and 5. As shown in the figures, the change in flux density was about 0.04 Gauss for both rods when loading to 73 MPa. The fact that rods 3 and 5 did have a notable change in flux density confirms that the rods were indeed cut from a section of bulk polycrystalline material with favorable crystallographic orientation. The smaller GMR and strain changes when loading rod 3 must then be due other reasons such as the smaller initial flux and/or unanticipated magnetic circuit behaviors.

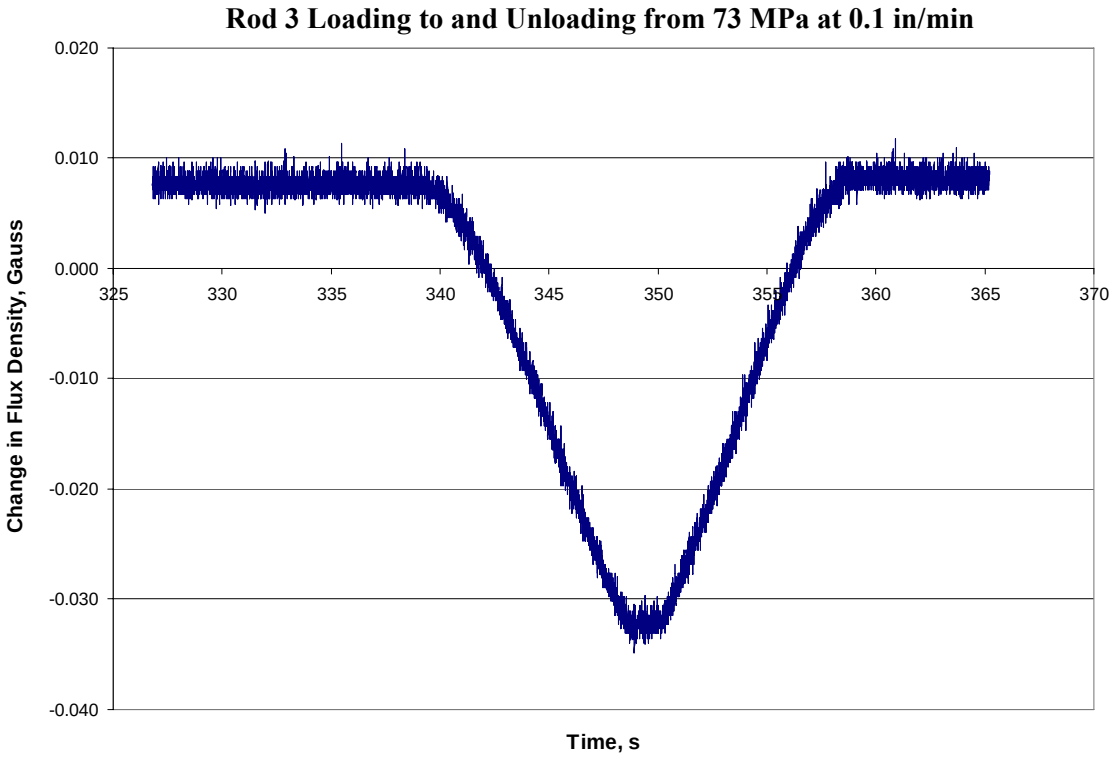

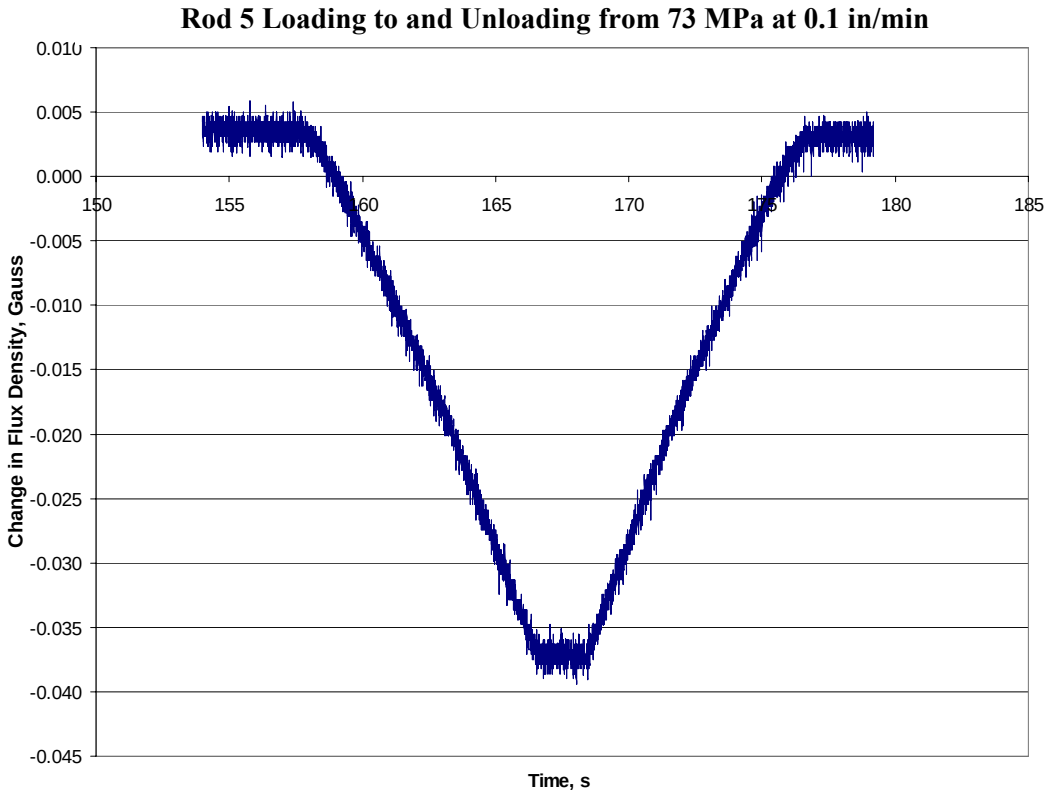

Figures 29 a. and b. Sense Coil Data for Rods 3 and 5 Loading to and Unloading from 73 MPa.

Figure 30 shows that rods 3 and 5 have very close to the same change in flux density for comparable loads of up to 70 MPa.

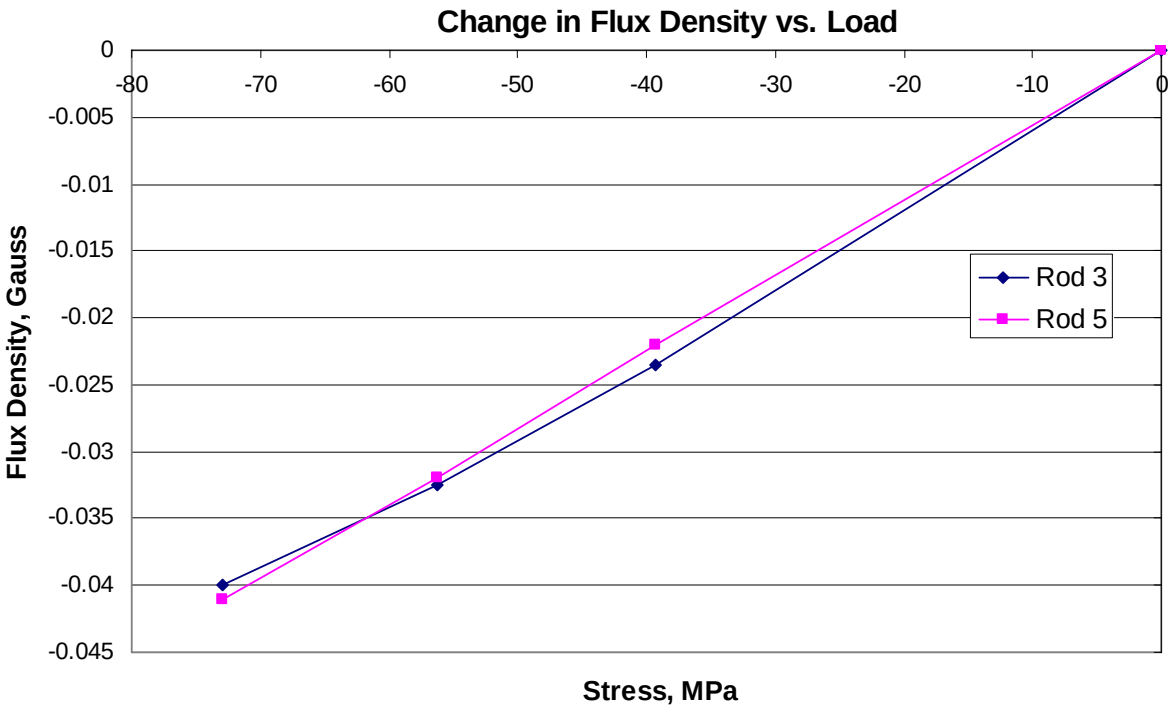

Figure 30. Change in flux density over stress levels for rods 3 and 5.

Considering that this change in flux density for rods 3 and 5 is small compared to the expected levels from Figure 4 and the additional facts of the small change in GMR voltage when the rods are loaded and the non-linear behavior of strain change vs. initial flux density levels, a single row of three rods was examined with the other rods taken out in order to simplify the circuit. The bottom horizontal row containing rods 7, 8, and 9 was chosen as all three rods have about the same level of measured flux density in air above their rod tops in this row configuration (depicted in Figure 31). The flux density

measurements were taken with the field lines parallel to the rod length just above the rod tops.

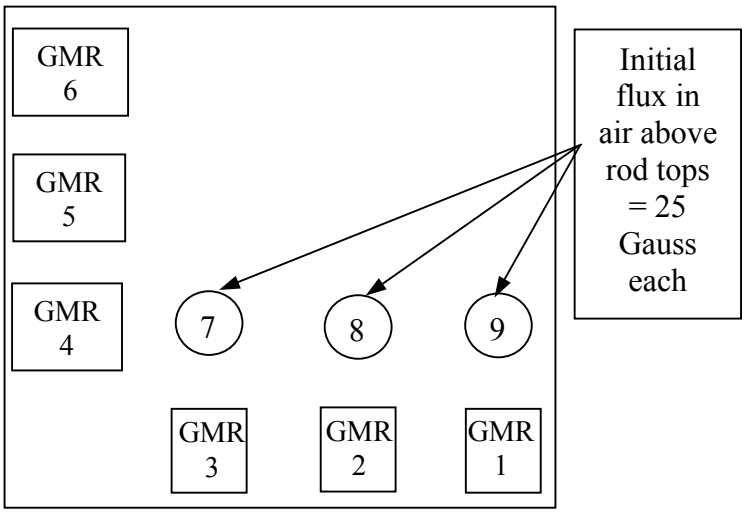

Figure 31. Configuration of rods with approximately equal flux density above rod tops (~25 Gauss).

A third sense coil was made (50 turns) and attached to a rod so that flux density changes could be recorded simultaneously for the row of three rods. Each rod was loaded to 39.3, 56.2, and 73.0 MPa and the flux density change was recorded. Figures 32 a, b, and c display the results.

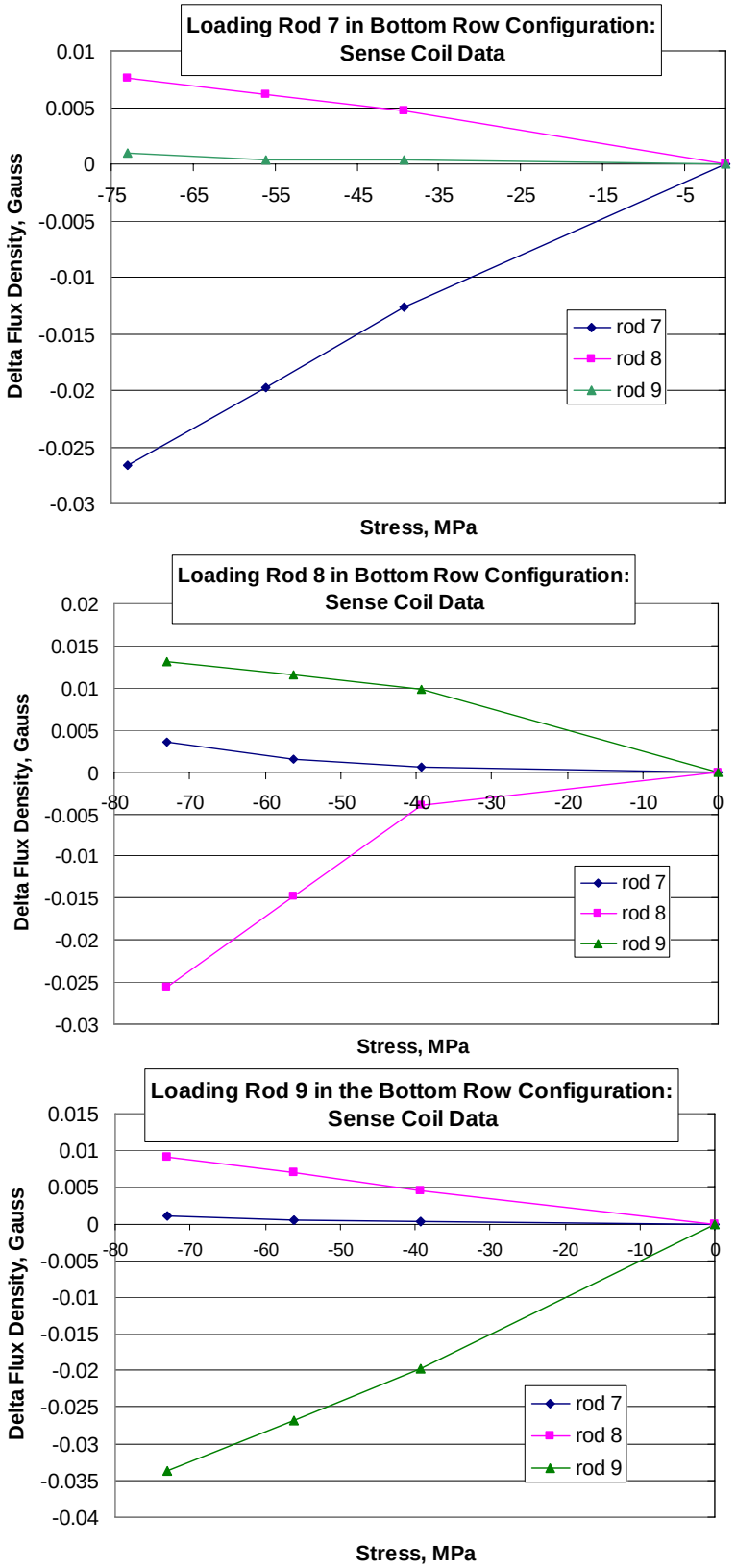

Figures 32 a, b, and c. Flux density change data collected using sense coils when loading rods 7, 8, and 9 respectively, in the lowest row configuration (as shown in Figure 31).

Figures 32 a, b, and c show that the rod stressed had the greatest change in flux density. While the flux density through the stressed rod decreased, the flux density through the other two rods in the row increased. When a rod on the end of the row (either rod 7 or rod 9 in this case) was loaded, the rod next to it (rod 8 in this case) increased more in flux density than the rod further away did.

Figure 33 takes the data for each rod that was individually loaded from the data displayed in Figures 32 a, b, and c and graphs them together for comparison. Rod 9 had the greatest change overall, while rod 8 changed slightly less than rod 7.

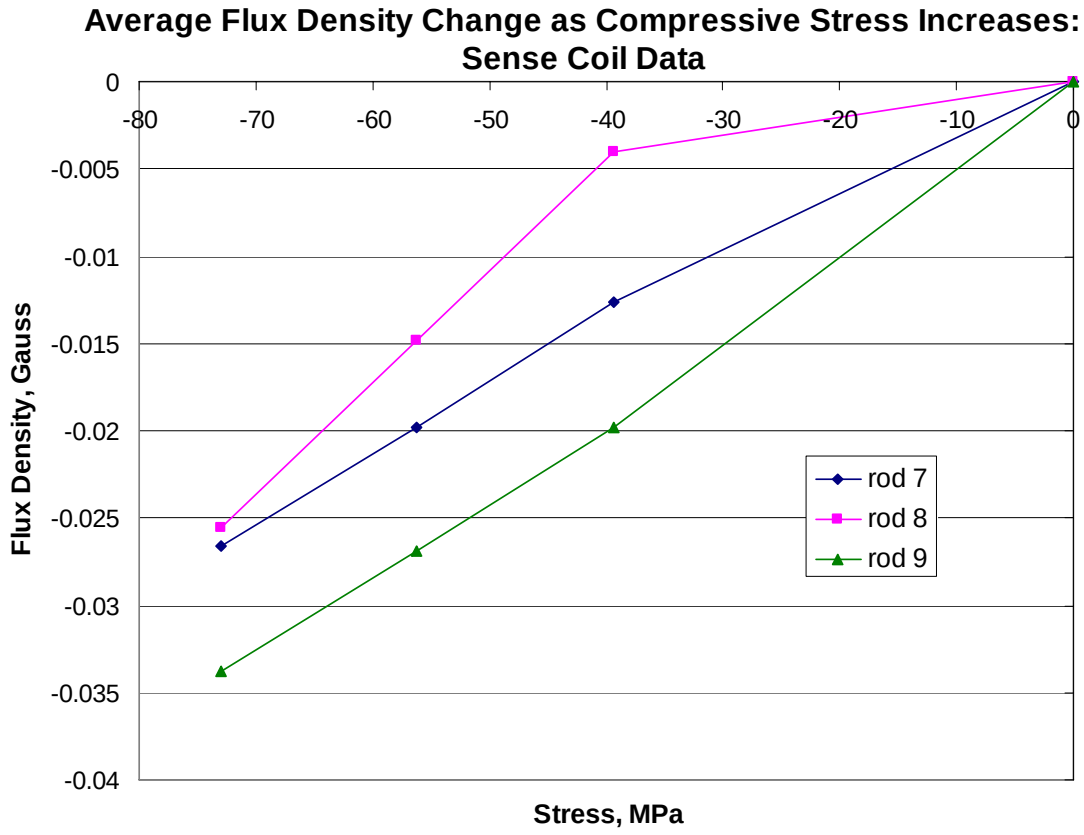

Figure 33. Flux density change for individual compression of rods 7, 8, and 9 at 39.3, 56.2, and 73.0 MPa.

A peculiar thing occurred when loading rod 8. As the rod was loaded, the flux density first greatly increased or decreased and then the opposite occurred before it reached its goal load of 39.3, 56.2, or 73.0 MPa. Then as the rod was unloaded the same occurred in the opposite order. See Figure 34 as an example of this behavior when rod 8 was loaded to 39.3 MPa and rod 7's sense coil recoded flux density change.

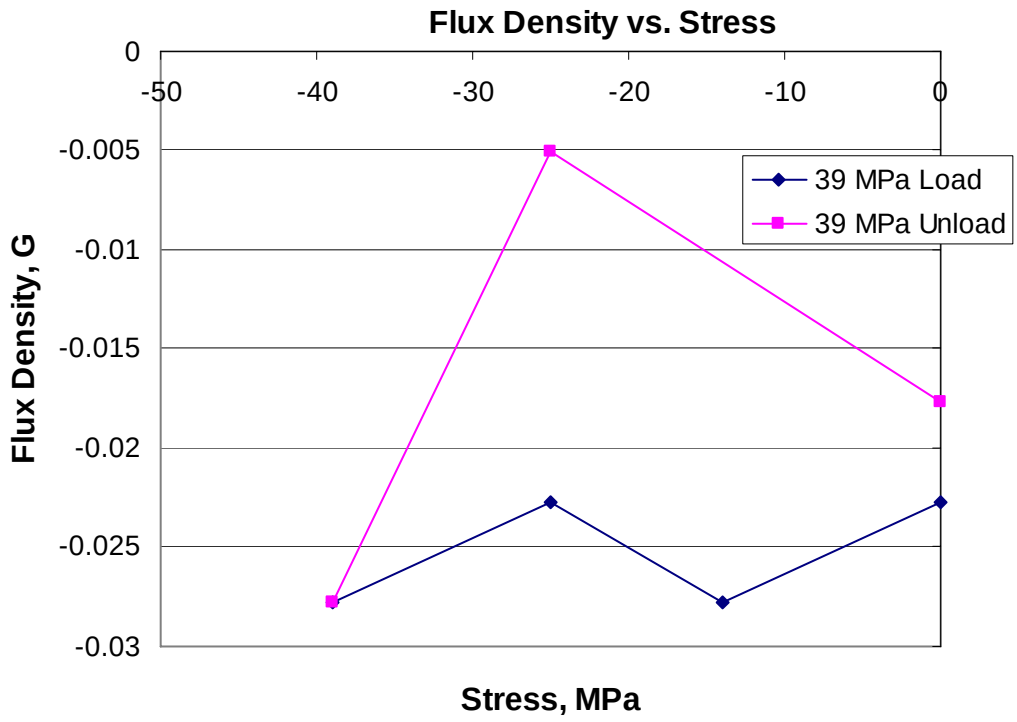

Figure 34. Data collected from a sense coil around rod 7 as rod 8 was loaded to and unloaded from 39.3 MPa.

A possible explanation for the flipping behavior was initially thought to be related to fact that the magnetic bias in the circuit was provided by two permanent magnets placed next to each other, and perhaps loading was introducing a gap at the magnet-to-magnet interface. Rod 8 sat right on top of this junction (Figure 35).

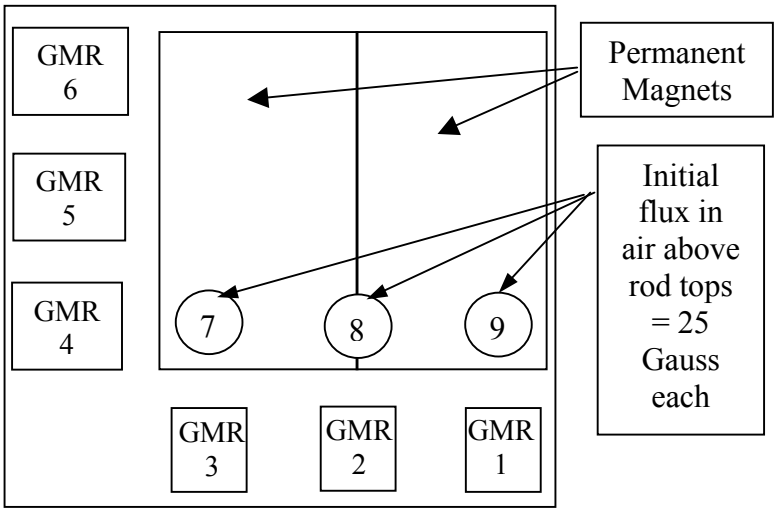

Figure 35. Depicting the location of rod 8 on the junction of the 2 permanent magnets.

In order to test this theory, another row of rods was analyzed. The row of rods 4, 5, and 6 were tested to look for the flipping behavior (Figure 36). Flipping occurred when the rod 5 was loaded, and also occasionally when rod 4 was loaded. Next the column of rods 3, 6, and 9 were tested (Figure 37a).

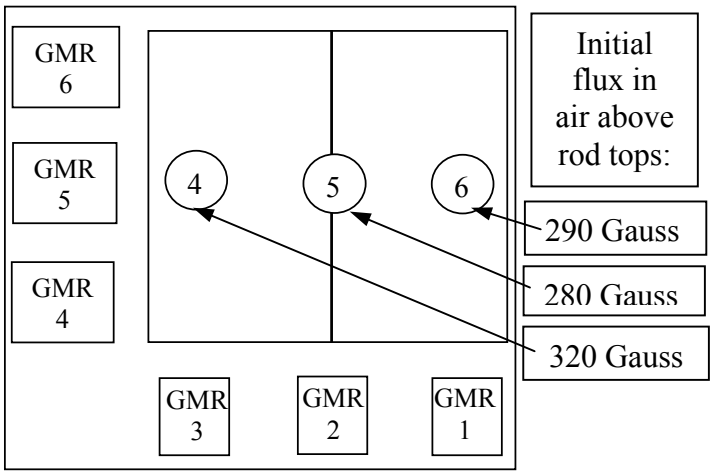

Figure 36. Center row of rods loaded to analyze flipping seen in sense coil data; initial bias levels are listed.

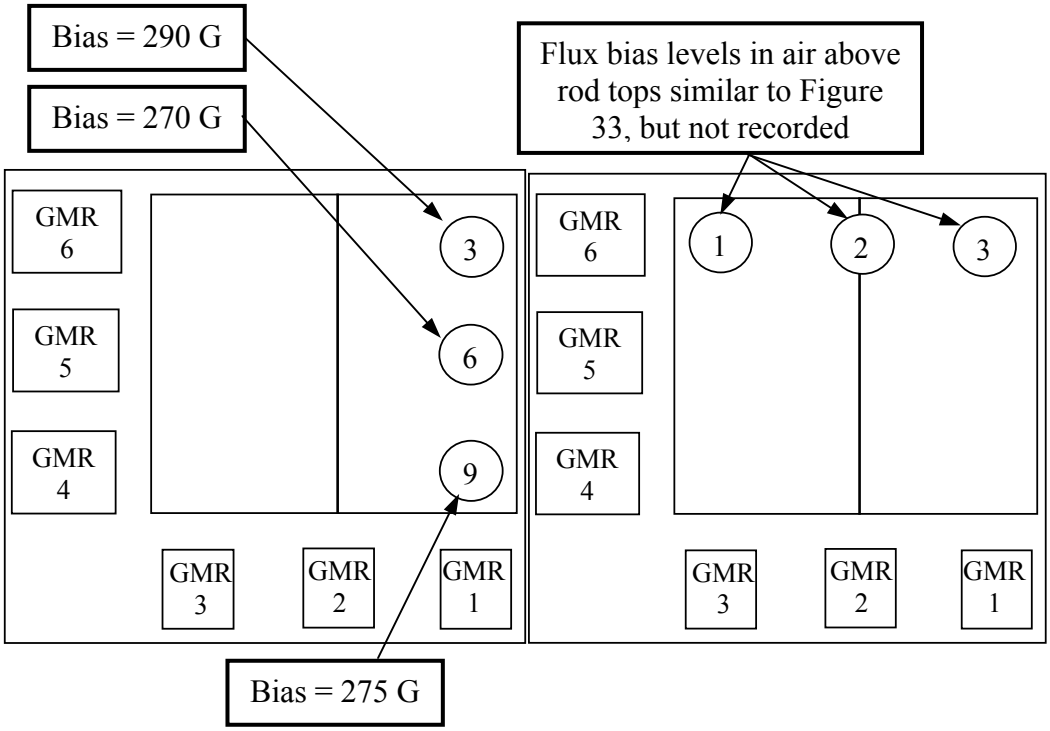

Figure 37 a and b. Additional column and row of rods analyzed for sense coil data flipping.

No major flipping behavior was noted when loading the column of rods 3, 6, and 9, although a small drop or increase (± 51 G), from the nominal value of 300G, occurred at the start of most loadings. This small initial change is likely due to the initial forcing of the rod tops down on the Galfenol creating a better surface contact and not the magnet junction. Next the row of rods 1, 2, and 3 was loaded (Figure 37b). No flipping was seen to occur in the sense coil data.

Due to the fact that flipping was not seen in all rows that crossed over the junction between the two magnets, the first row analyzed (row containing rods 7, 8, and 9) was again loaded to see if the flipping would occur again. This time the flipping did not occur.

During previous loadings of the different rods in the various rows and columns analyzed, on occasion, the flux density through the sense coil would indeed flip, but only during the first loading. The sense coils on the rods take up a lot of space along the rod and it is possible that the flipping noted initially is due to the rod top not seating correctly. Therefore, there seems to be no issue with using two magnets placed next to each other, but that sense coils and strain gages placed on the rods should be done so that the rod tops can seat completely and have complete surface contact.

A set of GMR and sense coil data was collected for the single column of rods 3, 6, and 9. Flux density levels in the air just above the rod tops and parallel to the rod lengths were 300 Gauss for rod three, 275 Gauss for rod six, and 270 Gauss for rod 9 (Figure 38).

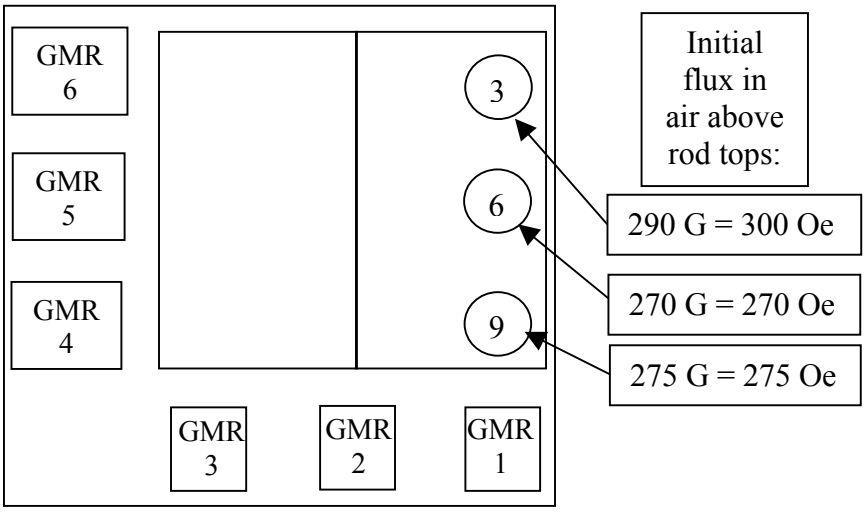

Figure 38. Initial flux density levels in air above rod tops of rods 3, 6, and 9.

Note that there is a difference in the flux density above rod 9 between figures 34 and 38. To clarify why rod 9 has a higher flux density value in the column configuration than in

the row configuration, Figure 39b depicts how in the row configuration, rod 9 had two return paths while in the column configuration (Figure 39a), rod 9 only had one return path.

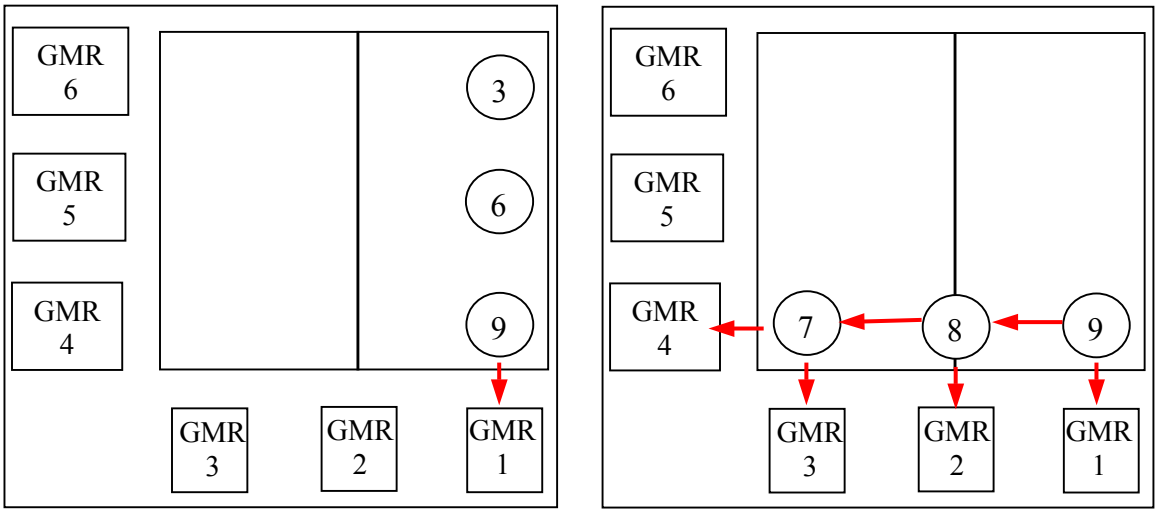

Figures 39 a and b. Flux return paths (in red) for the rods in a column and row configuration respectively.

Figures 40 a, b, and c, show the flux density change in the rods when one of the rods is stressed.

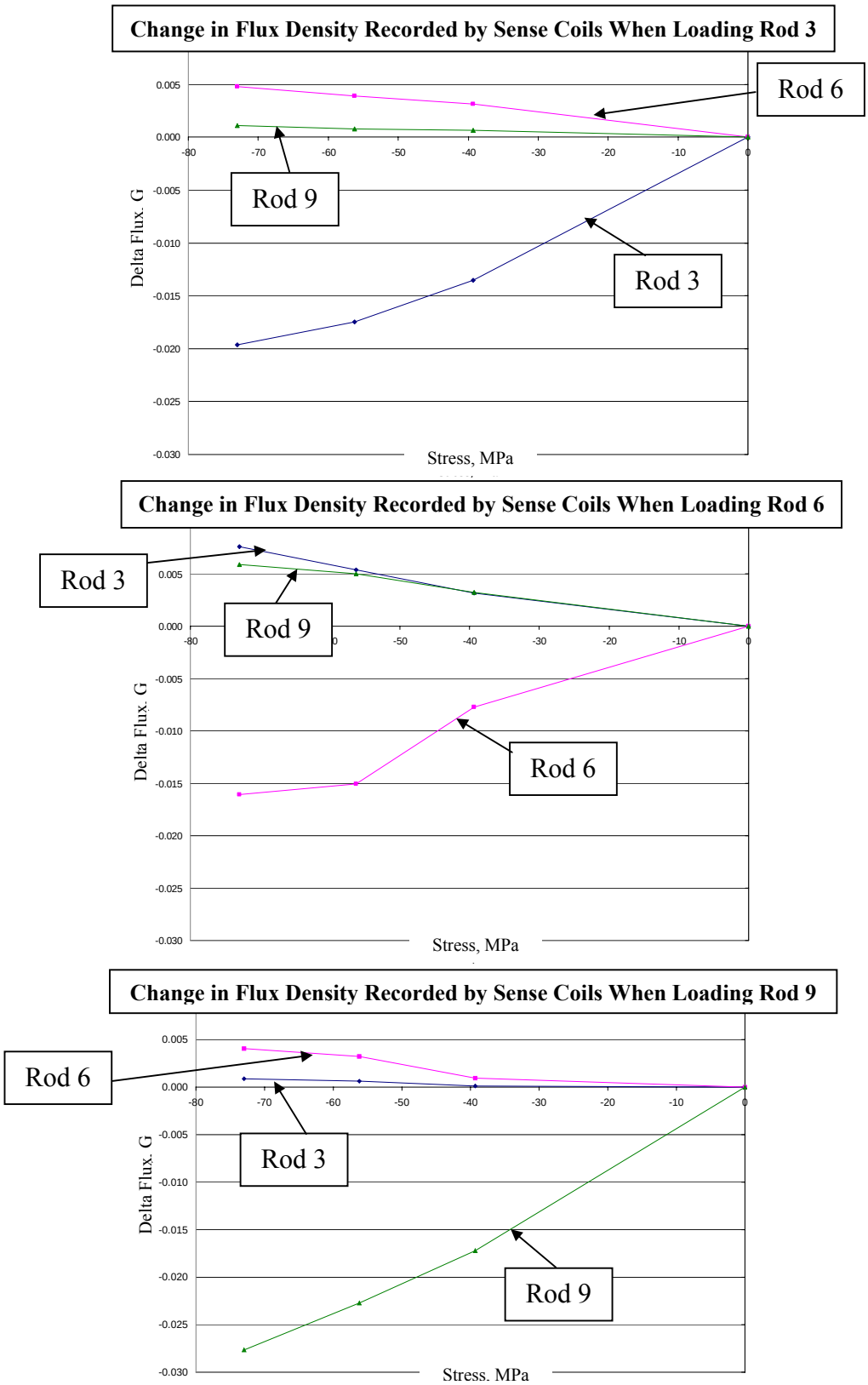

Figure 40: a, b, and c. Flux density change recorded by sense coils when loading rod 3, when loading rod 6, and when loading rod 9 respectively.

Figures 40 a, b, and c along with Figure 33, show that anytime a rod is stressed, its flux density will decrease while the other rods' flux density within the same column will increase. For example, when rod 3 is stressed (Figure 40a), the flux density within the rod decreases and the flux density in rods 6 and 9 increase. Rod 6 has a greater increase in flux density than does rod 9. This may indicate that when a rod that is the greatest distance, out of all rods, from the return path is stressed (in this case rod 3, Figure 39a), the flux changes from flowing through that rod (rod 3) to flowing through the rod that is the next closest to the flux return path (rod 6). When comparing results depicted in Figures 40 a and b, it is noted that the flux density in rod 6 does not change as much (~1500 G) as it did for rod 3 (~ 2000 G) when loaded to 73 MPa. Figure 40b also shows that rods 3 and 9 increase in flux density at about the same amount when rod 6 is loaded. When rod 9 is stressed (Figure 40c), its flux density decreases by the greatest amount out of the three rod loadings. Rods 3 and 6 only increase by small amounts (~75 G) during the loading of rod 9. This may indicate that the rod closest to the return path will provide the greatest change in flux density out of three with a single return path.

These two dimensional results are much more in line with the expected trend of the GMR closest to the rod under load provides the largest flux density change. The 3 dimensional case proved to be more complicated exhibited unexpected results. Also for the 2 dimensional case, data was not conclusive enough to indicate whether or not the initial flux density levels of rods in a circuit play a decisive role in the change in flux density during loading. It may be that the difference in initial flux density levels of this circuit was not great enough to show a difference during loading.

An interesting result that was shown in the above figures was that when the flux flow through a loaded rod was hampered by the decreasing permeability, the flux density increased through the next closest rod rather than the rod with the shorter return flux path length.

Figure 41 displays the data recorded by GMR sensor #1 as each rod in the column was individually loaded to 39.3, 56.2, and 73.0 MPa. As displayed in the figure, the largest change noted by GMR sensor #1 was when the rod closest to the side wall return path was stressed (rod 9). During loading, the change noted by the sensor decreased as proximity to the sensor (and to the return flux path) decreased. Also, while rods 3 and 6 increased in flux density by about the same amount over each increase in stress, rod 9 had a larger change in flux density over the same stress level increase.

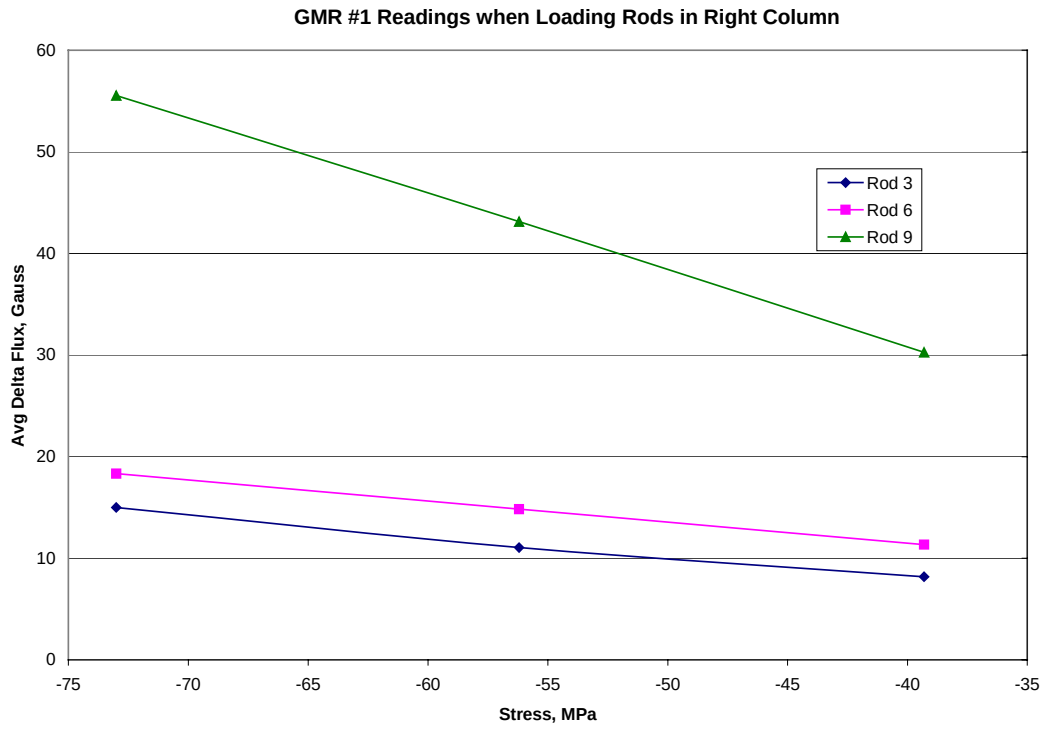

Figure 41. Average GMR #1 delta flux density data during loading of single column of rods 3, 6, and 9.

For both the bottom row of rods 7, 8, and 9, and the column of rods 3, 6, and 9, the data collected are compared to Figure 4 in Figure 42. The change in flux density is plotted with respect to the presumed value of bias field in the rods, based on the recorded values shown in Figures 35 and 38. (Due to instrumentation size constraints, a precise value for flux density in the unloaded rods could not be measured without disrupting flux return paths, which, as illustrated in Section 4.3, would have altered the targeted value.)

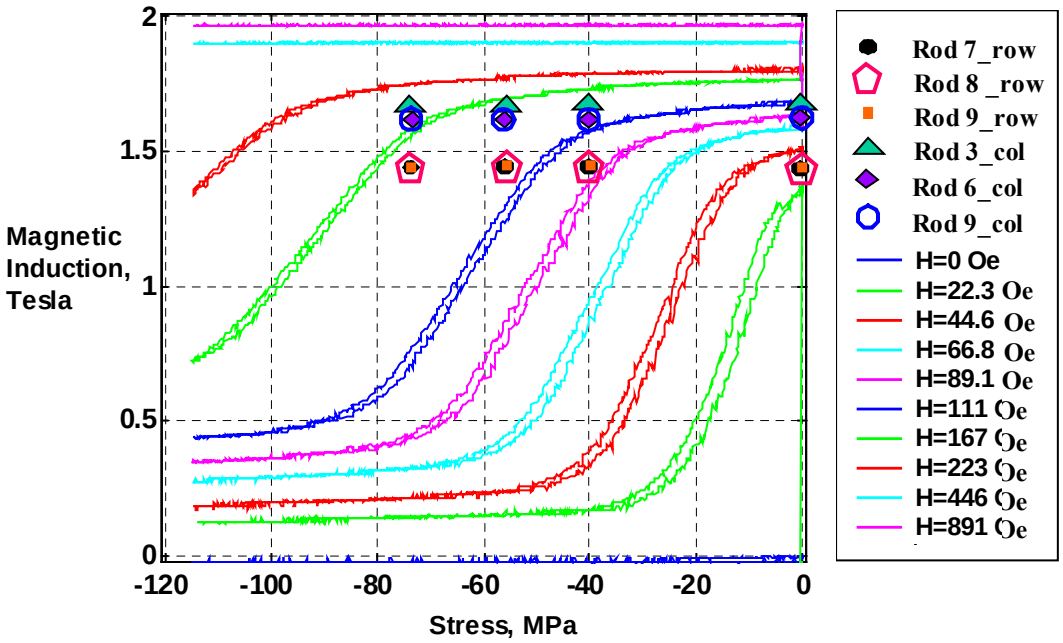

Figure 42. Comparison of experimental data collected by sense coils against given data for a polycrystalline rod. Experimental data (shaped points) is for a research grade rod while the given data is for a production grade rod (solid lines). (Magnetic induction versus stress curves courtesy of Atulasimha, 2006) "_row" denotes the single row array configuration and "_col" denotes the single column array configuration.

Although the trends observed in Figure 40 show magnetic induction decreasing with stress in the rod under load, when overlayed on the scale of Figure 42, magnetic induction values for rods 7, 8, and 9 in the row configuration essentially overlap each other, as do the magnetic induction values for rods 6 and 9 in the column configuration. The extremely small changes in magnetic induction shown in Figure 42 (on the scale of Figure 42) suggests that the rods were saturated, i.e. that the bias field was most likely greater than the 223 Oe bias field curve that is labeled, and that the stresses applied were insufficient to get much field change in the rods. Calculations were performed at this point to estimate the initial level of flux density in the rods.

5.3 Rod Flux Density Bias Level Investigation

The possibility that the Galfenol rods were biased to a field too high for the applied loads became apparent when testing of the second prototype was completed and the array measurement data was compared to the data collected by Atulasimha. Calculations were performed to estimate the initial level of flux density in the rods and are shown in equations 3, 4, and 5 and using the B-H curve for Galfenol in Figure 3.

Conservative assumption: Measured flux density parallel to rod axes just above rod tops is equal field at that point due to the measurement being taken through air. This field is assumed to be the same field as the steel rod top has and is used to find the flux density in the steel using the B-H curve for steel 1010 (Figure 43). (In actuality the field above the rod top is less than that within the steel and also the flux traveling parallel to the rod axes is less than that flowing along the steel paths perpendicular to the rod axes. Therefore the final solution for density in the rods will be lower than actual, and as noted this is a conservative approximation.

$$H_{steel} \Rightarrow B_{steel} \text{ (using Figure 43)}$$

$$flux_{steel} = B_{steel} * A_{steel} * \#paths \quad (3)$$

(A: Cross sectional area that flux travels through) (Figure 43 used to get field in steel) (Fitzgerald et al., 2003)

$$B_{rod} = flux_{steel}/A_{rod} \quad (4)$$

$$B_{rod} \Rightarrow H_{rod} \quad (5)$$

(Using B-H curve in Figure 3)

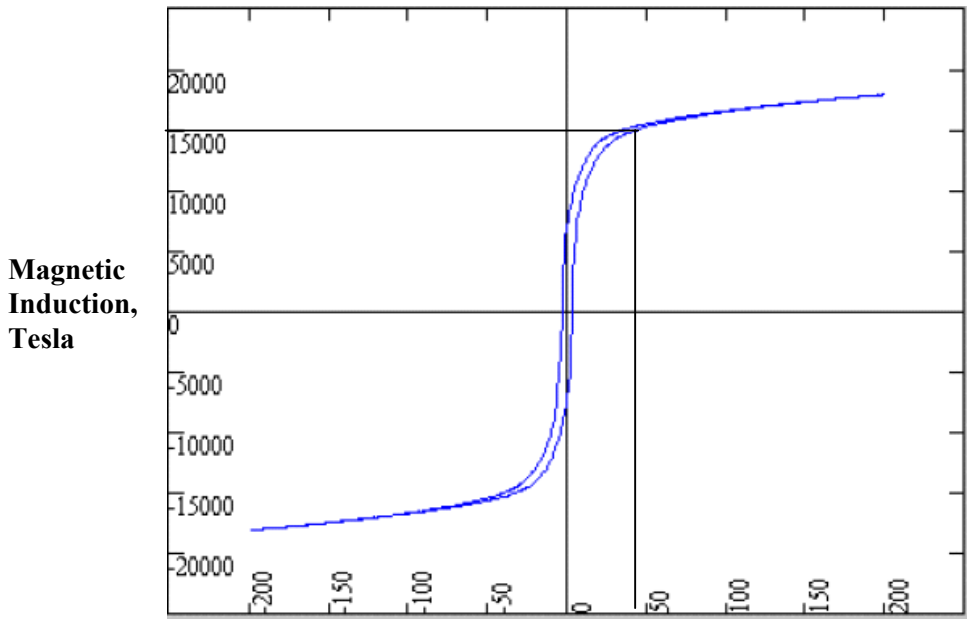

Figure 43. B-H curve for Steel 1010 (Walker LDJ Scientific, Inc.)

Sample calculation: Rod with H = ~ 40 Oe => B_{steel} = 1.5 T (using Figure 43)

H_{steel} = 1.5 Tesla * (1.59*3.175)mm^2 * 2

= 15.12 Tesla * mm^2

$B_{rod} = H_{steel} / A_{rod}$

$= 15.12 / (\pi * (3.18/2)^2)$

B_{rod} = 1.9 Tesla

B_{rod} => H_{rod} => greater than 200 Oe (i.e. out of range of Figure 3)

This shows that the rods are indeed subjected to a magnetic bias of greater than what a 200 Oe applied field would produce. Therefore, although the magnetic 2-D and 3-D models suggested the fields in air above the rod-tops seemed appropriate for the targeted load levels, the permanent magnet used must have been stronger than was originally modeled. Figure 44 locates the area on Figure 42 at which the data for such a high magnetic bias should appear.

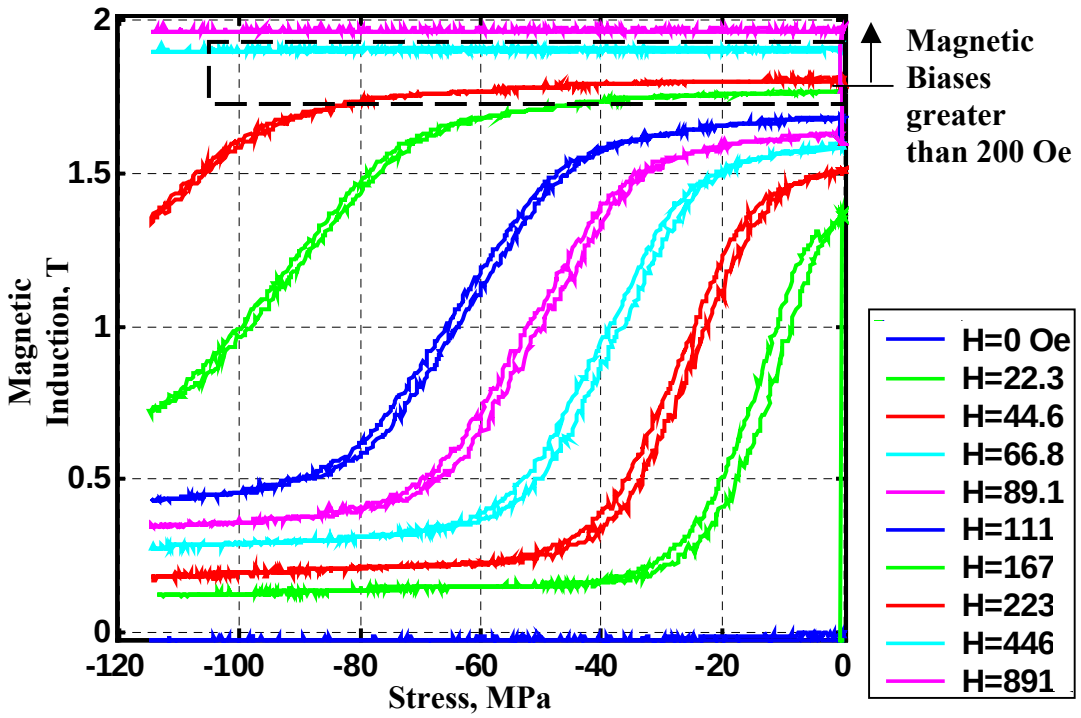

Figure 44. Depiction of where data for the rods in the Galfenol magnetic circuit array should fall with magnetic biases greater than 200 Oe.

As shown in Figure 44's legend, the third lie from the top is for a magnetic bias of 223 Oe. Therefore, according to the calculations in section 5.3, the data for the Galfenol rods in the magnetic circuit array could start anywhere from just below this line to anywhere above it. Figure 45 zooms in on the section of Figure 44 enclosed by the dashed black rectangle. The flux density changes for the row of rods 7, 8, and 9 are not depicted as the data is not distinguishable from the column data. Flux density changes for rods 3, 6 and 9 are too small to show change on the scale used in Figure 45 (scale was chosen in order to allow comparison of the data to that given in Figure 44). Therefore, it was determined that the data's initial magnetic bias was greater than 223 Oe.

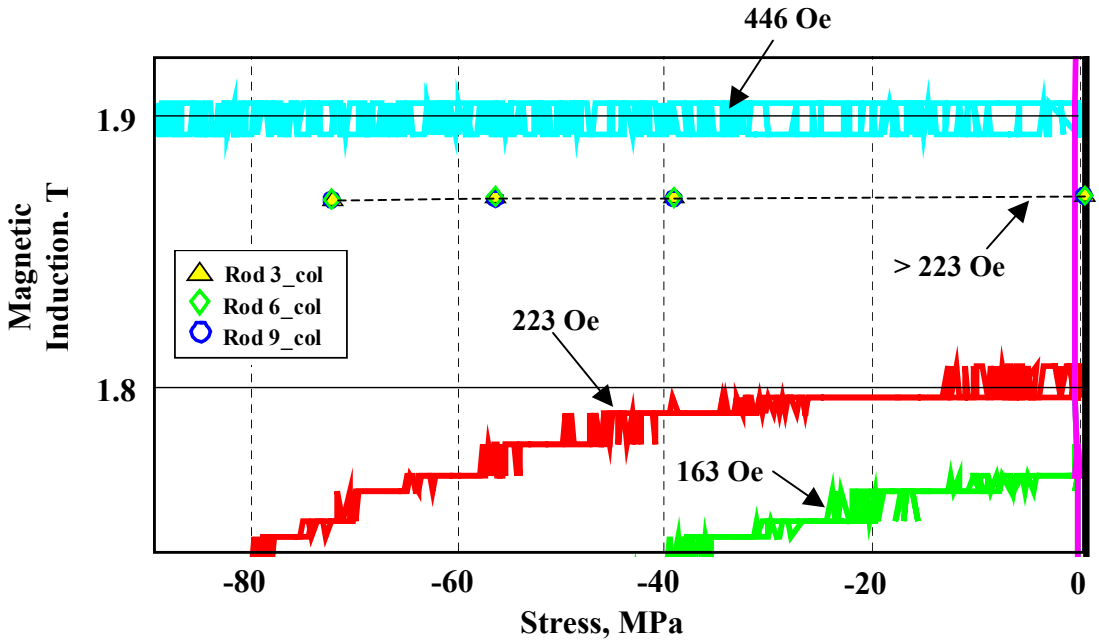

Figure 45. Zoomed in section of Figure 42 showing trend of flux density changes for rods 3, 6, and 9 in the column configuration. Data has an initial magnetic bias greater than 223 Oe.

6 CONCLUSIONS AND SUMMARY

Magnetic modeling and two prototype sensor arrays were built and tested to provide insight into the feasibility of the Galfenol sensor array concept. Initial magnetic modeling provided knowledge on the sensor array design in terms of the magnetic bias required, symmetric versus asymmetric flux path design, location of the GMRs, and expected data collection results. In addition to the two 3 x 3 circuit arrays built, two simplified circuits of 3 rods each; one in the column configuration and one in a row configuration were tested and analyzed.

Results from the magnetic modeling concluded that the asymmetric return path configuration was ideal for using the measurement of change in magnetic density to determine the location of a loaded rod. The models also determined the best location to place the sensors and the strength of the permanent magnet used to provide the magnetic bias in the Galfenol rods.

The first prototype's tests were conducted with rods individually loaded at stress levels of 4 and 7 MPa. Rods were loaded statically and dynamically and the resulting GMR sensor responses were analyzed. Although the GMRs had small responses to these loads, results lead to identification of a major design problem, the introduction of air gap between rod tops under load, which overwhelmed the targeted responses. FEM modeling confirmed the need for a redesign that would not cause air gaps under load. Also, the testing provided insight on the fabrication and assembly issues involved with the array design.

Tests of the second prototype array entailed loading individual rods to stress levels of 40, 56, 67, and 73 MPa within the 3 x 3 sensor array. Improvements to the second prototype included tightening the fabrication tolerances within the circuit, inserting magnetic grease between rod tops, and attaching strain gages and sense coils to the rods to increase data collection capability. The strain gages and sense coils enabled the collection of strain and flux density data on individual rods. The resulting data provided information on the change in flux density, strain, and GMR readings when loading the rods.

Tests were also performed on a single row and also a single column of rods in order to characterize magnetic induction change under stress within simplified circuits. As shown in figure 40 a, b, and c, the 3-rod circuit showed promising correlation between the loaded rod and its change in magnetic induction. These figures also give insight into how the flux density of the rods that were not being stressed changed. It can be said with certainty that the rod stressed will decrease in permeability and therefore the flux flow through it will decrease. How this flux density change in one rod affects the others seems to depend on the location of the stressed rod within the circuit. If the stressed rod is on either end of the row or column, the center rod's flux density will increase more than the rod on the opposite end.

As made apparent in Figure 42, the magnetic induction data of the bottom row and the right column (colored shapes) did not noticeably decrease (on the scale of Figure 42) when compared to the expected behavior shown for the polycrystalline, production grade

rod (solid lines). This data suggested error in the initial flux density values within the Galfenol rods. Although these values could not be directly measured, in Section 5.3 gaussmeter data from the magnetic fields in air above the rods was used to provide an estimate of a minimum possible flux density in the rods. This estimate indicated that the value exceeded the targeted range of being equivalent to what a 20-100 Oe field would produce and that the permanent magnet used was stronger than that modeled. Due to the stronger magnet, the bias field within the Galfenol rods was higher than the particular load range had capability to rotate the domains. The stresses applied to the rods during loading were not able to overcome this bias only slightly rotated the magnetic moments within the Galfenol rods. Figures 44 and 45 determined the area that the data should fall within and then zoomed in on the area to show the magnetic induction changes for rods 3, 6, and 9 in the column configuration. The data did not show any decrease in flux density at this scale and so it was determined that the initial magnetic biases for the rods were greater than 223 Oe.

According to the modeling performed, the concept of using Galfenol in an asymmetric grid array to determine force location is possible. Promising experimental results show definite correlation between the loaded rod and the change in flux density as observed in the 3x1 sensor configurations (Figures 40 a, b, c). Overall, these tests have produced some successes and identified areas that need modification and further study. By reducing initial rod biases to within that required for these loads and by preventing rod top separation the flux density data collected will be more accurate. With the data collected here, and the future work planned, the researchers in this experiment believe

Galfenol sensor arrays are feasible and could produce great advances in sensor technology.

7 SUGGESTED FURTHER STUDY

Replace permanent magnet

The most important change to this experiment is to exchange the permanent magnet with a magnet of a desirable strength that will provide a magnetic field within the Galfenol rods within the ideal range indicated by Figure 4 (20 to 100 Oersteds). Measurements should be made of the rod's initial flux density when assembled in the circuit array to ensure the proper bias before experimentation.

Modeling

Magnetic modeling proved difficult for Galfenol stress levels higher than 15 MPa as Galfenol's B-H curves have a S-shape which caused the modeling program to diverge when attempting to converge on an answer. Even after modifying the B-H curve by removing the initial part of the curve at low field levels, problems still occurred. Further modifications to the B-H curve may be made and/or changes to the model should be performed to enable modeling results at higher stress levels.

Further modeling of the single row of rods should be performed to determine if the experimental results match what is predicted. The modeling should investigate the change in flux density in each rod in a single row or column of rods when stress levels of 39.3, 56.2, and 73.0 MPa are applied to each row. Two rows/columns should be analyzed. One should have only one return path at one end of the row (Figure 46a), while the second analysis should have a row with 4 return paths as shown in Figure 46b.

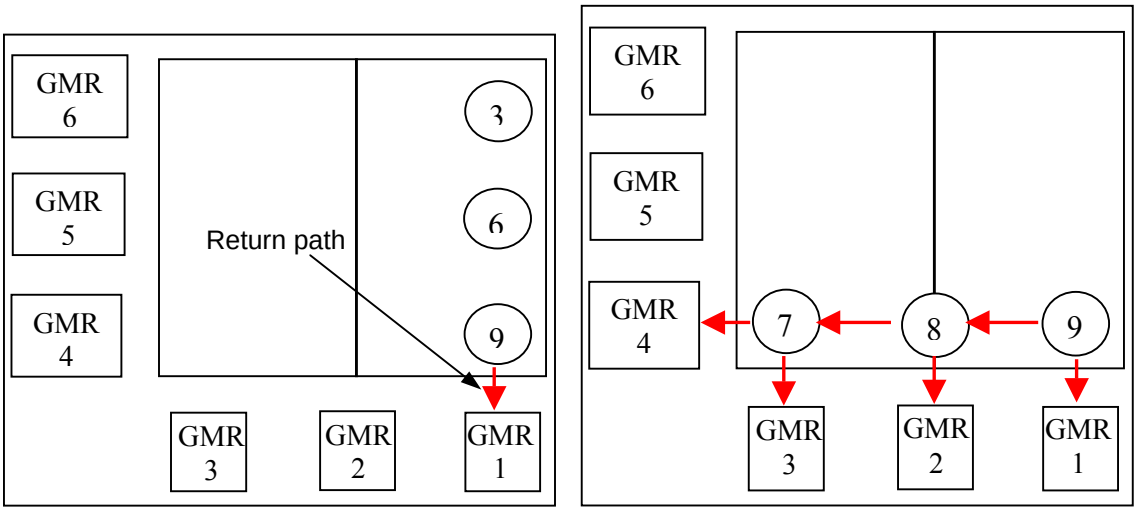

Figures 46 a. Modeling configurations with single return path
b. Modeling configurations with four return paths.

Size and proximity of GMR sensors

The GMR sensors used in the magnetic circuit have widths close to that of the steel pathways on the sides of the circuit where they are attached. Due to the fact that the sensors and pathways were located about 1/16″ from one another, questions arise as to whether or not the magnetic field one sensor is detecting is affected by the path next to it. A possible improvement would be to recess the GMR sensor into the steel path so that the flux flow goes directly through it, rather than the sensor being located over the flux flow. This may decrease the amount of proximity effect between the sensors and increase the sensor's accuracy in recording flux density change.

The size of the GMR sensor also raises issues when considering the intention to scale the circuit and create a nano-sized system. A GMR "violin" sensor exists that might be able to be incorporated to allow measurements to occur with the larger parts a certain distance away from the magnetic field pathway. This would allow magnetic field pathways to be

located closer together and would allow space for more of the pathways, therefore increasing resolution.

Congruity of flux paths

The steel paths on the tops of the rods are fabricated as separate pieces to allow force to be applied to one rod without applying force to another. Decreasing spacing tolerance and inserting magnetic grease (grease with iron filings) between the flux path tops may not have been enough to prevent gaping. Another solution is to use a single, flexible, magnetic piece of material in place of the steel rod top pieces. Thought should be put into the fact that the single piece of material may not enable loading of a single rod without affecting other rods. Additionally, holes should be paced within the material in order to create distinct flux paths.

APPENDIX

Static and dynamic loading of rods in 3x3 array; GMRs are positioned as shown in figure below:

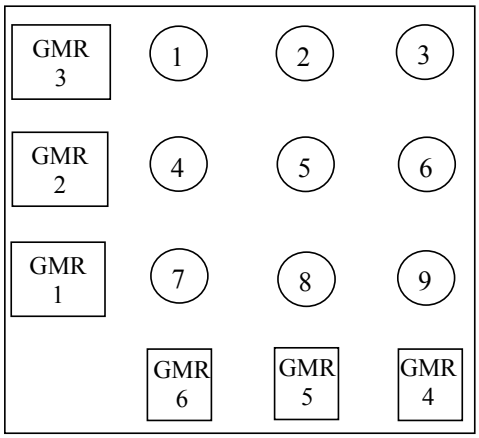

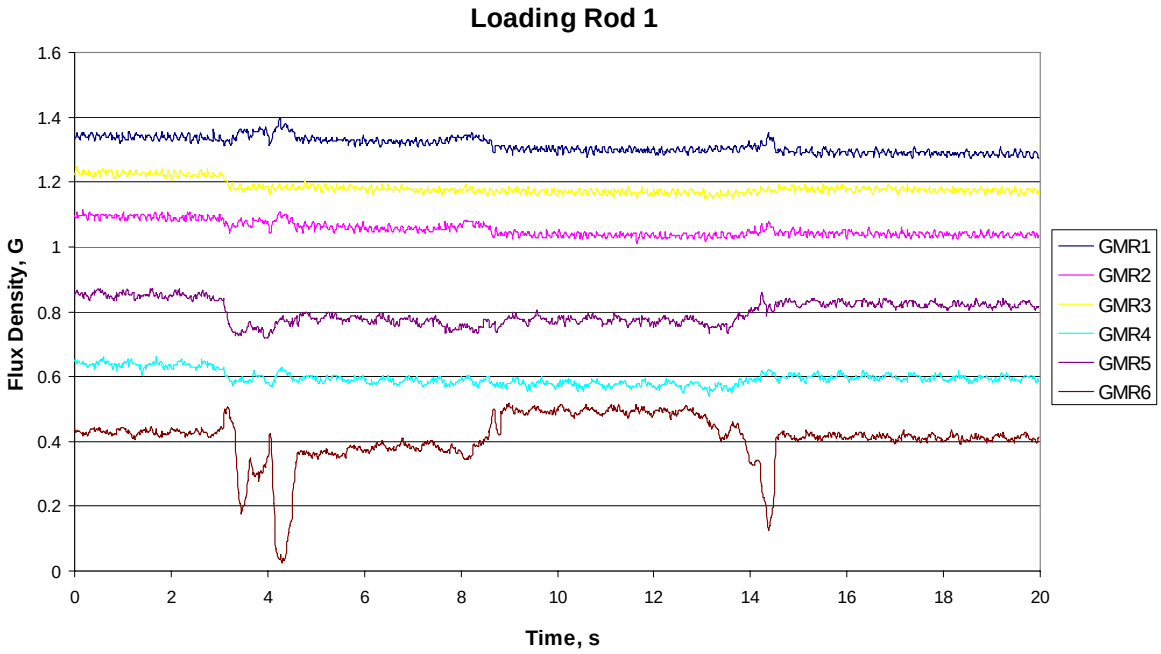

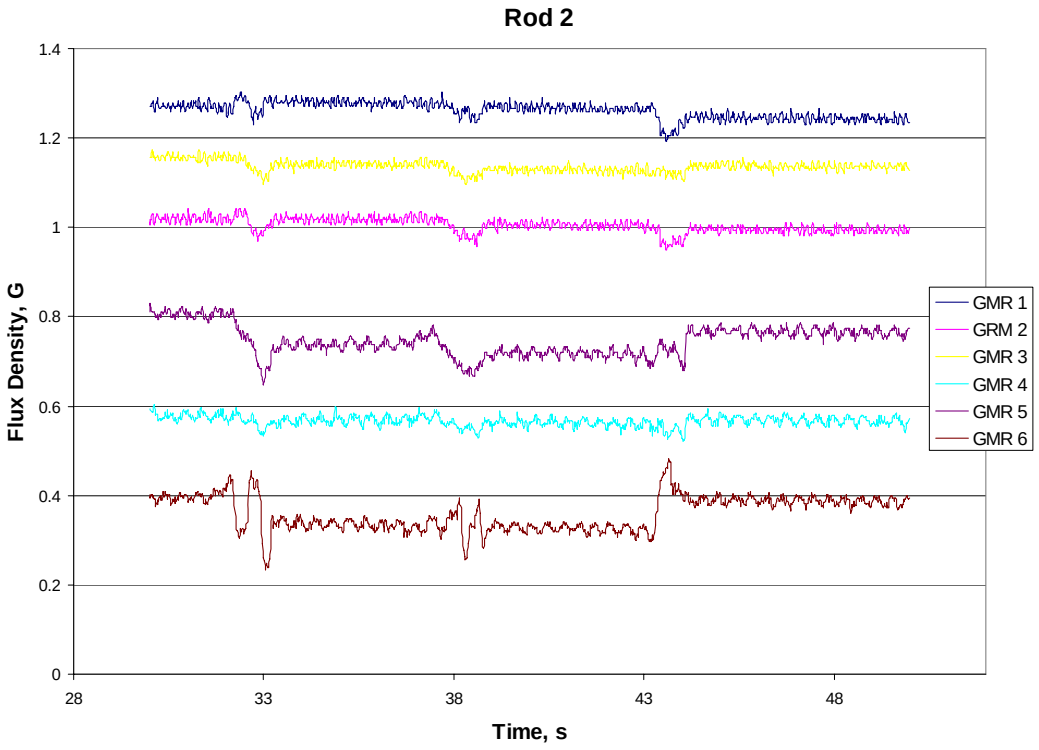
Rod 2
Flux Density, G
Time, s
1.4
1.2
1
0.8
0.6
0.4
0.2
0
28
33
38
43
48
GMR 1
GRM 2
GMR 3
GMR 4
GMR 5
GMR 6

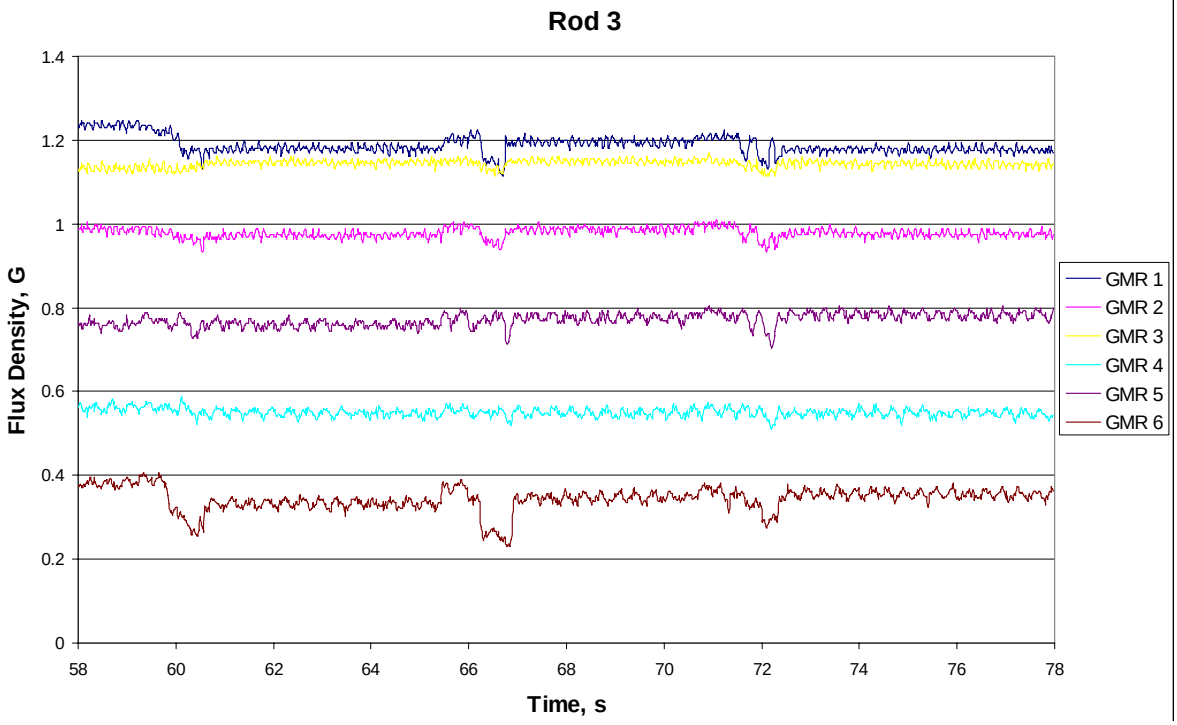
Rod 3
Flux Density, G
Time, s
1.4
1.2
1
0.8
0.6
0.4
0.2
0
58
60
62
64
66
68
70
72
74
76
78
GMR 1
GMR 2
GMR 3
GMR 4
GMR 5
GMR 6

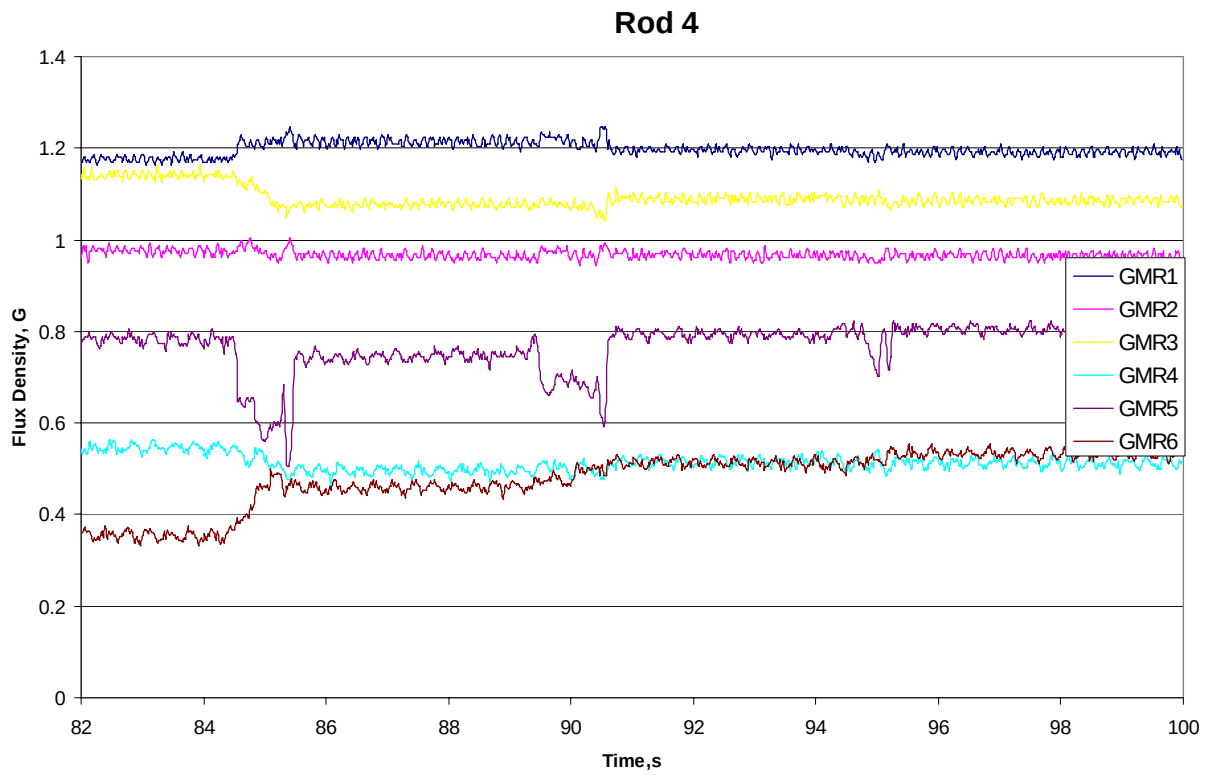
Rod 4
Flux Density, G
Time,s
GMR1
GMR2
GMR3
GMR4
GMR5
GMR6

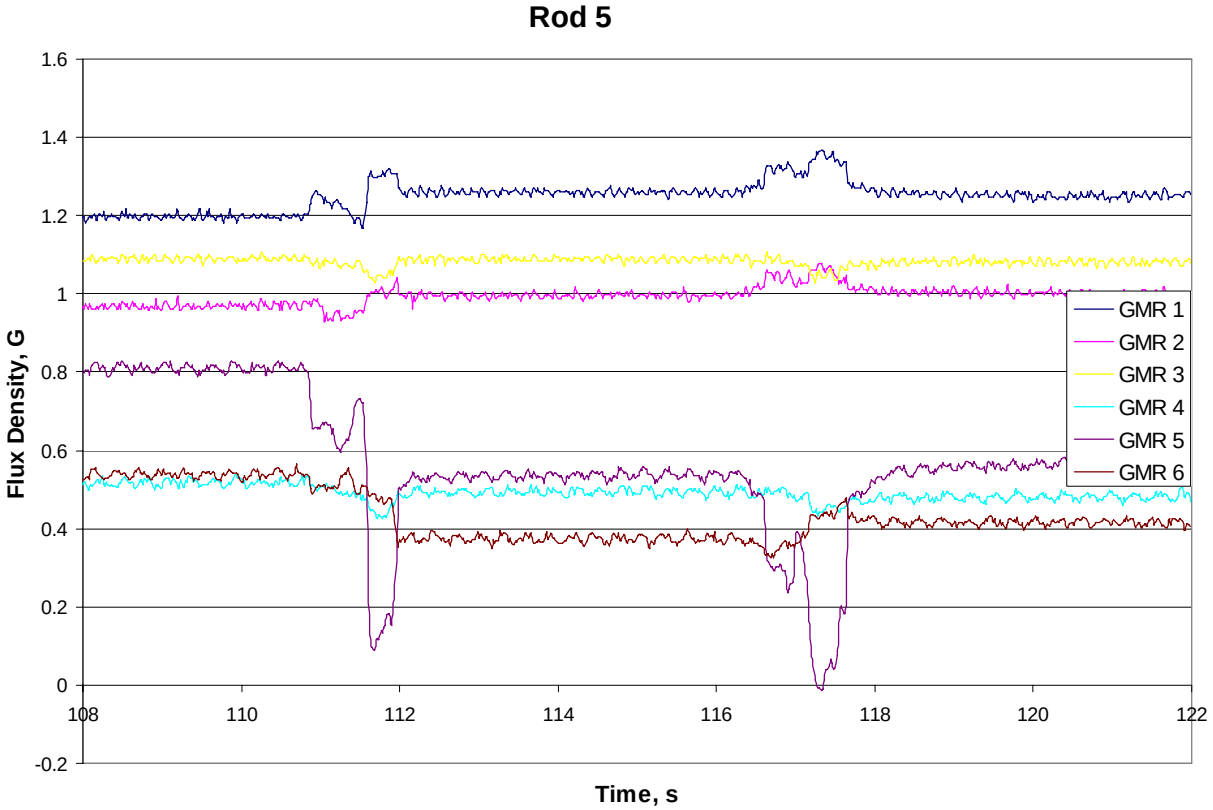
Rod 5
Flux Density, G
Time, s
GMR 1
GMR 2
GMR 3
GMR 4
GMR 5
GMR 6

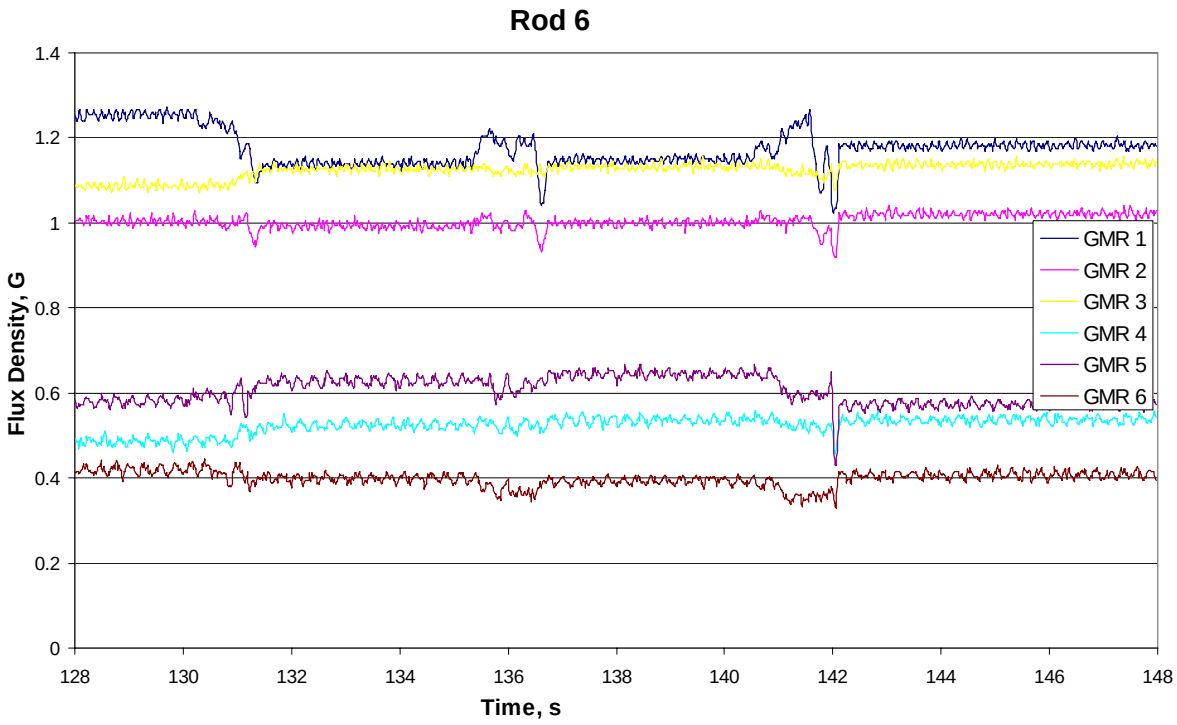
Rod 6
Flux Density, G
Time, s
GMR 1
GMR 2
GMR 3
GMR 4
GMR 5
GMR 6
0
0.2
0.4
0.6
0.8
1
1.2
1.4
128
130
132
134
136
138
140
142
144
146
148

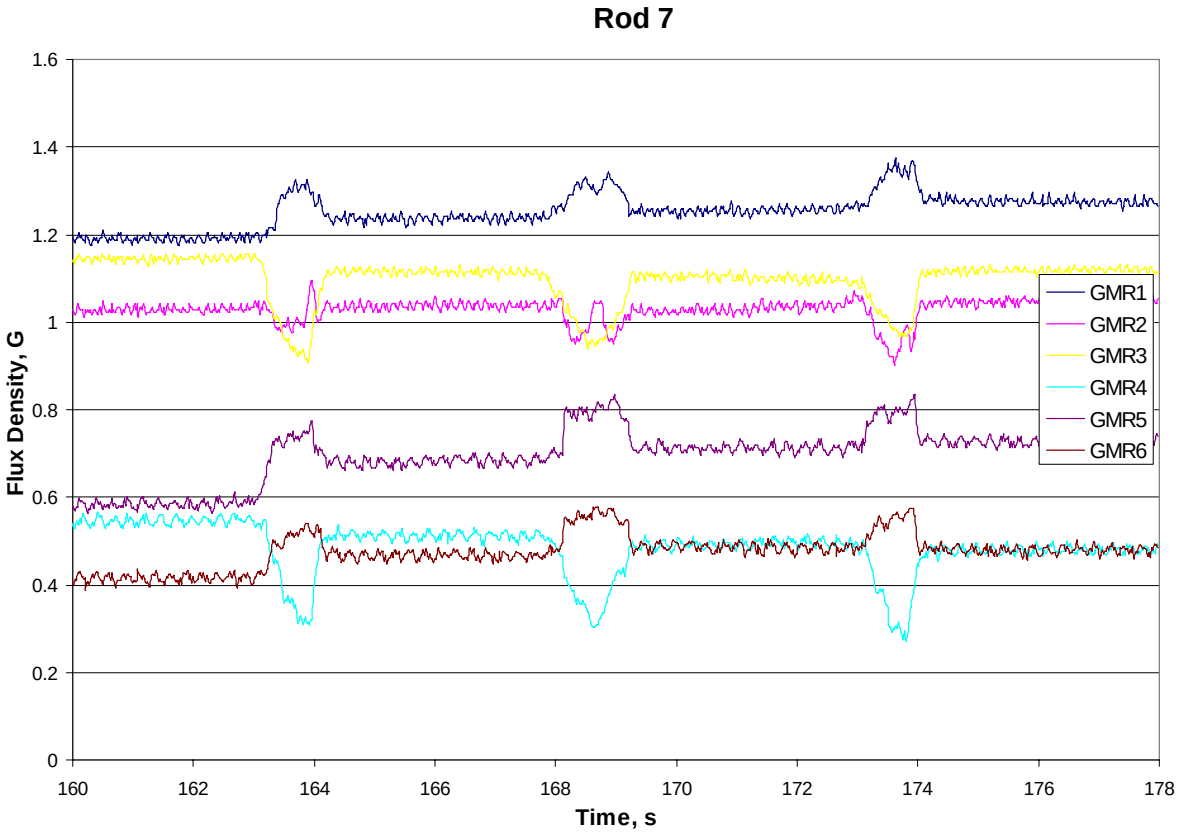
Rod 7
Flux Density, G
Time, s
GMR1
GMR2
GMR3
GMR4
GMR5
GMR6
0
0.2
0.4
0.6
0.8
1
1.2
1.4
1.6
160
162
164
166
168
170
172
174
176
178

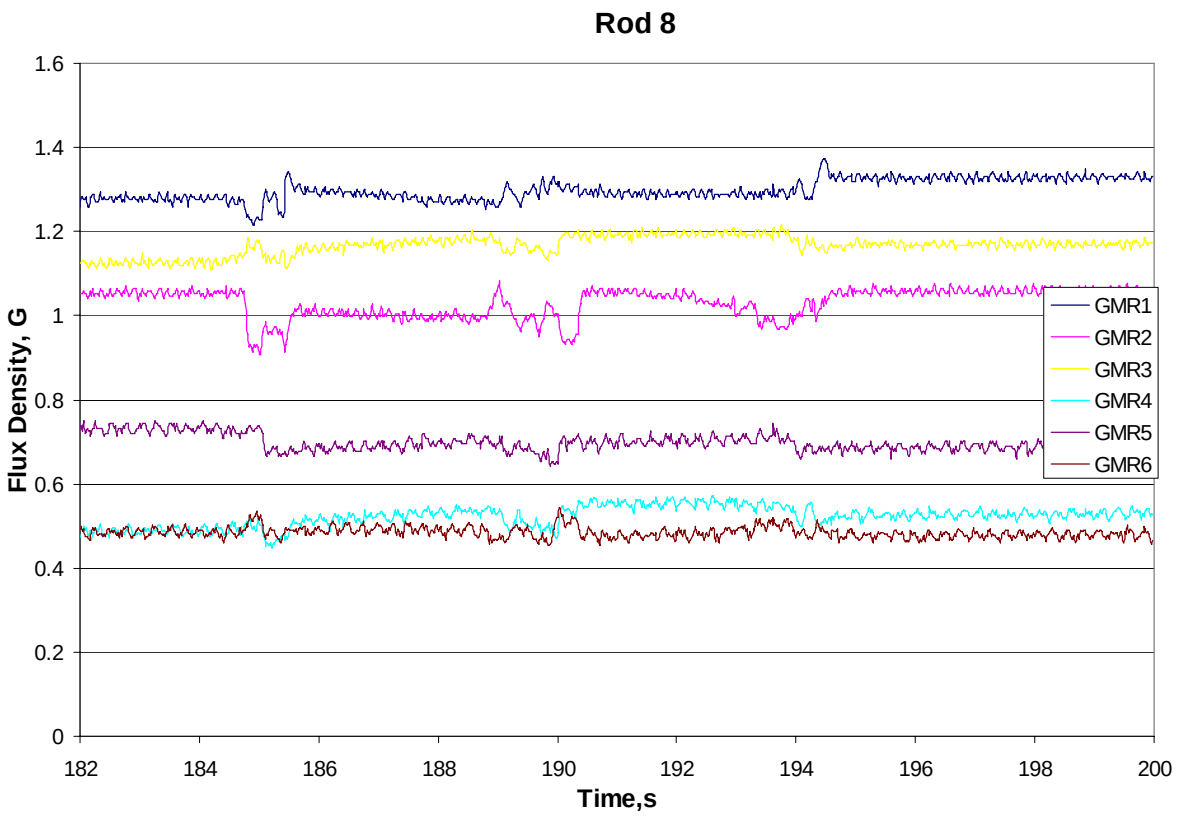
Rod 8
Flux Density, G
Time,s
GMR1
GMR2
GMR3
GMR4
GMR5
GMR6

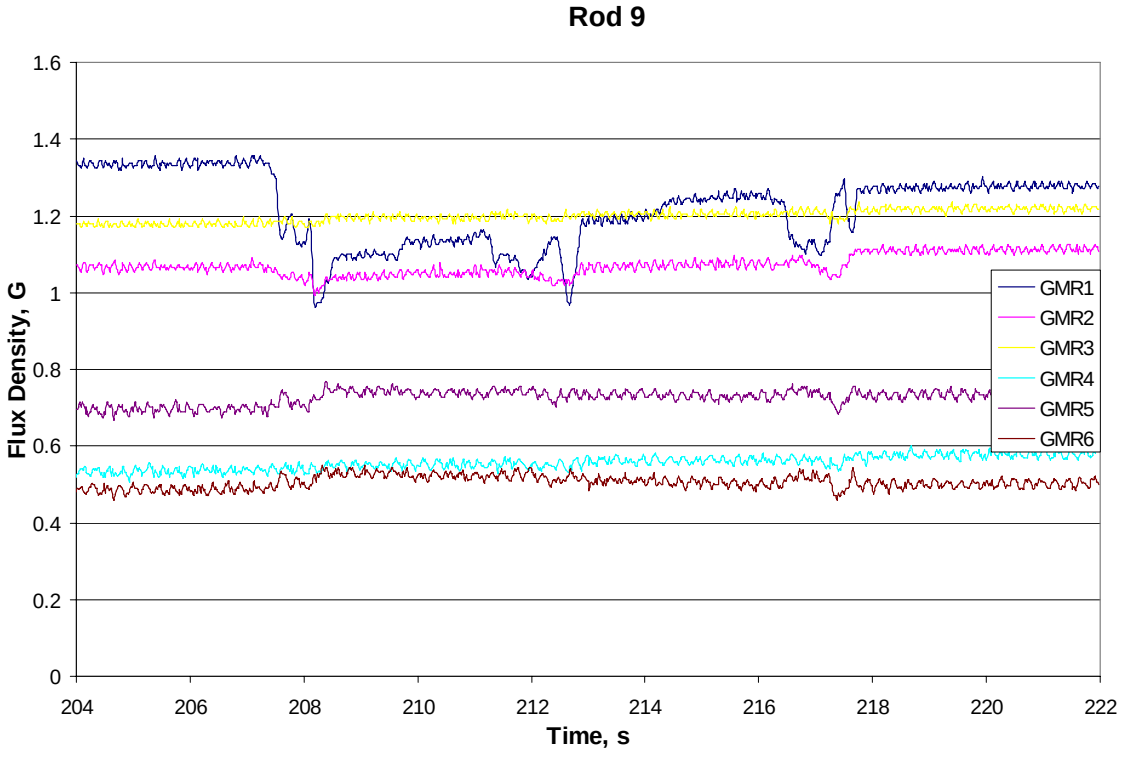
Rod 9
Flux Density, G
Time, s
GMR1
GMR2
GMR3
GMR4
GMR5
GMR6

Dynamic Loading

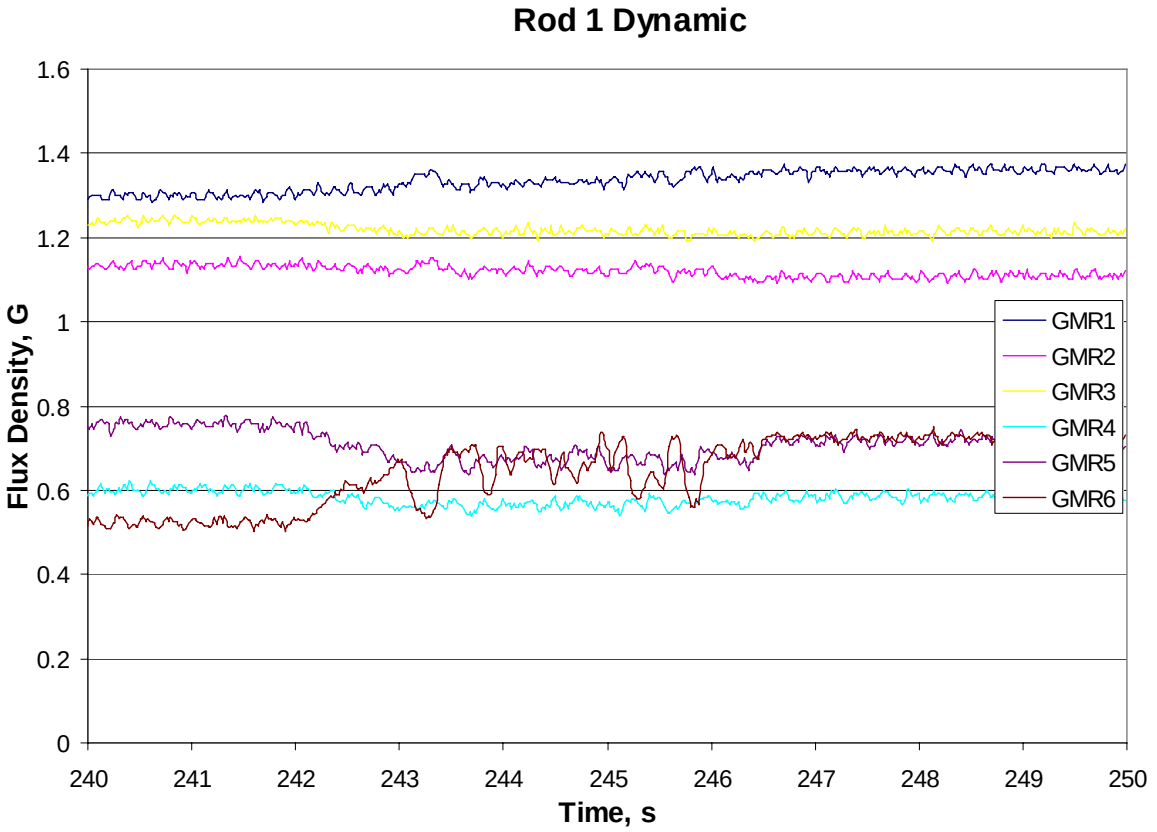

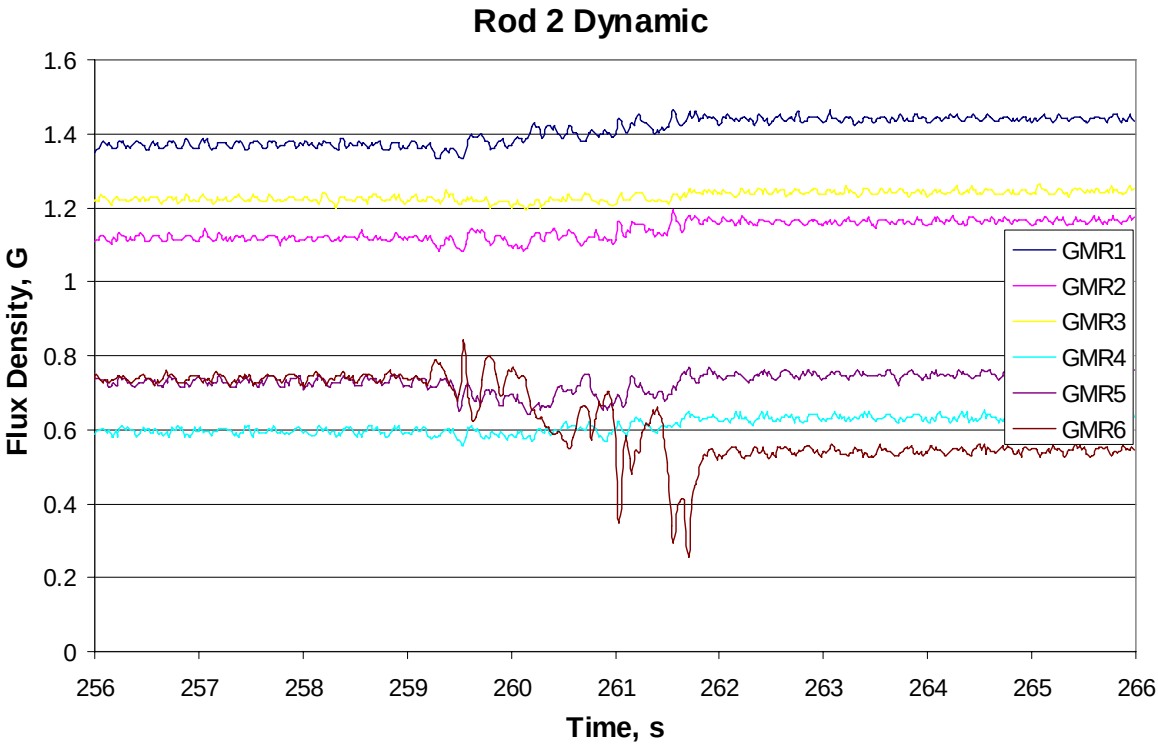

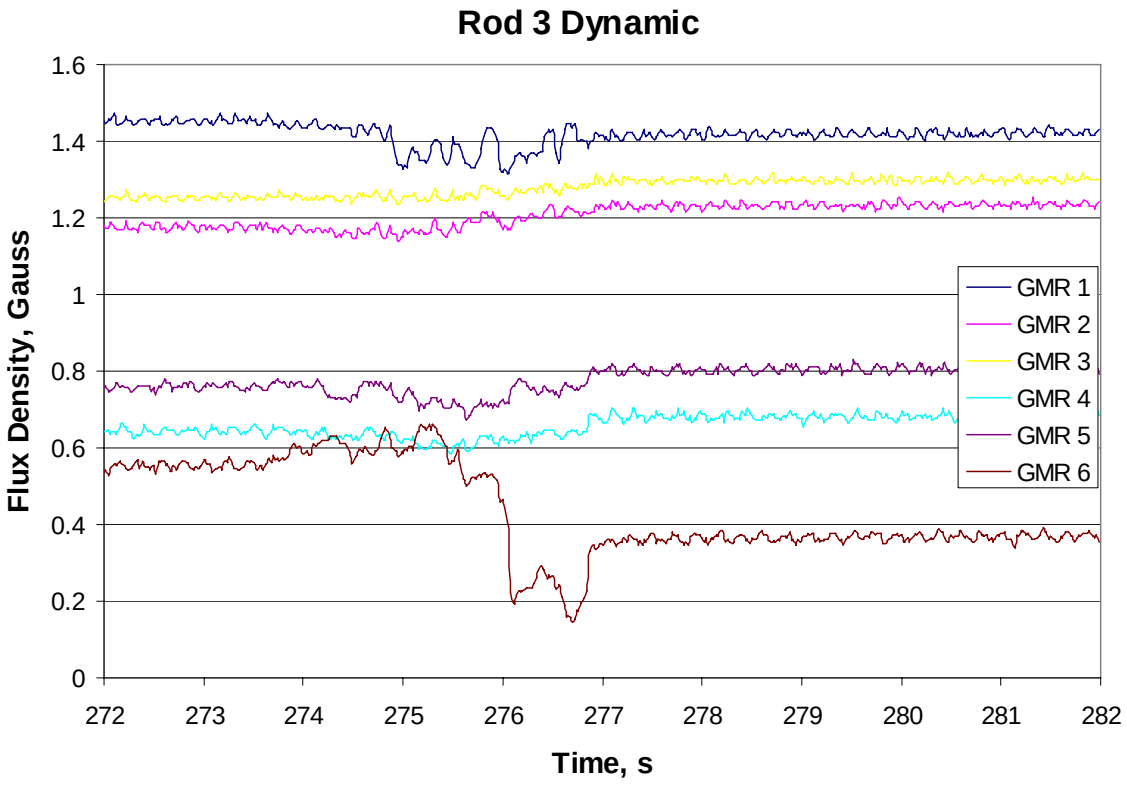
Rod 3 Dynamic
Flux Density, Gauss
Time, s
GMR 1
GMR 2
GMR 3
GMR 4
GMR 5
GMR 6
0
0.2
0.4
0.6
0.8
1
1.2
1.4
1.6
272
273
274
275
276
277
278
279
280
281
282

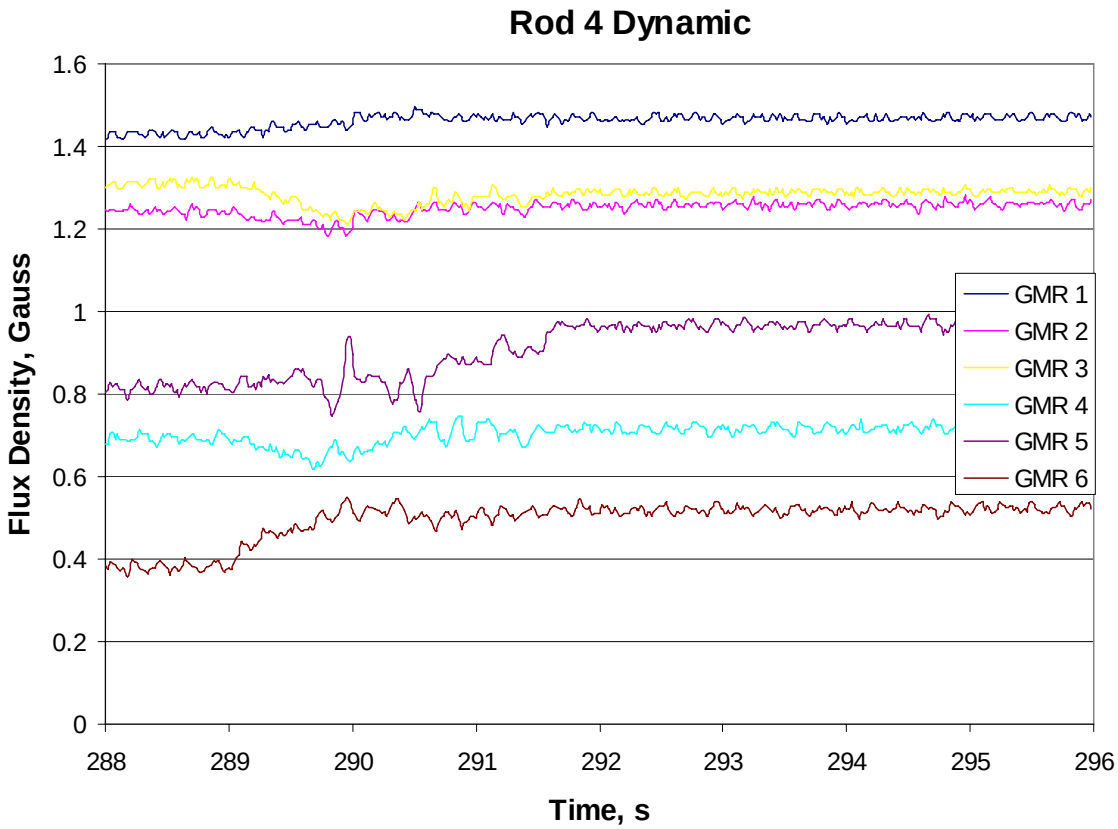
Rod 4 Dynamic
Flux Density, Gauss
Time, s
GMR 1
GMR 2
GMR 3
GMR 4
GMR 5
GMR 6
0
0.2
0.4
0.6
0.8
1
1.2
1.4
1.6
288
289
290
291
292
293
294
295
296

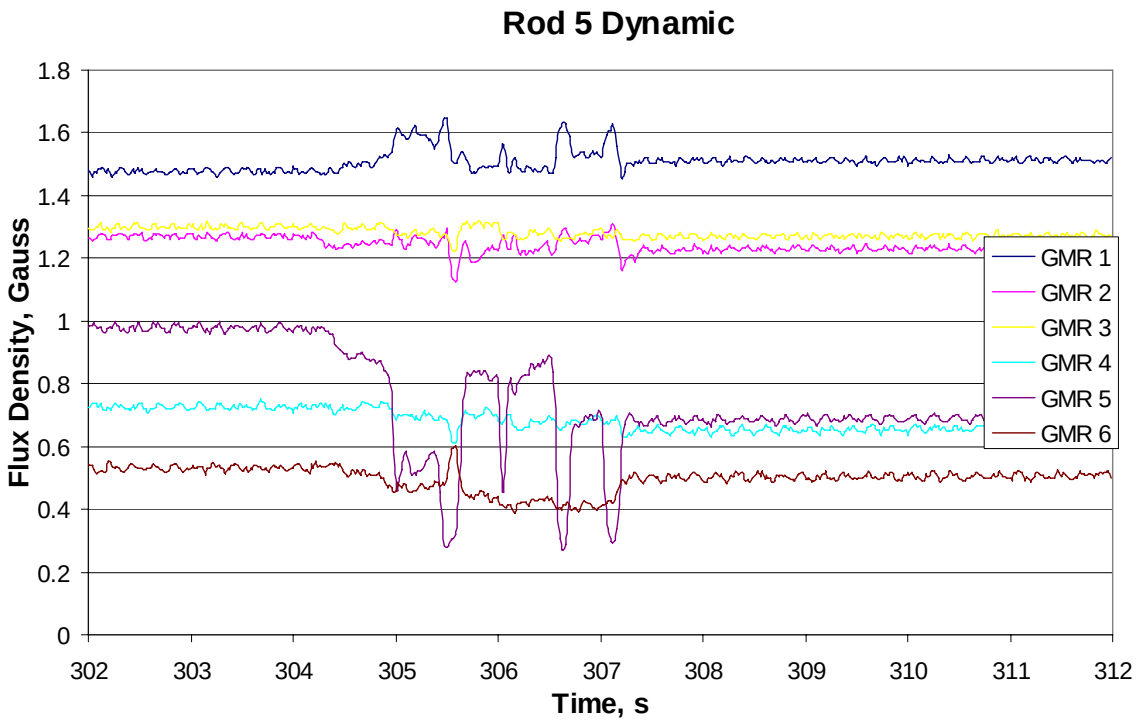
Rod 5 Dynamic
Flux Density, Gauss
Time, s
GMR 1
GMR 2
GMR 3
GMR 4
GMR 5
GMR 6
0
0.2
0.4
0.6
0.8
1
1.2
1.4
1.6
1.8
302
303
304
305
306
307
308
309
310
311
312

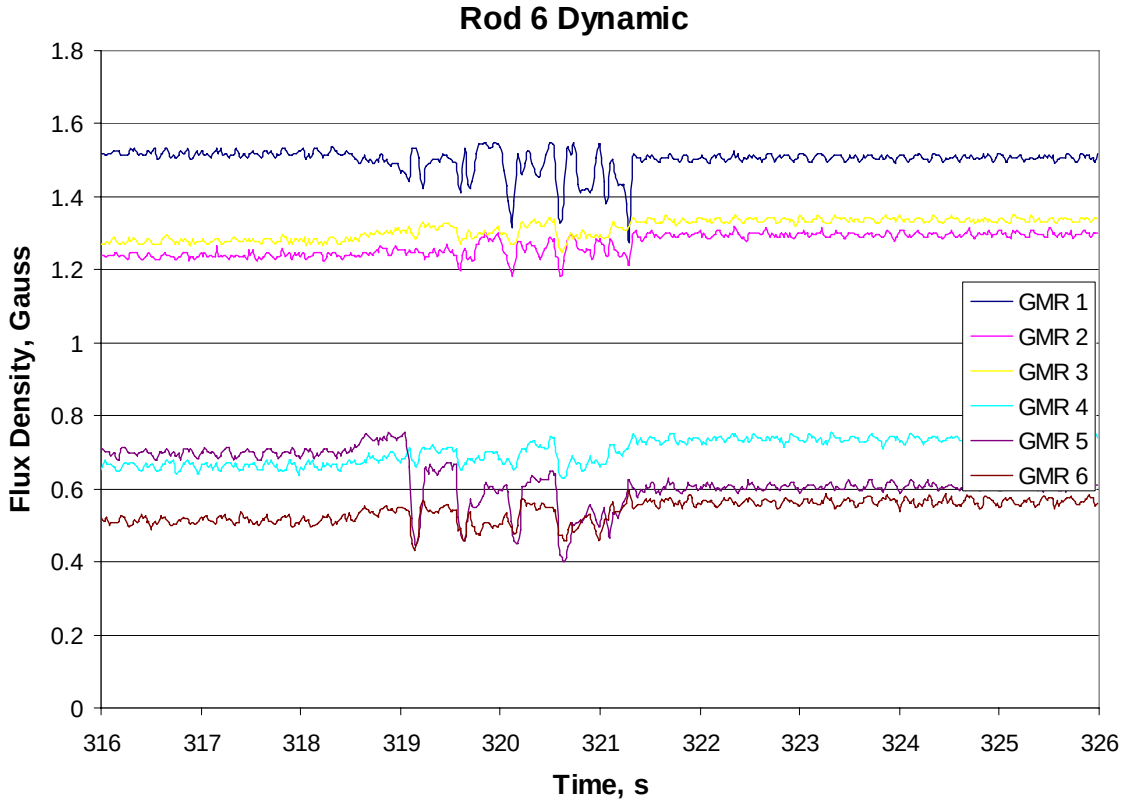
Rod 6 Dynamic
Flux Density, Gauss
Time, s
GMR 1
GMR 2
GMR 3
GMR 4
GMR 5
GMR 6
0
0.2
0.4
0.6
0.8
1
1.2
1.4
1.6
1.8
316
317
318
319
320
321
322
323
324
325
326

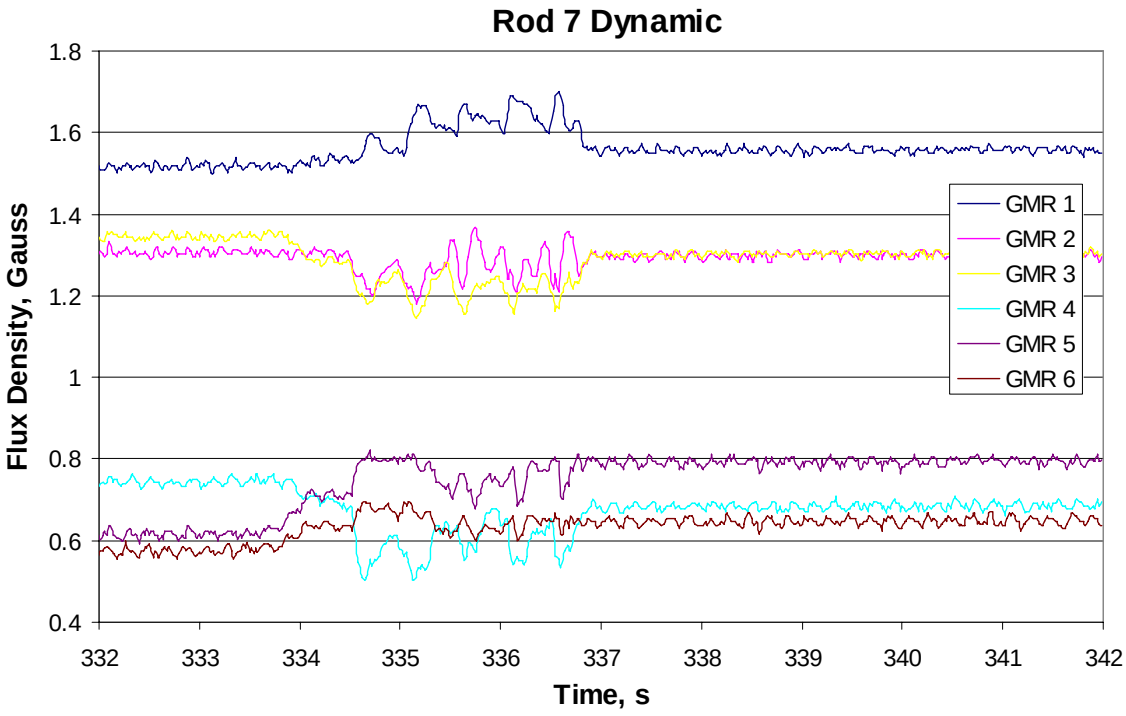
Rod 7 Dynamic
Flux Density, Gauss
Time, s
GMR 1
GMR 2
GMR 3
GMR 4
GMR 5
GMR 6
1.8
1.6
1.4
1.2
1
0.8
0.6
0.4
332
333
334
335
336
337
338
339
340
341
342

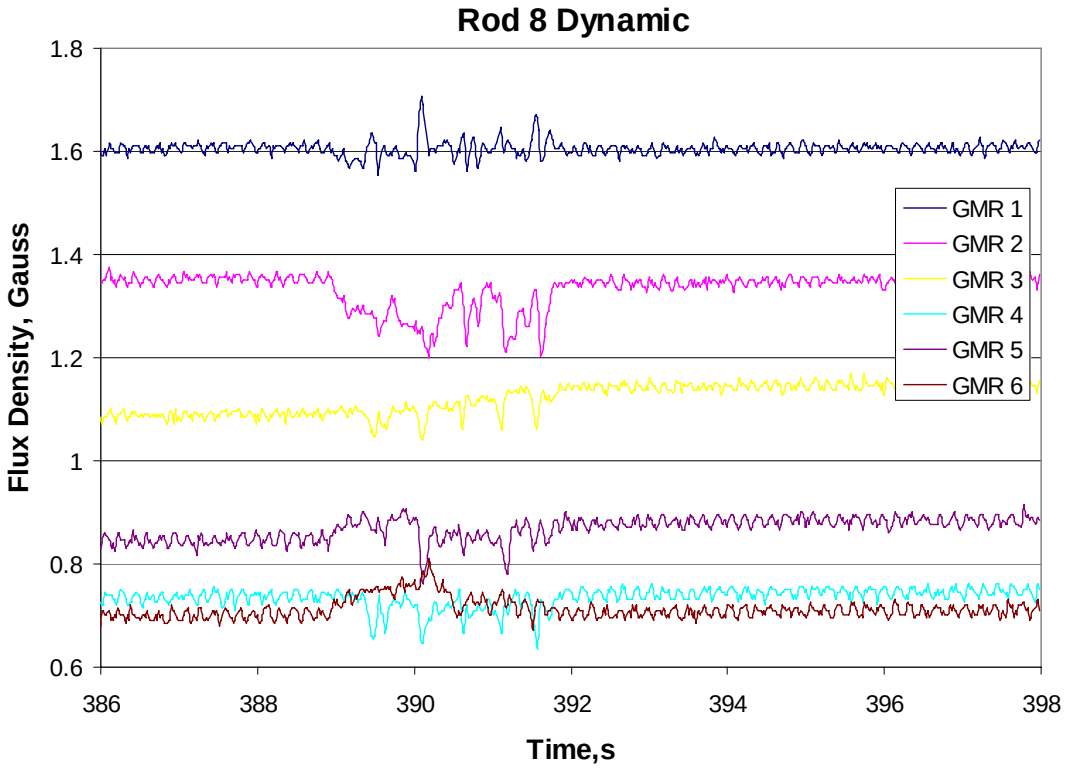
Rod 8 Dynamic
Flux Density, Gauss
Time,s
GMR 1
GMR 2
GMR 3
GMR 4
GMR 5
GMR 6
1.8
1.6
1.4
1.2
1
0.8
0.6
386
388
390
392
394
396
398

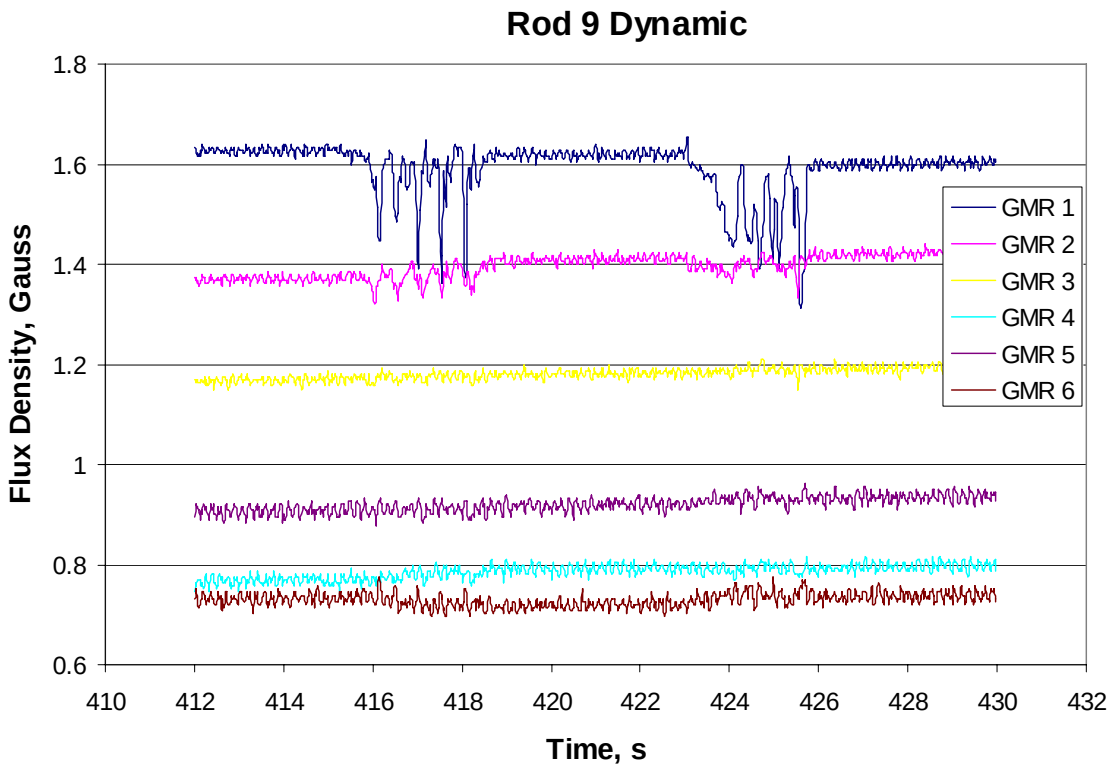

Diagonal rods in full 3 x 3 configuration:

Data recorded for loading performed by hand on rods 3, 5, and 7 in the following configuration:

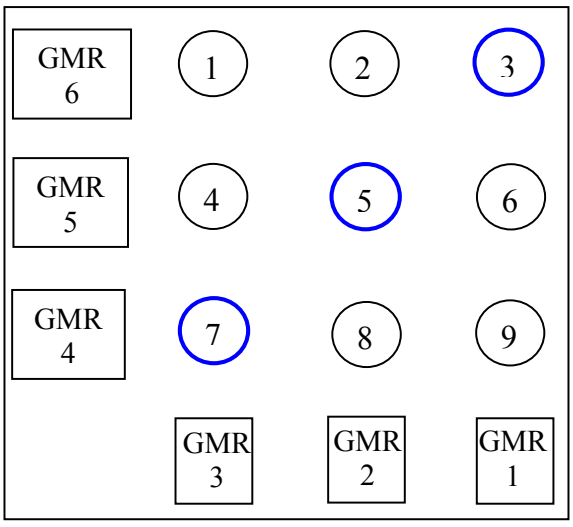

GMR & Strain Data

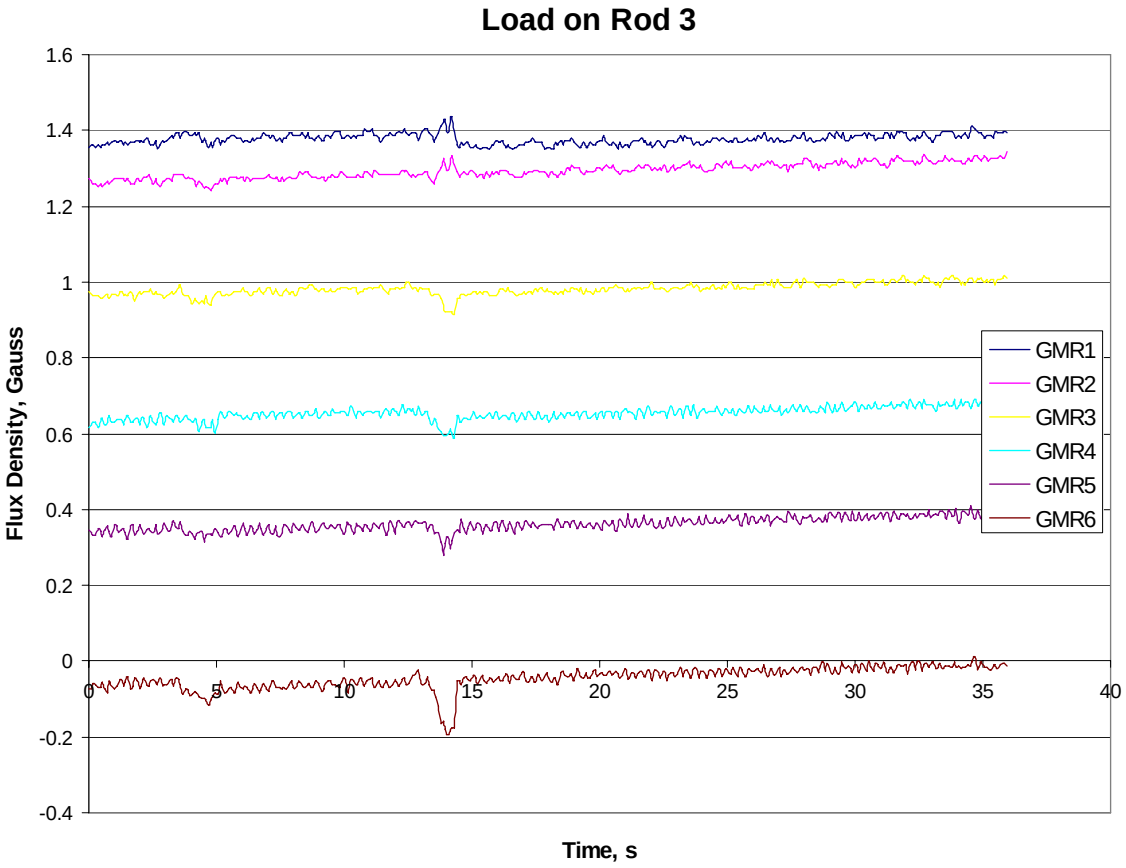

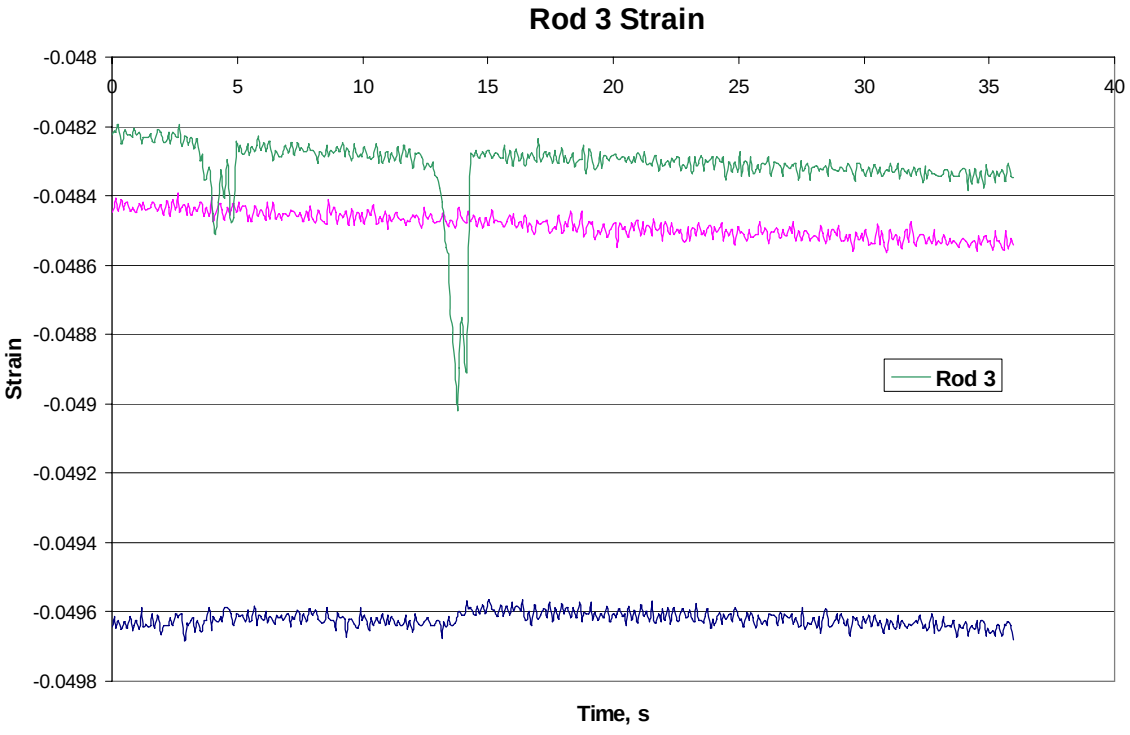

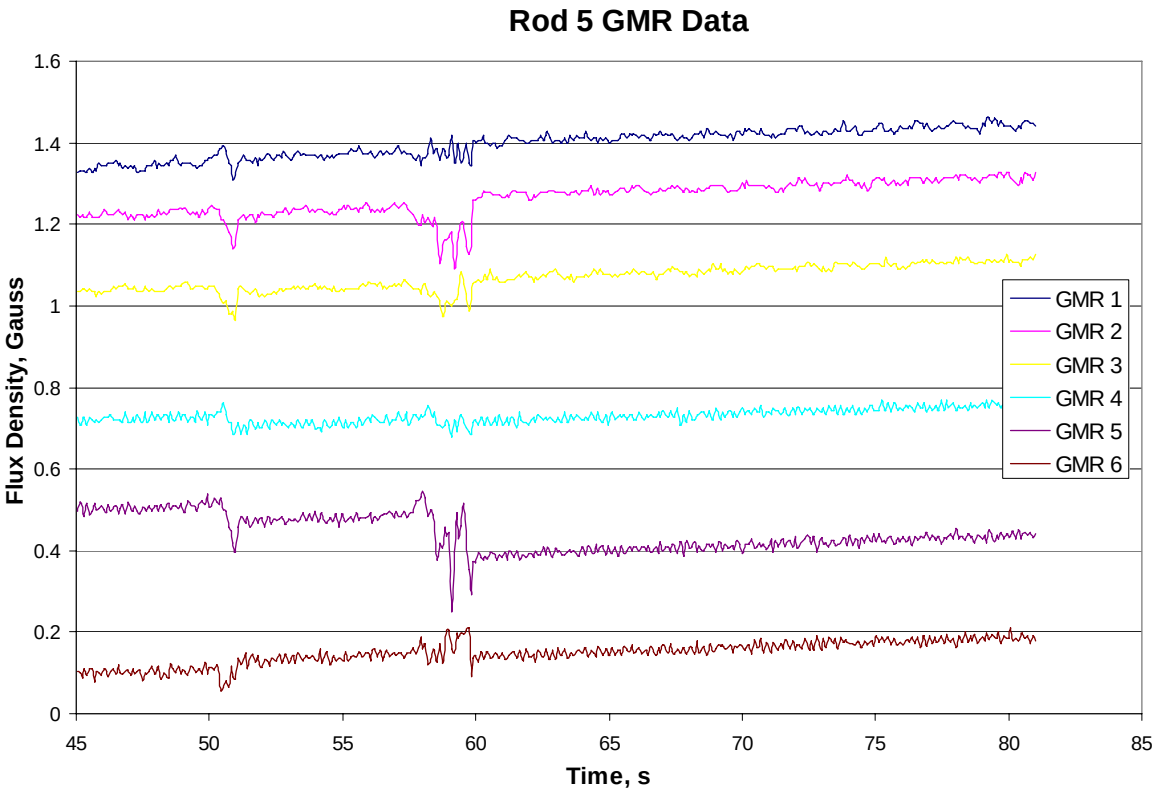
Rod 5 GMR Data
Flux Density, Gauss
1.6
1.4
1.2
1
0.8
0.6
0.4
0.2
0
45
50
55
60
65
70
75
80
85
Time, s
GMR 1
GMR 2
GMR 3
GMR 4
GMR 5
GMR 6

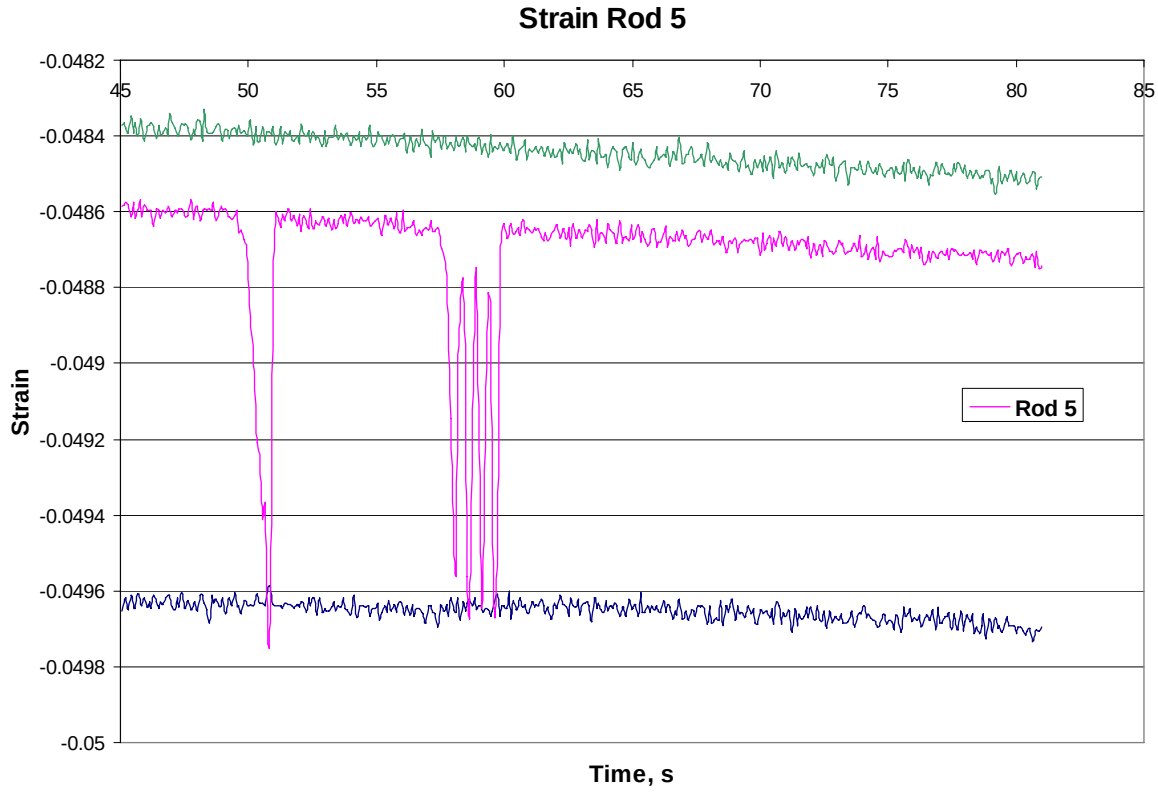
Strain Rod 5
Strain
-0.0482
-0.0484
-0.0486
-0.0488
-0.049
-0.0492
-0.0494
-0.0496
-0.0498
-0.05
45
50
55
60
65
70
75
80
85
Time, s
Rod 5

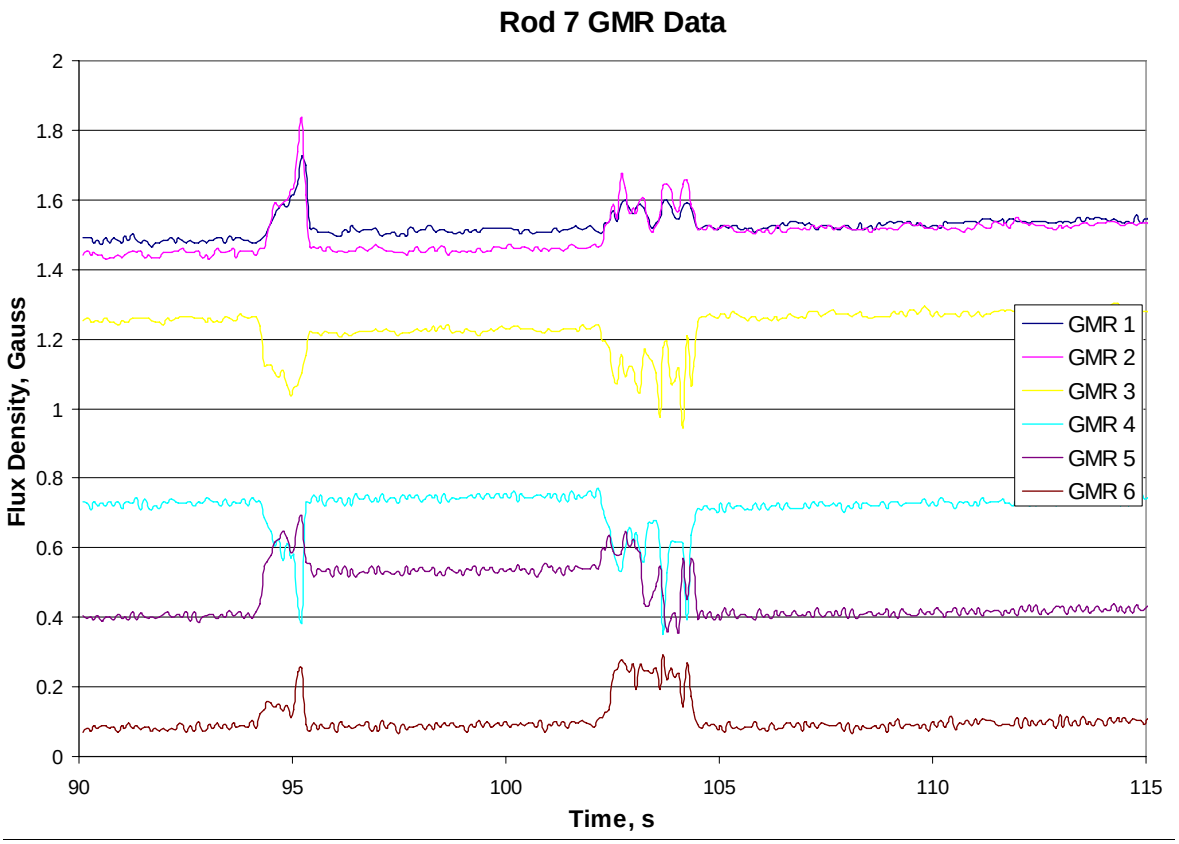
Rod 7 GMR Data
Flux Density, Gauss
Time, s
GMR 1
GMR 2
GMR 3
GMR 4
GMR 5
GMR 6
2
1.8
1.6
1.4
1.2
1
0.8
0.6
0.4
0.2
0
90
95
100
105
110
115

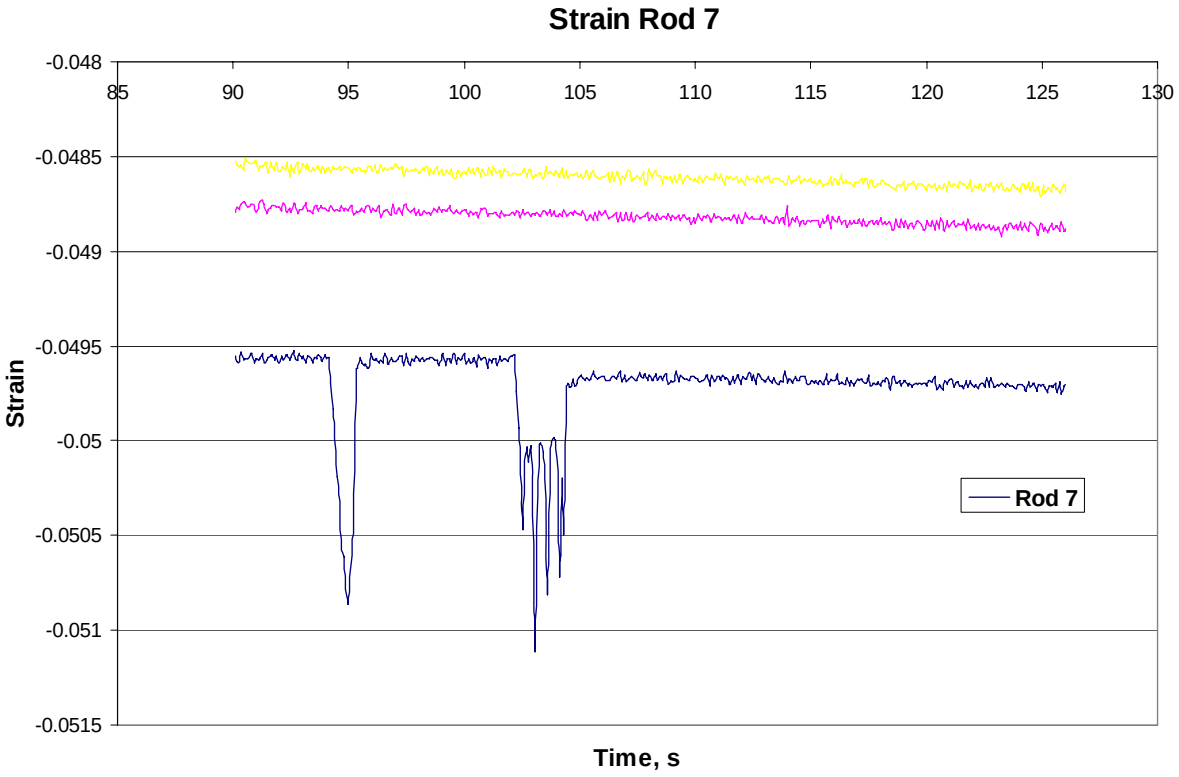
Strain Rod 7
Strain
Time, s
Rod 7
-0.048
-0.0485
-0.049
-0.0495
-0.05
-0.0505
-0.051
-0.0515
85
90
95
100
105
110
115
120
125
130

REFERENCES

Atulasimha, Jayasimha and Alison Flatau. "Quasistatic Actuation Characteristics of Varied Stoichiometry Single Crystal Iron-Gallium." Dissertation, Department of Aerospace Engineering, University of Maryland, College Park, MD, 2006.

Atulasimha, J, Flatau, AB, Kellogg, RA. "Sensing behavior of varied stoichiometry single crystal Fe-Ga." Journal of Intelligent Material Systems and Structures, Vol. 17, No. 2: 97-105, 2006.

Biagiotti, L., C. Melchiorri, and G.Vassura. "A Dexterous Robotic Gripper for Autonomous Grasping." Industrial Robot. Vol. 30 – Number 5: pp. 449-458, 2003.

Bluethmann, William, Robert Ambrose, Myron Diftler, Scott Askew, Eric Huber, Michael Goza, Fredrik Rehnmark, Chris Lovchik, and Darby Magruder. "Robonaut: A Robot Designed to Work with Humans in Space." Autonomous Robots. Mar 2003: Vol 14(2-3): 179-197.

Cobian, Ryan. "Tuning the Structural and Magnetic Properties of Cobalt and Cobalt/Copper Multilayered Nanowires" M.S. Thesis, Electrical Engineering Department, University of Minnesota, May, 2004.

Clark, A. E., Restorff, J. B., Wun-Fogle, M., Lograsso, T. A. and Schlagel, D. L., IEEE Trans. Magn., 36, 3238 (2000).

Calkins, F.T., Flatau, A.B. and Dapino, M.J. 1999. ''Overview of Magnetostrictive Sensor Technology,'' In: 40th AIAA/ASME/ASCE/AHS/ASC Structures, Structural Dynamics, and Materials Conference and Exhibit, St. Louis, MO, Apr, AIAA-99-1551, Vol. 4, pp. 2763–2772.

Fitzgerald, A.E., Charles Kingsley Jr., Stephen D. Umans. *Electric Machinery,* 6th ed., McGraw-Hill, 2003, chapter 1.

Kellogg, R.A., Ph.D. Dissertation, Iowa State University, 2002.

Lanfranco, Anthony R., Andres E. Castellanos, Jaydev P. Desai, and William C. Meyers. "Robotic Surgery: A Current Perspective." Annals of Surgery. 2004 January; vol. 239(1): 14–21.

Lee, Benjamin R., Jeffrey A. Cadeddu, Dan Stoianovici, Louis Kavoussi. "Telemedicine and Surgical Robotics: Urologic Applications." Reviews in Urology. 1999; vol. 1(2): 104-120.

Maheshwari, Vivek, and Ravi F. Saraf. "High-Resolution Thin-Film Device to Sense Texture by Touch." Science, 9 June 2006: 1501-1504.

McGary, Patrick D., Liwen Tan, Jia Zou, and Bethanie J. H. Stadler, Patrick R. Downey, and Alison B. Flatau. “Magnetic Nanowires for Acoustic Sensors.” Journal of Applied Physics, Vol. 99, 1, 2006.

Smith, Carl H. and Robert W. Schneider. “Low-Field Magnetic Sensing with GMR Sensors.” Nonvolatile Electronics, Inc. 1999. <http://www.nve.com/Downloads/lowfield.pdf>

Summers, Eric, Thomas A. Lograsso, Jonathan D. Snodgrass, and Julie Slaughter. “Magnetic and Mechanical Properties of Polycrystalline Galfenol.” Proceedings of SPIE. July 2004. Vol. 5387: 448-459.

Walker LDJ Scientific, Inc. “The Initial and Four-Quadrant BH-Curve of Soft Magnetic Materials.” <http://www.walkerscientific.com/Products/Product_Lines/Magnetic_Analysis/Hysteresisgraphs/Initial-4-Quadrant.pdf>

Zecca, M., G. Cappiello, F. Sebastiani, S. Roccella, F. Vecchi, M. C. Carrozza, P. Dario. “Experimental Analysis of the Proprioceptive and Exteroceptive Sensors of an Underactuated Prosthetic Hand.” International Journal of HWRS. v. 4., no. 4, Dec 2003.

http://robonaut.jsc.nasa.gov

http://www.public.iastate.edu/~terfenol/homepage.html